Advancing Widefield Nanodiamond Biological Sensing with CMOS Detection

PhD Thesis

Rebecca Craig

Nanobiophotonics
Department of Physics
University of Strathclyde, Glasgow

February 23, 2026

Signed:

Date: 17th October 2025

Declaration of Work

All work completed in this thesis was completed by myself. Excluding:

1. Sample preparation in Section 2.4.2, the cells were prepared and donated by Ms Mollie Brown, Dr Shannan Foylan and Dr Megan Clapperton.
2. The code used for acquiring data, which was produced by Dr Brian Patton.
3. The code used for data analysis which was primarily produced by Dr Ryan Corbyn and Dr Brian Patton, the code is detailed in [1]. The only alteration made to this code for this work was the inclusion of a widefield modality for noise weighting where the average intensity was multiplied by the number of pixels the region of interest was measured over.

Abstract

The prospect of using fluorescent nanodiamonds for biological imaging guided the work in this thesis. Fluorescent nanodiamonds have a small size (5 nm - 140 nm), which makes them an optimum choice for targeting cellular structures within an organism. Diamond is also biocompatible with no photobleaching effects, which allows for long-term imaging without toxic effects to the sample or concerns over signal loss. My PhD aimed to determine the feasibility of using a diffraction-limited, widefield microscope with CMOS camera detection for optically detected magnetic resonance spectroscopy of nitrogen-vacancy ensembles in fluorescent nanodiamonds in biological samples.

First, a widefield microscope capable of such sensing was designed, built and characterised. The optical design involved widefield epifluorescence and prism-based total internal reflection fluorescence microscopy; both of these imaging modalities were characterised for their noise properties. The total internal reflection fluorescence mode and the evanescent field propagation depth was measured for total internal reflection. Both modes were used to image focal adhesions in HeLa cells to evaluate the excitation benefits of total internal reflection fluorescence over widefield epifluorescence. After optical characterisation, the optically detected magnetic resonance schemes were applied and investigated. To fully explore the novel challenges of widefield nitrogen vacancy spectroscopy, the achievable image contrast enhancements from super-resolution radial fluctuations were compared with those from contrast-limited adaptive histogram equalisation to improve the selection of regions of interest.

After investigating the overall imaging performance, we characterised the optically detected magnetic resonance produced by each imaging modality, demonstrating the magnetic sensing capabilities for dynamic measurements with suitable resolution for quantitative outputs. Measurement can also be performed using temperature-sensing protocols, which this work attempts with limited success. We attribute the lack of success to hardware limitations in the temperature control system we employed. In particular, we identified an interaction between the temperature sensor used in our feedback control system and the microwaves required for optically detected magnetic resonance-based sensing.

To characterise noise, which can also affect measurement stability within the system, Allan Variance was used to assess fluorescence stability in each imaging modality for frame integration time, camera gain, and laser power, using fluorescent microspheres. Using these fluorescent microspheres, the fluorescent stability of nanodiamond over time can also be compared to evaluate its photostability, and the noise characterisation using Allan Variance can improve continuous-wave optically detected magnetic resonance measurements by informing imaging criteria selection. The Allan Variance shows promise as a means to improve continuous-wave optically detected magnetic resonance measurements in high-noise datasets by indicating the number of repeats required to improve the accuracy when fitting the data to a suitable model function, as demonstrated in the widefield epifluorescence modality. However, no improvement in imaging parameter selection is observed using Allan Variance in the total internal reflection fluorescence modality.

Finally, biological samples are used to validate the microscope's application for biological sensing using the nitrogen vacancy centre defect. Initially, *Caenorhabditis elegans* are used to demonstrate that *in situ* measurement is possible using our microscope system. *C. elegans* has the additional advantage that it has been used previously for nitrogen vacancy centre sensing with some success. Next, *Tetrahymena pyriformis* demonstrates the ability of live-cell nitrogen vacancy centre sensing from within an organism. Allan Variance is used to determine whether additional noise arises from the inclusion of biological material in fluorescence imaging, which could lead to less accurate spectral measurements, thereby demonstrating the novelty of Allan Variance as a tool in biological fluorescence imaging. The final biological experiment is an investigation into the feasibility of using fluorescent nanodiamond to evaluate the thermal response in photosynthesis during light and dark reaction time which was done using Pond Weed and *Spirogyra varians*, it is possible to induce a blue shift in the spectra indicating a measurable thermal event but the thermal response is not characterised due to the interaction of the microwaves with the thermistor.

Acknowledgements

To those who walked this path with me, thank you.

This work would not have been possible without all the amazing people who stood beside me. Celebrating successes and encouraging me through failures.

I want to thank Dr Brian Patton and Prof Gail McConnell. You both had a hand in getting me to this point, both being patient and kind to me throughout all the ups and downs of this experience. Thank you for your kind encouragement and frank discussions that helped shape me as a researcher. Brian, you had endless patience, you gave me opportunities I didn't think I'd get, and you have given me the ability to work through anything I don't know. Gail, you always pushed me to be better, more critical, more precise, even when I was an undergraduate fumbling through a summer project. You both taught me that this can be fun, too.

The wonderful research groups: Nanobiophotonics and Centre for Biophotonics. I'll miss our random conversations in the office, the laughter and every lunch spent taking a break from the stress of academia, which may have kept me sane. Petros, Gemma and Ryan, we survived the COVID lockdowns with shared lab time and appropriately distanced lunches before being able to share a drink when the world started to look more familiar. Bea, Shannan, Mollie, Kay, Laura, Lewis, Louise and Oz, you've always been a text away when I'm completely lost, and the organised chaos made every moment fun. Thank you, Dr Liam Rooney, for talking me through biology every time I asked (and only slightly laughing when I said or did the silly thing), for reading anything I sent, and for making me a better researcher. You did some heavy lifting there.

I need to acknowledge the friends who have been here since our undergraduate together, it brings me comfort to know there will always be a reason in our future to be in the same city at some point. Meg, you've been a fantastic friend. It was a pleasant turn of events getting to work alongside you (the head pats helped). You've taught me so much; you'll always be the cat's Aunty and the tonsil fairy. Jay, you challenge me every time we talk, you bring such joy and fun whilst putting me to shame every time. I owe you so much for all the time you spent reading this thesis - Viva la semi-colon. Emma, your hard work and dedication to science is inspiring. Thank you for the good times and the bad; they made me a better person.

I had the pleasure of meeting Dillon and Bethan at Photon 2022, a happy coincidence that we were working in buildings a few over from each other. Coffees and pints, commiseration and celebration, we were there for it all, thank you for the endless support, encouragement and community you both gave me. At SCOT2024, I met Iain. Thank you for becoming one of my best friends so quickly. You support every wild idea that comes into my mind and try to make it possible, which made writing this so much more fun. I know we'll have many more hikes, climbs and shopping trips in our future.

My family supported me through my whole life, confused by the only scientist in the family, but never stopped cheering me on. Dad, you bought me my first microscope when I was 8; you started this. You've made sure I always have the means to achieve and shown me the value of a good days graft, you always let me help with the heavy lifting and taught me I can do anything, thank you. Mum, you read every piece of work I ever submitted (not this, though, that seems a bit much), picked me up off the floor when the world was crashing down on me, and you let me focus. You made sure I could, thank you. Hannah and Abs, you both have no idea how much you challenge me every day, you have faith in me when I don't, and you remind me I need to get over myself sometimes. Thank you for being a driving force behind me.

Finally, Thea and Nyx, the cats that scream at me from across the room. Thank you for standing by the food bowls, reminding me that bills need to be paid and to just do the thing. Your obliviousness to the world around you truly is an inspiration.

Research Outputs

1. **Craig, R.***, Christopher, J.*, McHugh, R. E., Roe, A. J., Bauer, R., Patton, B. R., McConnell, G. & Rooney, L. M. "A 3D-printed optical microscope for low-cost histological imaging" 1. In: *Journal of Microscopy.* 298 3 (Jun 2025) p. 274-282 9
2. Munck, S., Cawthorne, C., EscamillaAyala, A., Kerstens, A., Gabarre, S., Wesencraft, K., Battistella, E., **Craig, R.**, Reynaud, E. G., Swoger, J. & McConnell, G. "Challenges and advances in optical 3D mesoscale imaging". In: *Journal of Microscopy.* 286 3 (Jun 2022) p. 201-219 19

Conference Presentations

1. **Craig, R.** & Patton, B. R., "Optically detected magnetic resonance of nanodiamond using widefield detection", Poster Presentation, Symbiosis: Healthcare Biosensing and Bioimaging Exchange (2023). Glasgow, United Kingdom.
2. **Craig, R.** & Patton, B. R., "A Multimodal Microscope for Improved Contrast Imaging and Optically Detected Magnetic Resonance of NV- Centres in Nanodiamond", Oral Presentation, Scottish Microscopy Society Annual Symposium (2023). Dundee, United Kingdom.
3. **Craig, R.** & Patton, B. R., "The use of diffraction-limited microscopy to complement super-resolution microscopy", Oral Presentation, Super-resolution Workshop 2023 (2023). Leeds, United Kingdom.
4. **Craig, R.**, Patton, B. R. & Jones, A. R., "From OLEDs to animal magnetoreception: quantum nanodiamond for the detection of short-lived paramagnetic spin-states generated by light", Oral Presentation (*Invited Speaker*), National Institute of Standards and Technology NIST (2023). Gaithersburg, United States of America.
5. **Craig, R.** & Patton, B. R., "The use of diffraction-limited microscopy to complement super-resolution microscopy", Poster Presentation, Photon 2022 (2022). Nottingham, United Kingdom.
6. **Craig, R.**, Patton, B. R. & Corbyn, R., "Quantum on a budget: developing a 3d-printed microscope for optically detected magnetic resonance of nanodiamond", Poster Presentation, Microscience Microscopy Congress - MMC (2021). Online.

Acronym List

In order of appearance.

NV-	Nitrogen Vacancy
CLAHE	Contrast Limited Adaptive Histogram Equalization
SRRF	Super Resolution Radial Fluctuations
(CW)ODMR	(Continuous Wave) Optically Detected Magnetic Resonance
FND	Fluorescent Nanodiamond

Contents

Nothing in life is to be feared,

it is only to be understood.

MARIE CURIE

Chapter 1

Introduction

Biological measurement is fundamental to unlocking the mechanisms that sustain life, revealing how organisms function and respond to their environments. [2] The imaging systems designed are increasingly specialised in undertaking these measurements, and the drive to get measurements at the nanoscale to pinpoint biochemical events in live samples is increasing. [3] These measurements are often complex, invasive, and expensive, and all of these are restrictive to improving our understanding. Examples of processes being investigated across a range of organisms and cell types include Ca2+ release, and the biochemical reactions in microbial samples for the determination of hazardous pesticides. [4], [5] Nanodiamonds offer the ability to measure a range of these processes with a single fluorophore, can be imaged with various microscopes and are biocompatible with biological samples. [6]

Nanodiamonds, diamonds measuring less than 1 micron, are of interest for their versatility; they can be used for fluorescent labelling and various sensing applications. [7] The optically active component utilised within this work is the Nitrogen Vacancy defect (NV-) within the nanodiamond crystalline structure, the schemes for NV- defect sensing based on the optical properties often employed for spectroscopic sensing of temperature, magnetic field or presence of key biomolecules. [8] Spectroscopic sensing schemes are complex, invasive and expensive due to requirements for highly technical instrumentation, high optical powers or the choice of components for a system. [9] Here, we set out to investigate the viability of an imaging system for live biological imaging and sensing using nanodiamonds as a cellular sensor for spectroscopy. To do so, we employ previously validated techniques to validate and determine the efficacy of an imaging system designed to be widely accessible. Key criteria centred on maintaining the viability of biological samples whilst determining the essentials for the aforementioned schemes to reduce overall cost, as well as demonstrating the capabilities of such a system for biological investigation in live samples.

NV- sensing measurements are commonly performed using photodetectors for fluorescence detection because they are more sensitive to fluorescent fluctuations than widefield sensing techniques. However, widefield techniques offer advantages over single-photon detectors for biological measurements, as fluorescence provides spatial information about biological structure, limited only by exposure time rather than the area of detection, thereby providing additional information on the measured biochemical event without additional imaging time. One type of widefield detector that offers comparable sensitivity to the photodetectors mentioned above is the EMCCD camera, which is discussed later in this chapter. However, an EMCCD camera is costly ($>$ 10k GBP per camera unit), limiting the accessibility of widefield measurements for many labs.

NV- based sensing is a photometric technique that requires accurate measurement of both the total photon flux from the defects and changes in the emission in response to environmental effects. Therefore, efficient photon collection is imperative for the quality of the spectra acquired, raising the question of whether a CMOS camera could be used for such measurements, since it is not as low-noise as an EMCCD but is a less expensive alternative. If a CMOS camera can have sufficiently low noise for NV-sensing, then the critical components required to acquire sufficient signal to produce NV- spectra suitable for practical measurement, such as thermometry, would be key understanding required to undertake measurements reliably. Reducing the complexity of systems required for NV- sensing to the minimum necessary would increase uptake of the technique for biological measurement, since the need for highly experienced microscopists decreases as the cost of the measurement systems decreases.

Determination of the base requirements for success involved a complete characterisation of the microscope systems used. In this work, it is investigated whether widefield fluorescence could be used for thermometry, and the results are compared with previous research using EMCCD detection. The system is designed to allow excitation of the sample in both epifluorescence and total internal reflection modalities, although not always simultaneously, depending on sample preparation. We investigate whether classical methods of characterisation or image noise reduction affect the application of NV- sensing. Further, novel techniques for testing fluorescence stability using Allan deviation demonstrate the importance of an adequate sample size and normalisation in NV- sensing to reduce the noise associated with prolonged measurements. [10]

Although widefield measurement produces images with many NV- centers present in the field of view, not all NV- centres will be suitable for measurement. Therefore, characterisation of region-of-interest selection and the best approach for extracting positional information for optimal region-of-interest selection are evaluated. Image enhancement tools - Contrast Limited Adaptive Histogram Equalisation (CLAHE) and Super-Resolution Radial Fluctuations (SRRF) - are compared against one another to determine the best method to extract spatial information on optically detected magnetic resonance (ODMR) responsive emitters and the resulting quality of ODMR spectra produced from the selection determined by its spectral contrast and inhomogeneous broadening. [11] The quality of the spectra produced from widefield epifluorescence microscopy and total internal reflection fluorescence microscopy is evaluated alongside the effects of dual excitation from either two wavelength excitation in widefield epifluorescence microscopy or single wavelength excitation in both epifluorescence and total internal reflection fluorescence on the resulting spectra.

Initial tests of sensing with external magnetic fields are conducted by introducing a magnetic field and evaluating the resulting Zeeman splitting to quantify the effects of neodymium magnets and magnetic nanoparticles in proximity to the NV- centre on the spectra. By quantifying each of these effects, it could be determined whether there is a local detection of the applied magnetic field near the NV- centre, or, in the case of the magnetic nanoparticles, a distortion or amplification of the detected field strength. The introduction of magnetic nanoparticles into biological samples is part of an established protocol for biological measurement undertaken in this work. Thermometry is of great interest due to its ability to measure biochemically induced temperature differentials; this work details attempts at thermometry characterisation, which are limited by technical problems arising from microwave interference with thermisters and thermocouples.

Finally, the NV- sensing application to biological specimens is explored. *Caenorhabditis elegans* is a model organism explored for biological measurements using NV- centres, using *C. elegans* as a confirmatory experiment that the system designed is capable of measurement, because of its popularity, it has been used in previous NV- sensing work so that it could stand as a benchmark for the performance of the hardware. Expanding into other biological models, the work presented shows the application of Allan Variance for photostability in live cell imaging compared to NV- centre exclusive measurement in *Tetrahymena pyriformis* (a unicellular eukaryote found in ponds) and also showed a method for measuring the thermal change during photosynthesis of Chlorophyll II in pond weed and *Spirogyra varians* (strand-like algae).

1.1 Overview of Thesis Structure

The introduction provides an overview of the key theoretical and experimental techniques employed in this research. Due to the multiple disciplines employed in this work, the introduction will be split into Optics and Microscopy to cover the theory used in microscopy techniques for system development, and Nitrogen Vacancy Defect to introduce and discuss the diamond lattice defect used for ODMR and the continual development of ODMR-based techniques for thermometry. Theory concludes with Allan Variance, covering the relevant theory for stability measurements and noise characterisation. There is also a section describing some key stylistic choices throughout this work.

The subsequent chapters all begin with a brief literature review that discusses the field's current state and explores the motivations for the developmental and statistical approaches undertaken. Finally, the thesis concludes with an overview of how the preceding chapters are combined to achieve the final goal of biological measurement with NV- centres using widefield imaging for enhanced spatial information during dynamic processes, compared to systems that employ single-pixel detection.

1.2 Optics and Microscopy Theory

The research presented in this thesis is based on microscopic imaging; for the systems used, the ray-optics formalism will allow sufficient modelling and description of the imaging paths, enabling the design of the microscope to meet our project requirements and design goals. This section will explore image formation, fluorescence, numerical aperture, magnification and resolution limits as described by ray optics. A mechanical and theoretical overview of relevant imaging systems, equipment, and processing techniques is given to describe both the advantages and any limitations of the techniques and methods discussed. This discussion provides context for decisions made throughout this thesis.

Most of this discussion is from [12], unless otherwise noted.

1.2.1 Ray Optics and Image Formation

The introduction of lenses into the path of light propagation, as shown in Fig. 1.1, leads to the formation of real and virtual images. Using concave and convex lenses dictates which type of image - real or virtual - will be formed, depending on the lens's position on the optical axis and its focal length. Image formation is critical to microscopy, as it determines the final image, which is usually a magnified view of the structure of interest. The configuration of lenses required in an optical path will vary depending on the final image desired; a ray diagram illustrates the beam path, which usually indicates the real and virtual image formations.

1.2.2 Numerical Aperture, Image Contrast and Resolution

Numerical aperture (**NA**) is the relationship between the refractive index (**n**) and the half angular aperture (α), which describes the cone in which photons will be collected for imaging, described by Eq. 1.1.

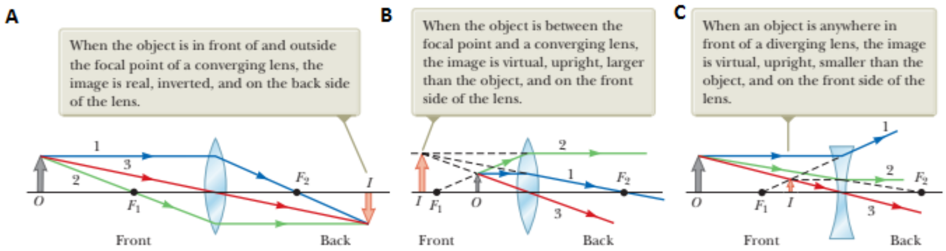

Figure 1.1: Ray tracings for lenses where (a) the image is real and inverted after light interacts with a convex lens, (b) the image is virtual and upright after light interacts with a convex lens due to the object's positioning closer to the lens than the focal length and (c) the image is virtual and upright after light interacts with a concave lens producing a smaller image relative to the object of interest. Figure extracted from [12]

$$NA = n \sin \alpha \tag{1.1}$$

Image contrast is the quantifiable difference in intensity between an object of interest and its background, or between two objects of interest. It is determined by the resulting intensity difference in light from different areas, after noise is accounted for. In brightfield (see Section 1.2.8) microscopy, contrast arises from the illumination passing through an object, which scatters the light being received at the detector, causing a high background and low structure contrast. Conversely, fluorescence microscopy (see Section 1.2.9) has a low background and high structural contrast, with a label that is highly specific to the structure.

Resolution, in part, depends on contrast resolution: it is the smallest distance between two objects at which they are still distinguishable. There are many different approximations of the resolution limit, such as Rayleigh, Sparrow and Abbes, which produce comparable values; for consistency, we will use the Abbe resolution criterion/limit as the definition of resolution in this work. The resolution definitions in this section describe the resolution limit in optical diffraction-limited microscopy. The smallest resolvable separation (**d**) in fluorescence microscopy is dependent on the numerical aperture (**NA**) of the system and the wavelength (λ). There is also a dependence on the frame of reference, whether lateral (XY, plane perpendicular to the optical axis) or axial (Z, parallel to the propagation of light), such that:

$$d_{xy} = \frac{\lambda}{2NA} \tag{1.2}$$

$$d_z = \frac{2\lambda}{NA^2} \tag{1.3}$$

For example, in a system with a numerical aperture of 1.25 and emission wavelength of 532 nm, this corresponds to a lateral resolution of 213 nm and an axial resolution of 680 nm using Eq 1.2 and Eq 1.3, respectively. Depth of field is the volume (or distance along the z-axis) where the structures are "in focus", the point at which the contrast between structures is sharpest. The depth of field (d_{tot}) is dependent on the wavelength, numerical aperture, the refractive index (n), the lateral magnification (M) and the resolution of the detector in the imaging plane (e) as described in Eq. 1.4.

$$d_{tot} = \frac{\lambda.n}{NA^2} + \frac{n.e}{M.NA} \tag{1.4}$$

Another way resolution is represented is the Airy Disk (XY) function, a mathematical approximation of the system response to an infinitely small emitter. The Airy disk shows a point emitter with a central disk containing 84% of the light intensity, surrounded by dim concentric rings, as shown in Fig. 1.2. Because the nanodiamonds are smaller than the diffraction limit, Airy rings are present in images throughout this work, as they are infinitely small emitters compared to the limit of detection.

1.2.3 Total Internal Reflection

Refractive index (n) is a critical parameter in the following discussion. It is the ratio of the speed of light in air (c) vs the speed of light in a medium (v), which is calculated using the wavelength (λ) and the frequency (f) in Eq. 1.5 and 1.6. [12]

$$n = \frac{c}{v} \tag{1.5}$$

$$v = f\lambda \tag{1.6}$$

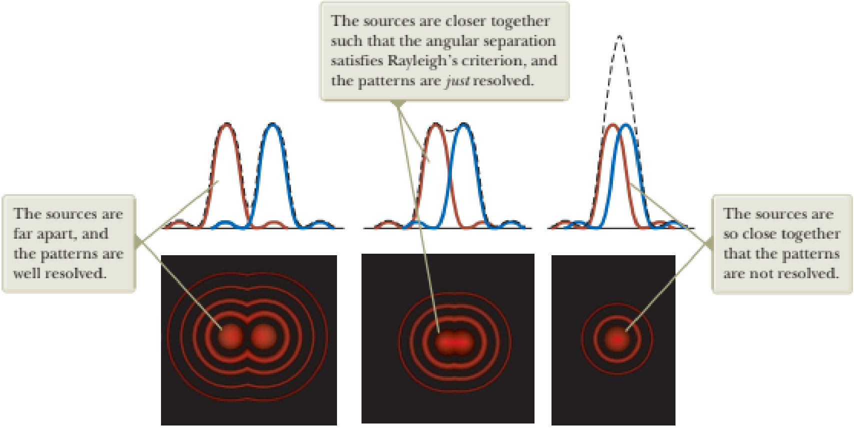

Figure 1.2: Figure showing the appearance of Airy rings on point emitters and the resulting intensity plots (upper row) for categorising the resolvable distance between them. Figure from [12]

Snell's Law is the process by which a refractive index interface changes the velocity and direction of light; the change is angular, which will be determined by Snell's Law where the angle of entrance (Θ_1) through a medium of refractive index (n_1) interacts with a medium of refractive index (n_2) and propagates with an angle of (Θ_2) through the relationship shown in Eq. 1.7 and shown in Fig. 1.3. A change in angle of propagation occurs because of the change in velocity of the wave as it passes through the medium.

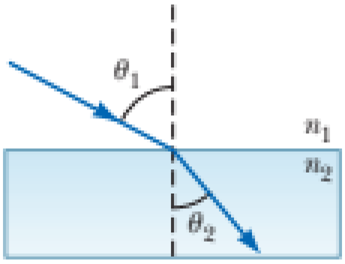

Figure 1.3: Light penetrates with angle Θ_1 from refractive index n_1, at the interface of the two media, the angle of travel Θ_2 changes in media of refractive index n_2. Figure extracted from [12].

$$n_1 \sin \Theta_1 = n_2 \sin \Theta_2 \tag{1.7}$$

The critical angle (Θ_c) is the angle at which light enters the second medium and exits 90^o to the normal (perpendicular to the interface). A ray is reflected within the system (Eq. 1.8). In the case of Fig.1.4, the second refractive index (air) is lower than the first (glass). Angles of incidence greater than the critical angle result in total internal reflection.

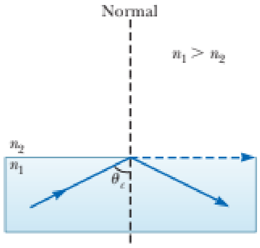

Figure 1.4: Total Internal Reflectance occurs when the beam incident angle on the refractive index interface is smaller than the critical angle, and the beam is reflected within the media. At the critical angle, the beam travels along the surface of the medium. Figure extracted from [12].

$$\sin\Theta_c = \frac{n_2}{n_1} \tag{1.8}$$

Total internal reflection is the process by which a beam is reflected within the medium at the same angle it entered the medium at the normal. Optical fibres work on this principle by ensuring that light is always totally internally reflected through the length of the cable.

1.2.4 Fluorescence

Fluorescence is the phenomenon in which an atom absorbs a photon, usually emitting a photon of a specific wavelength stochastically after some time. Fluorescence lifetime is the average time a molecule spends in an excited electronic state before returning to the ground state by emitting a photon. Fluorescent labelling is particularly useful in microscopy since fluorophores, molecules or particles that exhibit fluorescence, can be used to label structures of interest, allowing the user to collect information only from that structure. The ability to generate signals primarily at locations of interest, rather than elsewhere in the sample, is called the contrast mechanism and is critical to fluorescent microscopy techniques. [13] Image contrast in microscopy is determined by the dynamic range of the detection method used, where the highest value possible is saturation and the lowest is background in fluorescence microscopy.

For fluorescence microscopy, excitation filters can be placed before the detector to eliminate excitation wavelengths, allowing only fluorescence from the sample to be detected and improving contrast. [14] The use of filters also allows multi-labelling of samples with different structures labelled with different fluorophores, which emit at different wavelengths. The emission of one fluorophore can be rejected, and the emission of another can be detected if the fluorophore emission is sufficiently separated in wavelength such that a suitable filter placed in front of the detector will pass light from only one of the fluorophores and reject the light from the others.

The Jablonski energy diagram describes the key states associated with a given molecule's electronic structure, which is useful for describing fluorescence in microscopy. As a primary principle, singlet spin states are denoted by $\mathbf{S}$ and triplet spin states are denoted by $\mathbf{T}$; a molecule can have many singlet states of varying energy separated by the energy band gap, and singlet states have a spin angular momentum of 0. Conversely, triplet states have a spin angular momentum of 1. Phosphorescence is a similar process of decay to fluorescence; however, it has a longer decay time. The increase in decay time is due to a change in spin, thus, a lower probability of an additional spin flip in the subsequent emission.

Fig. 1.5 shows the energy levels associated with a molecule and the various decay and excitation paths, with the order of magnitude of the lifetimes included. Excitation occurs when a photon with enough energy (i.e. the energy of the band gap) excites from the ground state ($\mathbf{S_0}$) to the excited state ($\mathbf{S_n}$) as shown with the blue straight arrows as absorption. Further excitation can occur from excited states to higher excited states, such as $\mathbf{S_3}$ to $\mathbf{S_4}$, but is not discussed in this work. This is followed by vibrational relaxation to the lowest energy state of the excited energy level, depending on the lifetimes of the vibrational relaxation processes, which can drive a preference for phonon relaxation.

Vibrational relaxation (wavey yellow lines) occurs when the molecule relaxes rapidly to the lowest vibrational state of $\mathbf{S_n}$ (any state) and does so non-radiatively, releasing energy as heat. In fluorescence emission (green lines), the molecule typically relaxes

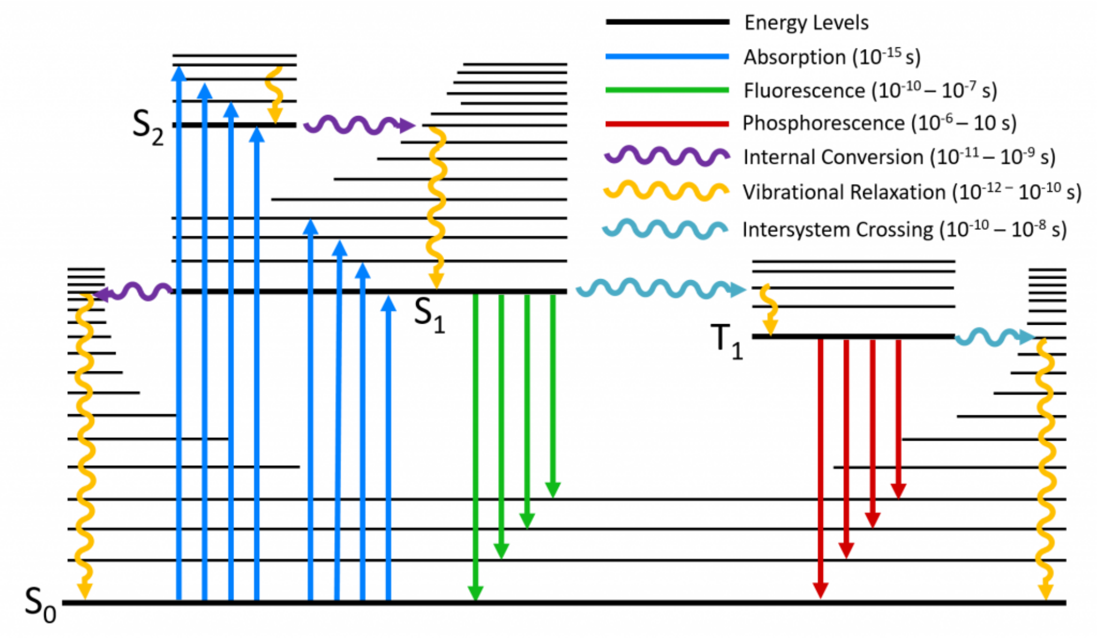

Figure 1.5: Diagram of the Jablonski Energy levels present within a molecule. Figure acquired from [15]

from the lowest vibrational state of an excited state to the ground state, emitting a photon with less energy than the absorbed one (a longer wavelength); this is Stokes' shift.

Relaxation from the triplet state to the singlet ground state is called phosphorescence. An alternative relaxation mechanism is via another intersystem crossing event, in which a photon of much lower energy than in direct relaxation from triplet to ground state is emitted. Intersystem crossing events occur in four cases: spin-orbit coupling, where electronic and spin states are mixed; the energy gap between the excited singlet and triplet states is comparable; a vibration wavefunction overlap (Frank-Condon Principle) between the excited singlet and triplet state; and molecular structure where molecules with rigid, planar structures, conjugation or hetereoatoms are more likely to undergo this process.

1.2.5 Laser Illumination Inhomogeneity

Common benefits of lasers over other light sources are their directionality, brightness, and monochromaticity. However, this is not always the case, and especially in less expensive lasers, there are usually high levels of modal and polarisation mode dispersion, low power outputs, and a higher excitation range versus their nominal stated wavelength. [16]

In widefield imaging, the dominant inhomogeneity in laser illumination is often assumed to be speckle. Speckle is identifiable by the fluctuation in fluorescent intensity (when not anticipated) between frames (temporal) or across the field of view (spatial), neither of which is present when the illumination source is homogeneous. Often, this is exacerbated by reflections within the laser or back-reflections into the laser, creating mode instability. However, speckle depends on the source's coherence.

Studies have proposed different ways to mitigate the apparent effects of laser-field inhomogeneity, ranging from post-imaging software to mechanical vibration of fibre bundles or fast-scanning micromirrors. [17], [18], [19]

1.2.6 Detectors

Complementary Metal-Oxide Semiconductors Detectors

CMOS detectors are widely used cameras because of their low power consumption and small size. The sensor comprises pixels, and each pixel accumulates charge during image acquisition as photons excite electrons within the semiconductor. The readout electronics convert the charge to a voltage, which may need amplification through a gain stage. The output voltage is typically discretised to enable digital processing of each pixel. CMOS offers greater parallelisation in pixel readout than CCD, resulting in faster readout time.

The timing scheme that defines the exposure and readout of both individual pixels and larger groups (e.g., rows or entire sensor sectors) varies across sensors and affects image quality. A global shutter function reads all pixel values simultaneously. Alternatively, a rolling shutter typically reads pixel values line by line and transfers the data;

the entire image is read out from the first line to the last concurrently. Rolling shutter, however, introduces a delay in imaging, which could lead to distortion if the subject moves, since acquisition may be completed only partially on the subject, with the rest occurring at the new position, although read noise is lower than with a global shutter.

There are many criteria when evaluating a camera, making it applicable to all imaging parameters. Megapixels indicate how many pixels are on the sensor; the pixel size determines the camera's resolution, allowing Nyquist sampling of smaller structures within the sensor's imaging area. For extremely sensitive measurements, read noise and full well capacity become essential, with the noise indicating the predicted fluctuation in sensitivity from reading the sensor and the full well capacity indicating the total potential dynamic range of that sensor, further characterised by the quantum efficiency detailing the effectiveness of reading those photons as an electrical signal.

CMOS detection is common in microscopy, as it is often used for widefield imaging due to the simplicity of sensor readout and the high dynamic range of these sensors, developed for imaging. Outside of widespread use in modern photographic cameras, CMOS detectors have been used scientifically for electron microscopy, fluorescence lifetime microscopy, and single-molecule localisation microscopy, so they are well characterised for scientific use.

Electron Multiplying Charged Couple Devices

EMCCDs are commonly used in widefield NV- sensing experiments because they can read photons in low-light scenarios. EMCCDs operate similarly to Charge Coupled Devices; biased electrodes collect the photon charge as a positively applied voltage, and the electrons are stored in the n-type substrate before being passed to the p-type substrate and detected. EMCCDs amplify the signal collected from the electrons before passing it to the readout substrate via channels. One row of pixels is read out at a time, and the dynamic values are calculated as a share of electrons across the full sensor.

EMCCDs are preferred for widefield imaging because of their low readout noise and higher sensitivity to low light than most detectors; their quantum efficiency is much better than that of a photomultiplier tube (PMT) (approximately 99% compared to

15%), and their readout noise is much lower than that of a CMOS camera. However, the EMCCD is a very expensive detector - around 35k GBP - making it inaccessible for many users despite its better performance compared to CMOS cameras and its ease of use compared to PMTs.

CMOS Noise

T Thorlabs 2.3MP CMOS cameras detect fluorescence using a grey scale of 0 bits to 4094 bits. There are four sources of noise in a camera: dark shot noise, read noise, photon shot noise and fixed pattern noise. [20], [21]

Dark shot noise is a thermal phenomenon that occurs when valence electrons are thermally excited into the conduction band, making the silicon register a photon when none are present. Most scientific cameras now come with some form of cooling in place to mitigate the effects of this, although, to measure the effects of this on a camera, a dark image can be collected, counts collected (I_D), and Poisson statistics applied where dark shot noise (σ_D) is proportional to the temperature (T) as in Eq. 1.9.

$$\sigma_D = \sqrt{I_D * T} \tag{1.9}$$

Read noise (σ_R)is similar to dark shot noise, except it is related to the electrical current in the components, as the pixels detect a photon instead of the intrinsic thermal properties responsible for dark shot noise. CMOS cameras have an individual read noise per pixel because each pixel has its own amplifier circuit, which is a constant source of noise that does not change frame-to-frame.

Photon shot noise is directly due to quantum effects in photon collection. The collected signal can vary from frame to frame because photons are discrete and are counted only in integer values. Photon shot noise (σ_S) also follows Poisson distribution statistics, meaning it can be measured and predicted to bring detection to the "shot noise limit" which is proportional to the quantum efficiency (QE) of the camera, the photon flux (N) in photons/second and the frame integration time (t) in Eq. 1.10.

$$\sigma_P = \sqrt{(QE)N * t} \tag{1.10}$$

These values are summed as in Eq. 1.11 to find the total effective noise.

$$\sigma_{eff} = \sqrt{\sigma_D^2 + \sigma_R^2 + \sigma_S^2} \tag{1.11}$$

The signal-to-noise ratio (SNR) is then calculated by dividing the measured signal (S) by the effective noise.

$$SNR = S/\sigma_{eff} \tag{1.12}$$

Finally, fixed pattern noise is an intrinsic quality of the camera; its effects are greatly exaggerated when a high gain or a long frame integration time is used in imaging. The term comes from the linear pattern formed where stripes of lower and higher intensities appear in the field of view. Fixed pattern noise is a result of the manufacturing process, where circuitry inconsistencies lead to consistently offset intensity values. There are many ways to limit the fixed pattern noise; one approach is to use camera denoising and mask transformations on the final image, using a "dark" image at the same frame integration time and gain, or the fluorescence images.

1.2.7 General Microscopy Principles

Microscopy can be described by defining "planes" where key events (e.g., imaging) occur along the optical path; one example is the Fourier planes. Fourier planes describe the spatial frequency at a given point in an optical system; analysing these planes allows understanding of how the optical system resolves and reconstructs the object. The higher the spatial frequency after a Fourier transform, the higher the image resolution. The Fourier plane is defined at the back focal plane of the objective lens, the spatial frequency here is often characterised by low spatial frequencies at the centre corresponding to coarse features (i.e. fluorescence from a cell) and high spatial frequencies further from the centre corresponding to high resolution (i.e. fine details, such as a high frequency grating). The image plane is after the tube lens; this is the real-space image typically captured by the sensor, where the tube lens has focused light from the objective's back aperture.

For this work, the term lateral (x,y) will refer to any movement perpendicular to the axis of propagation of light, and the axial (z) refers to any movement done parallel to the axis of propagation of the light.

1.2.8 Brightfield Microscopy

In brightfield transmission microscopy, illumination uniformity across the imaged sample volume is detected by the objective, and transmitted light is collected and focused onto a sensor. The contrast mechanism for brightfield transmission microscopy relies on the sample interacting with the transmitted light. One form of interaction is absorption or changes in reflectivity, modulating the overall intensity. Another mechanism occurs in transparent samples with inhomogeneous refractive index, where the sample locally refocuses or defocuses light, making regions appear darker or brighter than the surroundings. If the sample is naturally coloured, this can also be detected using a colour camera. Live cell imaging is straightforward in this configuration, as the requirements to limit laser excitation, etc., are reduced, since a low excitation density is sufficient for imaging. [22]

The technique does not rely on fluorescence, so resolution is limited to the excitation wavelength; transparent samples often lack sufficient contrast because light is not absorbed, and highly pigmented samples often lack well-defined outer edges due to out-of-focus light absorption. Staining, such as with methylene blue, can provide contrast as structures will now absorb light where they previously did not, whilst still benefiting from the simple optical technique and the ability to easily image live cells. [23]

1.2.9 Widefield Epifluorescence Microscopy

Epifluorescence microscopy is a technique in which excitation and emission are performed through the same objective lens; "epi" means "same" in Greek. An epifluorescent microscope offers low signal loss and greater penetration depth than other techniques, such as total internal reflection fluorescence. However, this penetration depth is limited by a sample's opacity, so samples are typically optically cleared or intentionally chosen for their diaphanous structure. Moreover, epifluorescent microscopy is usually subject to high background noise due to the non-specific illumination.

For this configuration, after selecting the excitation and detection sources, the most significant consideration is the objective lens; the chosen lens will serve as the basis for most focal-length and optical positioning calculations. The most efficient excitation for epifluorescence will have the excitation focus as a tight spot at the back focal plane of the objective, as this produces collimated light from the front element, minimising optical power loss whilst exciting the entire visible sample space.

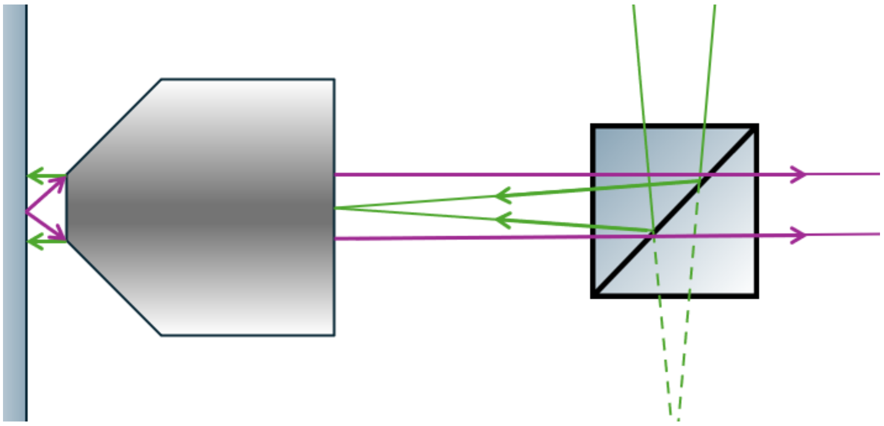

Figure 1.6: Green lines are the excitation source where the focusing beam enters a dichroic mirror and is redirected to the objective, where the beam is focused at the back aperture, resulting in collimated light entering the sample. Magenta shows the angle at which photons are collected from the emission (determined by the numerical aperture) and propagate out of the back aperture of the objective, through the dichroic mirror, separating the excitation and emission.

The excitation beam is focused on the appropriate size, calculated by multiplying the focal length and the NA of the objective to give the radius of the beam profile, at the back aperture of the objective dependent on the size of the back focal plane. An excitation filter may be used to reduce background noise from the excitation source, especially in situations where samples are sensitive to other wavelengths. Additional wavelengths may arise when a laser has a broad excitation bandwidth. In emission collection, a filter is typically used to remove the background and leave the sample emission spectra before passing the light into a tube lens to focus the image onto the detector. This technique is diffraction-limited, so the lateral resolution is calculated to

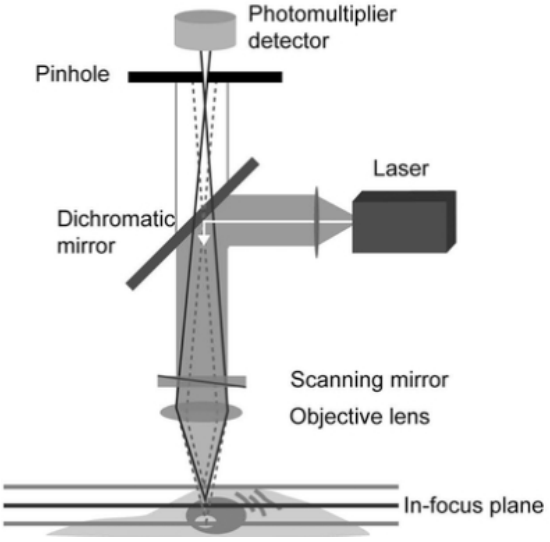

Figure 1.7: Ray diagram of confocal microscope. Figure taken from [24].

be 248 nm for a 100x objective lens with an NA of 1.25 and a wavelength of 532 nm.

1.2.10 Confocal Microscopy

Confocal Microscopy is a technique that improves lateral (x,y) and axial (z-axis) spatial resolution compared to conventional widefield fluorescence microscopy by using a tightly focused illumination spot to excite the sample and a pinhole at the detector. The size of the excitation cone is directly related to the numerical aperture of the objective being used, as the excitation fills the back aperture of the objective to use the full NA of the lens, where light is then produced through at the imaging plane, focusing onto the sample. Emission is detected via an objective, and then passes through a pinhole that rejects out-of-focus fluorescence from the sample. The rejection of this out-of-focus fluorescence increases image contrast compared to total volume excitation. The excitation spot is either scanned over the entire field of view or the sample is scanned through the excitation volume to generate an image. A ray diagram is presented in Fig. 1.7 showing the pinhole rejection of this out-of-focus light.

1.2.11 Total Internal Reflectance Fluorescence Microscopy

Total internal reflection fluorescence is based on total internal reflection, where light incident on a medium of higher refractive index enters at or above the critical angle in a medium of lower refractive index. When this occurs, the field produced has an associated evanescent field of a few hundred nanometers; this is what gives total internal reflection fluorescence lower background noise and better optical sectioning at the surface than other systems, since only a very small axial volume is excited. However, the small evanescent field produced means it has a minimal penetration depth (d), which is calculated using Eq. 1.13, where λ_0 is the initial wavelength, n_1 and n_2 are the refractive indices of medium one and two, respectively. Using this penetration depth, the intensity at a distance z from the prism interface, I_z, can be calculated from the initial intensity I_0 through the exponential relationship provided in Eq. 1.14

$$d = \frac{\lambda_0}{4\pi\sqrt{n_1^2 \sin^2\theta - n_2^2}} \tag{1.13}$$

$$I_z = I_0 \exp -\frac{z}{d} \tag{1.14}$$

There are two typical schemes for total internal reflection fluorescence microscopy: through-objective and prism-based. The former uses a specialised objective with high NA whose maximum half-angle exceeds the critical angle in the imaging medium. However, the beam is usually offset to the side of the back aperture (offset from the central axis) and is reflected into the collected wavelengths as the "back-reflected beam", despite being outside the cone of collection dictated by the numerical aperture of the objective, which requires filtering to separate from the fluorescence from the sample.

Prism-based total internal reflection fluorescence microscopy uses a prism, usually BK15 glass, in which the excitation is incident at the critical angle; prisms can be purchased and cut to the critical angle for easier alignment. The objective does not collect the evanescent field; only fluorescence is collected. Prism-based total internal reflection fluorescence microscopy has lower background noise than the through-objective method because it does not require filtering the excitation wavelength from the col-

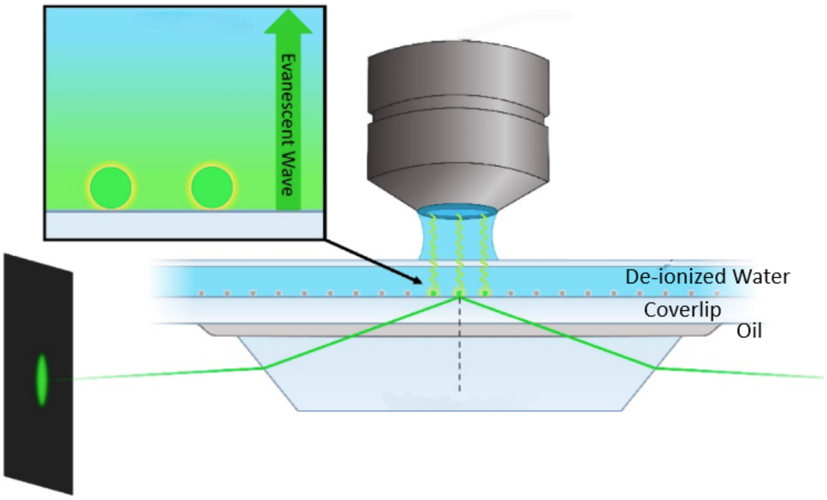

Figure 1.8: Diagram showing the ray propagation in a prism for total internal reflection fluorescence microscopy, light enters and is refracted due to Snell's Law; when it reaches the top surface, it propagates greater than the critical angle, reflecting into the prism and producing an evanescent field from the top surface into the sample. A change in line style indicates the beam path. Figure adapted from [25].

lected signal. Alongside this and the reduced effects of autofluorescence, scattering and stray illumination because of the smaller volume of excitation, prism-based total internal reflection fluorescence microscopy has an improved signal-to-noise ratio over epifluorescence, making it an obvious choice when trying to improve the sensitivity of NV^- sensing measurements by removing excess signal and excitation of out-of-focus fluorescent nanodiamond (FND).

1.2.12 Super-Resolution Radial Fluctuations

Single-Molecule Localisation Microscopy (SMLM) relies on photoswitchable fluorophores to stochastically excite spatially separated emitters, which can be reconstructed post-imaging to provide images with approximately 10-100 times higher resolution than those of diffraction-limited microscopy techniques. SRRF is initially designed to aid in single-molecule localisation microscopy as an alternative that does not rely on high excitation intensities. [11] The dependence on high excitation powers (22-40 mW) is partially due to the requirements of most commercially available photoswitchable fluorophores. [26] SLML methods require thousands of images to provide a single image post-processing to collate all fluorophore positions while maintaining sufficient spatial separation.

To reduce the number of images required for high-resolution imaging and to minimise the laser power incident on a sample, SRRF is developed. This method is not sensitive to overlapping emitters within the same frame, meaning emitters do not need to be spatially separated as in other techniques. SRRF increases resolution by dividing each original pixel into smaller subpixels (e.g., 1 pixel becomes 4). It then assigns each subpixel a probability of representing an emitter, based on whether the signal at that location shows temporal correlation (indicative of an emitter) or uncorrelated noise, evaluated across multiple image frames. A key concept in SRRF is radiality, the intrinsic symmetry of the PSF around an emitter. By analysing the gradients in pixel intensity surrounding a given pixel, SRRF determines whether the local pattern is radially symmetric (correlated signal from an emitter) or random (uncorrelated noise). The repeated acquisition of images adds a temporal dimension to the data, extending analysis beyond spatial position and intensity to include temporal fluctuations. This allows SRRF to better distinguish between real emitter signals (which fluctuate in a temporally correlated manner) and noise (which fluctuates randomly and uncorrelated).

Through post-processing, SRRF reconstructs a super-resolved image without requiring mechanical modifications to the imaging system or imposing strict constraints on sample preparation.

SRRF can be applied to any imaging system where varying emitter intensity is expected to improve the spatial resolution. This work applies it to the nitrogen vacancy centre, where the emitter intensity can be controlled using microwaves or by varying the laser intensity within the field of view. Experimentation in this thesis uses the intrinsic properties of the emitter to enhance the spatial resolution of optically active emitters, enabling better region-of-interest selection.

1.2.13 Contrast Limited Adaptive Histogram Equalisation

CLAHE is another form of post-imaging enhancement. Unlike SRRF, CLAHE does not improve spatial resolution but enhances image contrast, allowing users to visualise regions with lower contrast more easily.

Equalisation goes through a mathematical process. If the intensity I of some pixel with coordinates (x, y) is $I(x, y)$, then the histogram of those intensity points can be denoted as $h(i)$ as the number of pixels with a given intensity. A normalised histogram ($p(i)$) is calculated by dividing $h(i)$ by the total number of pixels in the region (N). [27]

$$CDF(i) = \sum_{j=0}^{i} p(j) \tag{1.15}$$

$$I_{eq}(x, y) = (L - 1)CDF(I(x, y)) \tag{1.16}$$

The cumulative distribution function (CDF) is calculated from Eq. 1.15 and the output intensity after the equalisation is then given by $I_{eq}(x, y)$ in Eq. 1.16 where L is the number of possible intensity levels. CLAHE operates slightly differently; a coefficient T is used, where it is the clip limit, which is the maximum allowed bin height for the histogram, such that:

$$h'(i) = \min(h(i), T) \tag{1.17}$$

The excess, E, is then calculated:

$$E = \sum_{i=0}^{L-1} \max(h(i) - T, 0) \tag{1.18}$$

The histogram is then adjusted:

$$h''(i) = h'(i) + \frac{E}{L} \tag{1.19}$$

After producing the normalised histogram and cumulative distribution function, the final output intensity is given by:

$$I_{CLAHE}(x,y) = (L-1)CDF_{clip}(I(x,y)) \tag{1.20}$$

Because this is done on small tiles across the image, bilinear interpolation is then done to remove artefacts. If Q_n is the tile surrounding a pixel (x,y) and α and β are the fractional horizontal and vertical distances of the pixel, to blend the neighbouring tiles:

$$I_{CLAHE}(x,y) = (1-\alpha)(1-\beta)Q_1(I) + \alpha(1-\beta)Q_2(I) + (1-\alpha)\beta Q_3(I) + \alpha\beta Q_4(I) \tag{1.21}$$

Adaptive histogram equalisation reregisters a pixel's contrast relative to the surrounding pixels. A histogram of a small region is generated and normalised so that the intensity of each pixel spans the full dynamic range of the image's detection. This can lead to overamplification of pixels where no emitter is present, making the results unreliable.

However, CLAHE limits the histogram to a small region defined by the user, and noise amplification is reduced by contrast limiting: contrast above the limit is disregarded. To remove artefacts, a bilinear interpolation method is used. This is used over the full field of view and can correct the effects of stitching and tiling. CLAHE is more reliable in its output, and using it in FIJI doesn't change the assigned pixel value; it generates a look-up table rather than manipulating the image. [28]

1.3 Nitrogen Vacancy Defect

In experimental sensing work, diamond is usually classified into two types: nanodiamond, with typical particle diameters of about 1 to 1000 nm, and bulk diamond. In both cases, the sensing behaviour does not arise from an ideal diamond lattice; it stems from point defects present in the crystal, whether introduced intentionally or formed unintentionally. Among these defects, the negatively charged nitrogenvacancy (NV-) centre is particularly important because its spin states can be optically read out and it remains photostable under prolonged illumination.

Bulk diamond is often preferred when careful control of crystal orientation and low strain are required. These conditions are necessary for high-fidelity quantum measurements, such as precision magnetometry and coherent spin control, because ensemble averaging and lattice defects can otherwise mask the underlying spin dynamics. Bulk diamond is often used in experiments that study quantum-mechanical phenomena and in sensing setups that require very high sensitivity. [29]

Nanodiamond platforms are widely used in *in vitro* sensing, including temperature and pH measurements, monitoring chemical reactions via coherence-time changes, and detecting magnetic fields. Because nanodiamonds are biocompatible, resist photobleaching, and can be modified at the surface, they can be used as fluorescent markers that are directed to specific cell types or to particular locations inside cells. Their small size allows them to be placed close to specific reaction sites in biological systems, enabling spatially resolved measurements that bulk materials cannot provide.

The fluorescent intensity of the out of NV- centres is dependent on the density of NV- centres and the incident laser power. However, with increased density, the detected spin effects become more inhomogeneous; as a result, the preference for high-fidelity quantum measurement is for photon detectors, since they eliminate electrical noise. [30] For biological sensing, the laser power should be kept as low as possible to avoid phototoxicity, and widefield imaging is preferred for spatial information about the sample. Photon detectors can produce widefield images, but acquisition time depends on the field of view, whereas in CMOS, the limiting factor is exposure time. For real time imaging, acquiring a single frame needs to be as quick as possible, so CMOS is preferred. Until recently, EMCCD has been the common choice; however, CMOS detectors have improved readout noise, making them a viable option for NV- sensing.

1.3.1 Crystalline Structure

Diamond has a face-centred cubic (FCC) crystal structure, where each carbon atom forms covalent bonds with four nearest neighbours in a tetrahedral arrangement. These strong sp^3 bonds account for diamonds hardness and its high thermal conductivity.

The NV- centre is a point defect in diamond in which a nitrogen atom replaces a carbon atom and is located next to a vacant lattice site. This defect breaks the crystals local symmetry and creates discrete electronic states inside the diamonds band gap. The axis set by the nitrogen vacancy pair provides the quantisation direction for the electronic spin states, which is essential for describing both optically and microwave-driven transitions. [31]

1.3.2 Photophysics of Nitrogen Vacancy Defect Centre

Under optical excitation, most often with green light near 532 nm, NV- centres are driven from the electronic ground state to an excited state, as shown in the Jablonski diagram in the referenced Fig. 1.9. The main radiative decay process occurs between triplet states and leads to broadband fluorescence from about 600 to 800 nm, with a zero-phonon line centred at 637 nm.

In the NV- centre, the electronic ground state is a spin-triplet, and it shows a zero-field splitting of about 2.875 GHz between the $m_s = 0$ sublevel and the degenerate $m_s = \pm 1$ sublevels. Microwave radiation at a frequency close to this value can coherently induce transitions between the relevant spin states.

During optical pumping, the NV centre is driven mainly into the ground-state sublevel with $m_s = 0$ because the decay routes depend on the spin state and favour relaxation into this level. Electrons excited to the $m_s = 0$ state mainly decay radiatively back to the ground state, while about 30% of electrons excited from the $m_s = \pm 1$ states undergo intersystem crossing into a metastable singlet manifold. Relaxation along this pathway is non-radiative and produces phonons instead of photons, which lowers the measured fluorescence intensity and resets the spin to the $m_s = 0$ state [32].

The distinction between bright (radiative) and dark (non-radiative) decay pathways underlies optically detected magnetic resonance (ODMR). It is important to note that microwave excitation does not directly cause intersystem crossing. Instead, it shifts population between the spin sublevels, altering the likelihood of non-radiative decay and increasing the observed fluorescence contrast.

When an external magnetic field is applied, the Zeeman effect removes the degeneracy of the $m_s = \pm 1$ spin states, so the two levels split and appear at different resonance frequencies that can be distinguished in spectroscopy.

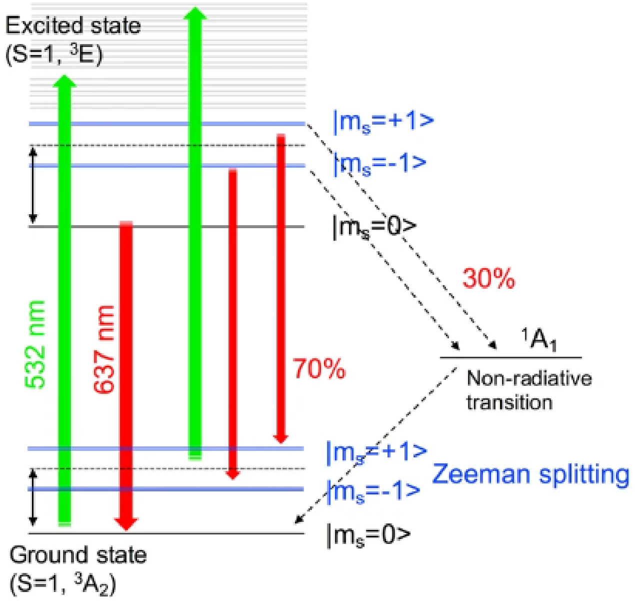

Figure 1.9: Jablonski energy diagram of the NV- centre showing the pathways for non-radiative decays, which occur 30% of the time. [33]

1.3.3 Quantum Spin State Transitions

In its ground state, the NV- centre has three electronic spin sublevels: $|0\rangle$, which has zero spin projection along the NV- axis, and $|\pm 1\rangle$, which have spin projections of $|+1\rangle$ and $|1\rangle$ along the same axis, often described as aligned and anti-aligned with it. The combined effects of zero-field splitting, magnetic interactions, and perturbations from the surrounding environment determine the energy of these spin states.

The ground-state Hamiltonian of the NV- centre can be written as follows.

$$\hat{H} = \mathbf{S} \cdot D(T) \cdot \mathbf{S} + g\mu_B \mathbf{B} \cdot \mathbf{S} \tag{1.22}$$

Here, S denotes the spin-1 operator; $D(T)$ is the zero-field splitting parameter that depends on temperature; g is the electronic g-factor; μ_B is the Bohr magneton; and B is the applied magnetic field vector.

For sensing applications, it is important to account for how D depends on temperature, $D(T)$, as well as the Zeeman interaction term. Changes in temperature lead to measurable shifts in the resonance frequencies, and an applied magnetic field splits the otherwise degenerate $m_s = \pm 1$ states. Although strain and hyperfine interactions may also modify the Hamiltonian, they are not included in the present analysis. In nanodiamond ensembles, linewidths are usually set by strain-related broadening and sample-to-sample inhomogeneity, which tends to mask hyperfine structure that would otherwise be resolved. In ultra-high-purity bulk diamond, these broadening mechanisms are reduced enough that hyperfine features can be observed.

1.3.4 Continuous Wave Optically Detected Magnetic Resonance

Continuous-wave optically detected magnetic resonance (CWODMR) is a spectroscopic method in which the microwave frequency is scanned through the resonance of the $|0\rangle$ to $|\pm 1\rangle$ transitions. At the same time, the fluorescence intensity is recorded to track the response. When the drive is at resonance, population is transferred to the $m_s = \pm 1$ states, increasing the likelihood of non-radiative decay and leading to a measurable decrease in fluorescence intensity.

In CWODMR measurements of NV- ensembles, the spectrum usually shows one or two dips, depending on whether a magnetic field causes a splitting of the resonance. These spectra are often fitted with a double Lorentzian model because Lorentzian line shapes represent homogeneous broadening mechanisms well. By comparison, Gaussian line shapes are typically used when the broadening is purely inhomogeneous, as they provide a more accurate fit. When both effects are present in nanodiamond ensembles, it is often necessary to use a hybrid or phenomenological approach to fit the data.

In Fig. 1.10, temperature changes appear mainly as horizontal shifts in the resonance frequencies, while an applied magnetic field splits the resonance minima through the Zeeman effect. These features allow thermal and magnetic disturbances to be measured simultaneously or separately.

The spectral linewidth, usually reported as the full width at half maximum, can be used to infer ensemble characteristics such as crystal strain, nitrogen content, and the influence of nearby magnetic fields [35]. Bulk diamond samples are often used to reduce line broadening caused by strain and to improve spectral resolution.

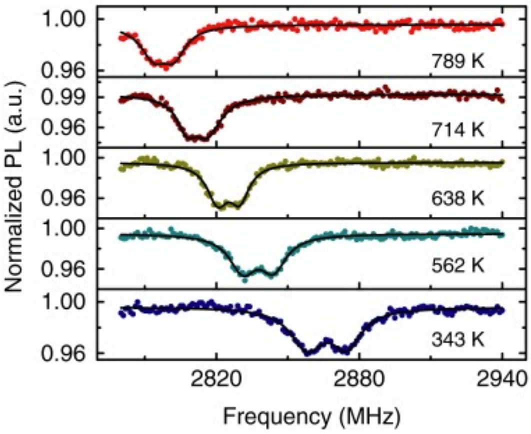

Figure 1.10: CWODMR spectra from NV- centre spectroscopy plotting fluorescent intensity against the frequency of microwaves applied, top down, the readings are decreasing in applied temperature, showing the lateral shift (frequency) associated with temperature shifts. Comparing red and dark blue, the Zeeman splitting associated with the magnetic field is apparent in the dark blue with two pronounced dips compared to the red, where only one is distinguishable. Figure adapted from [34].

1.3.5 Temperature Sensing

The temperature-dependent shifts observed in CWODMR spectra can be explained by changes in the zero-field splitting parameter $D(T)$. With higher temperature, the lattice expands, and electronphonon interactions become stronger, which lowers the zero-field splitting and shifts the ODMR resonance frequencies to higher values (a blue shift). By contrast, cooling leads to a red shift. These shifts offer a direct, quantitative way to measure temperature at the nanoscale.

Temperature is measured by monitoring shifts in the resonance frequency that align with the minima in the fluorescence spectrum. By calibrating the system, the proportionality constant that relates the frequency shift to the temperature change can be determined. Published values are often reported in the range of about -60 MHz/K to 100 MHz/K, with the exact number depending on the chosen convention and on how the experiment defines the quantity. A fuller account of the calibration methods is given in [6]. This approach allows high-resolution measurements of cell temperature under physiological conditions.

Temperature sensing exploits the $D(T)$ element in Eq. 1.22. The relative temperature shift per measurement can be calculated by observing the frequency at which the CWODMR curve is at a minimum; via system calibration, the temperature per frequency unit can be calculated; in literature, this is commonly found to be around -75MHz/K, however, this value varies across measurements and a more indepth discussion can be found in [6]. This measurement is helpful as cellular thermometry is possible with high thermal resolution.

To improve response time and accuracy of measurement, the data can be subsampled to include a selection of frequencies for scanning over instead of a full CWODMR scan; studies have been done into 3-, 4- and 6-point sampling by optimising the scanning microwave frequencies via calibration to improve the efficiency of the sensing and temporal resolution. For context, with 10 repeats per frequency, 5 MHz step size, referencing from 2.800 GHz to 2.93 GHz and a frame integration time of 200 ms, a full CWODMR scan takes 1.73 mins, 3-, 4- and 6 points for the same 10 repeats per frequency take 12 s, 16 s and 24 s respectively. The method in this work focuses on 4-point thermometry. As such, the referenced theory will correlate to the mathematics involved.

An initial CWODMR scan of the FND measurement will be used to select the four points by determining the midpoint of the curve. This can be done by evaluating the curve, subtracting the noise at the maximum and minimum values, and determining the midpoint between them. Then, the range is selected for measurement, and from this midpoint, the measurement frequencies are selected ± in the selected range as shown in Fig. 1.11.

A scan is undertaken where each microwave frequency, ω, now has a corresponding intensity (I), and so the temperature shift, ΔT, and ODMR shift estimation, $\Delta\Omega$, are calculated:

$$\Delta\Omega = \delta\omega \frac{(I_1 + I_2) - (I_3 + I_4)}{(I_1 - I_2) - (I_3 - I_4)} \tag{1.23}$$

$$\Delta T = \alpha^{-1} \Delta\Omega \tag{1.24}$$

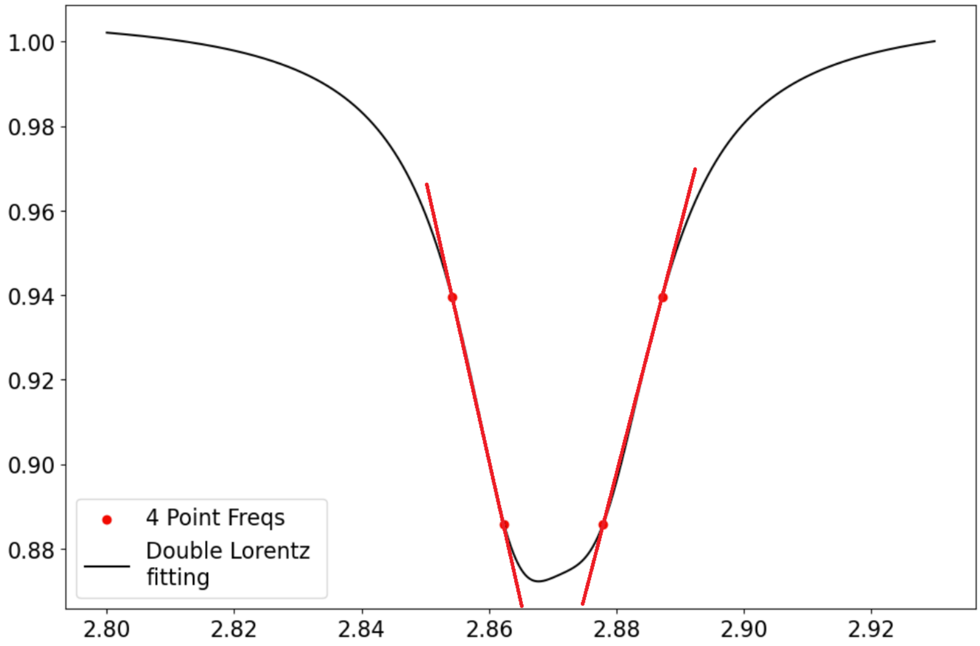

Figure 1.11: Graph of Double Lorentzian plot from measured data with selected frequencies for 4 point measurement indicated with red dots on the graph, representative of real experimental parameters employed. Red lines indicate the line plots used to determine the point of intersection of both lines from two points.

Where α is the rate dD/dT or how the frequency changes with respect to temperature, the reciprocal is used as a multiplier. A crude measurement can be undertaken by calculating a line of best fit for ω_1 and ω_2, then for ω_3 and ω_4 to track their point of intersection as it moves.

1.4 Allan Deviation

Allan Deviation is a statistical technique applied to large datasets to quantify a system's stability over time. There are many valuable resources for an in-depth explanation of the derivation of Allan Deviation from first principles to the final value; the most relied upon can be found [10]. The key equation used in this work assumes a continuous measurement process and takes the form:

$$\sigma_y^2(\tau) = \frac{1}{2m^2(M-2m+1)} \sum_{j=1}^{M-2m+1} \left\{ \sum_{i=j}^{j+m-1} [y_{i+m} - y_i] \right\}^2 \tag{1.25}$$

Where τ is the averaging time from a dataset of M measurements, and the Allan Variance, $\sigma_y^2(\tau)$ is calculated via Eq. 1.25. The square root of this gives the Allan Deviation, as shown in the plots throughout this work. The equation is illustrated pictorially in Fig. 1.12. Each point in the top line represents a data point M. For the work in this thesis, τ_0 is the initial frame integration time of the camera. The average of each k is calculated and plotted for the final Allan deviation corresponding to a given τ or number of repeats per data point as an integer multiple m. Shorter τ is high-frequency noise, and longer τ is low-frequency noise. [36] In practice, overlapping Allan deviation, which considers the average of overlapping k rather than consecutive, is considered to have better confidence intervals than the alternative non-overlapping methods since the number of sample points increases and overlapping differences are no longer statistically independent.

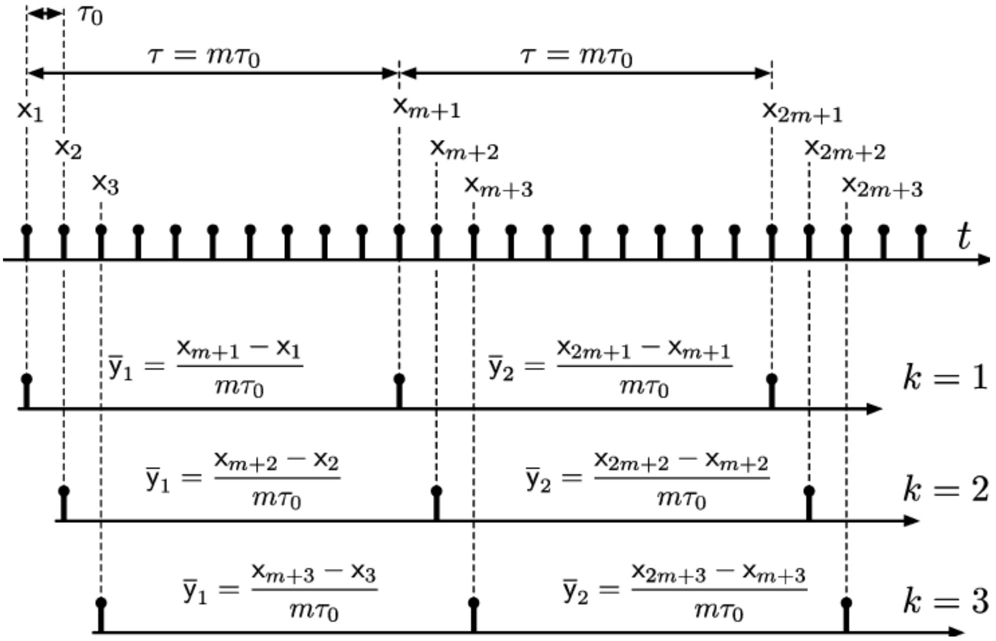

Figure 1.12: Diagram showing how overlapping Allan deviation is calculated. Figure acquired from [37].

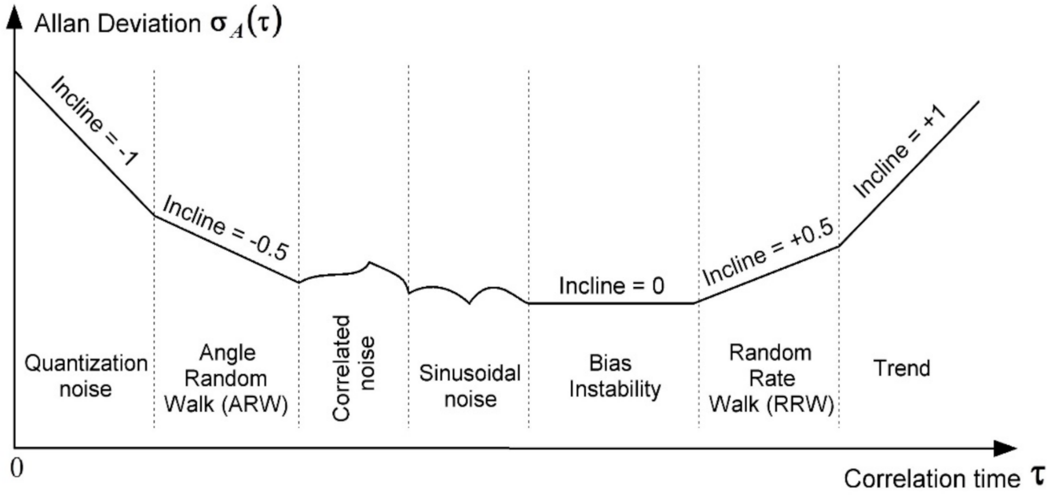

Figure 1.13: Graph showing the different types of noise detected using Allan deviation. Figure acquired from [38].

The resulting Allan deviation is plotted against the corresponding τ, similar to the graph shown in Fig. 1.13; the plot shows the varying noise, as determined from the profile. Quantisation noise refers to the sampling of data; if data is continuously quantised, the system is unaffected by internal noise. Angle random walk noise is additive, typically thermal, and can drown out the signal at sufficiently high levels. Correlated (gradient $= \pm 1 / \mp 1$) and Sinusoidal (gradient $= \pm 1/2 / \mp 1/2$) noise are seldom discussed due to the improbability of measurement, and it is unclear what causes these trends. [36] Bias instability is when no noise source contributes more than another. The rate random walk is attributed to random ambient fluctuations with long-term drift; this can be mechanical or environmental. [39]

In short, a decreasing gradient indicates that the system isn't limited by the noise it encounters; an increasing gradient indicates that the noise overwhelms the system.

1.5 Notes on Stylistic Choices

1.5.1 Terminology Substitutions

Due to overlapping research areas where key terms have varying meanings, some areas of this work have had to be defined to specify which definition is being discussed. One term is ’contrast’, which is used interchangeably with different definitions throughout this work, all of which converge in the discussion. To limit confusion, the following terms will be used in place of:

- **Image Contrast**: the phenomenon that arises in an image due to the dynamic differences between structures from high fluorescent intensity to low fluorescent intensity.
- **Dip Depth**: the contrast which arises when undertaking ODMR, the loss of fluorescence caused by the microwaves exciting at energies resonant with the ground spin state transitions.

Another instance of this is ’noise’; there are multiple definitions of noise, which will be defined as:

- **Image Noise**: the variation seen across an image; this variation is due to the properties of camera acquisition and is contributed to by the factors discussed in section 1.2.6
- **Image signal-to-noise ratio**: the ratio between the signal collected and the image noise.
- **ODMR Noise**: the noise present within the ODMR scans, taken as the standard deviation in a single frequency point average, producing the error bars present in each plot.

1.5.2 Importance of Acquisition Schemes to Measurements

Parts of this work directly investigate the effects of acquisition schemes as a means of characterisation, so it is essential to disclose this to draw a reasonable conclusion.

Secondly, the conclusions of that work require ensuring that the measurements being compared are like-for-like. Further, the Allan Variance investigations rely primarily on the frame integration time for processing and understanding how the data are processed; this is key to understanding how the data is acquired.

The dip depth measured in CWODMR is statistically linked to the signal-to-noise ratio and to the number of counts detected by the camera. The imaging criteria in this thesis aim to minimise background noise whilst still improving photon collection by increasing exposure time and limiting gain. Fig. 1.14 shows how the relationship between dip depth and signal-to-noise ratio varies depending on the counts collected by a camera for fluorescence and background. These graphs are produced by setting arbitrary fluorescent counts (200 and 2000 in the graphs provided), which are then added to the background value to obtain total counts detected. This allowed calculation of the signal-to-noise ratio and dip depth, which could then be plotted to show the inverse relationship.

As the signal-to-noise ratio decreases, the possible dip depth (contrast of CWODMR) decreases as well; this is evident: at signal-to-noise ratio = 0.02, with 200 fluorescent counts, the detectable dip depth is 1% compared to 8% at signal-to-noise ratio = 0.02. As such, the camera settings, microwave generator settings, ODMR scan parameters, and sample type are highlighted for each measurement, as these acquisition schemes can greatly alter the measurement outcome.

1.5.3 Fluorescent Nanodiamond Selection for Sample Preparation

FNDs vary in size and density of NV- centres within each FND. This density of NV- centres will determine the achievable image contrast with similar excitation powers and acquisition schemes. The higher the density of NV- centres, the better the image contrast, as more emitters are imaged. This usually means larger FNDs containing more NV centres, so using a larger FND reduces the frame integration time and gain required to image a sample. This works brilliantly in situations where the primary concern is overcoming background from another emitter in the field of view.

However, larger FNDs are less sensitive to environmental changes. This is suspected

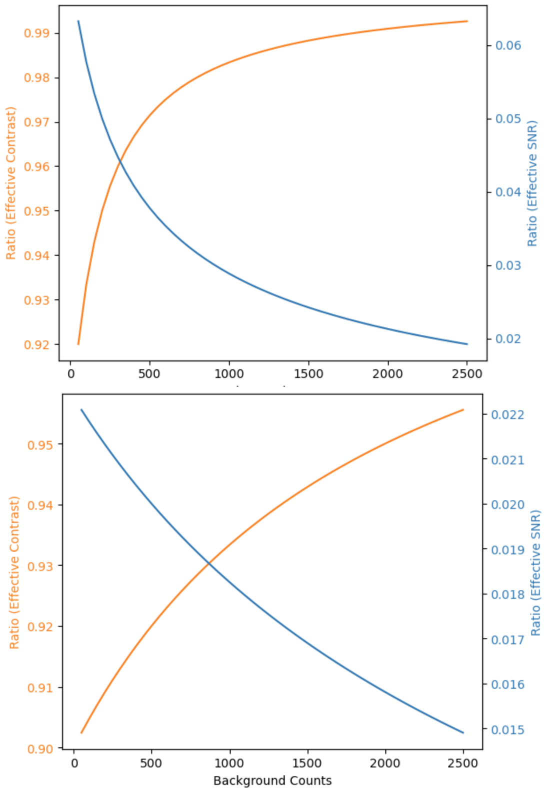

Figure 1.14: Modelling demonstrating the effects of background and fluorescence signal on the effective contrast (dip depth) and effective signal-to-noise ratio in a CWODMR scan. This varies depending on the number of counts recorded on a camera for fluorescence and background. These graphs show fluorescence counts for (top) 200 and (bottom) 2000, with a background signal of 50 counts.

to be because the NV- centres at the centre of the FND are less affected by environmental changes than those at the surface, yet they still contribute to the FND's fluorescence spectra. For temperature measurements, this means that, ideally, the larger the FND, the better it responds to environmental changes, since the structure is closer to the bulk diamond. Recently, this has been disputed by the manufacturer of FNDs with properties similar to bulk diamond, whilst having a rough size of 100 nm; these FNDs are specially manufactured and not readily available for measurements. [40]

During this work, the diamond size varies from experiment to experiment. For FND characterisation, measurements are usually acquired using 90 nm FND because sensitivity is not required for sensing, enabling faster acquisition. Finally, sections involve measurement with 100 nm FND. This is typically observed in samples with excessive background, for various reasons, which allowed the fluorescent output to at least compete with, if not exceed, that of other emitters in the field of view, facilitating measurement.

1.5.4 The Inclusion of HeLa Cells

HeLa cells are an immortalised cell line derived from the cervical cancer tumour of Henrietta Lacks in 1951. Henrietta was a 31-year-old African American who sought treatment for her aggressive cervical cancer at Johns Hopkins Hospital, the only hospital that would treat African American patients. During this time, and after her death, samples were taken and provided to a researcher without consent. The name HeLa was chosen to protect Henrietta's privacy. It was discovered that these cells rapidly divided and does not die after a few divisions, unlike other cell lines, making them a good choice for long-term laboratory experimentation, leading to their immortalisation.

Her cells have been highly influential in scientific research; between 1953 and 2018, over 110,000 papers have used HeLa cells. The first notable use of her cells was the development of the Polio vaccine in 1952. It has been used to prove human papillomavirus (HPV) causes cancer (1984), determine the infection mechanism of HIV (1986) and many other studies. In 1973, the family was contacted to provide blood samples after HeLa cells contaminated other cell lines in the laboratory. This is how the family found out that Henrietta's cells were being used in research.

At the time of collection, it was legal to collect specimens from patients without consent; the Lacks family, alongside scientists, have worked to change this so that consent is required before the biological specimens are used in research. The attempt to change to the Common Rule failed in 2017. When genome sequencing began circulating, the family requested that the papers be retracted due to privacy concerns, as they contained their genetic information. The National Institutes of Health (NIH) agreed that this data is now available only to researchers who apply and are granted permission by the committee, which has two family members. Further, in 2023, Thermo Fisher Scientific paid a settlement to the family for profiteering from Henrietta's cells. The family is not calling for a cessation of experimentation; rather, they are calling for accountability to ensure that research outputs are equitable and that her legacy is recognised.

This work uses HeLa cells to characterise total internal reflection fluorescence excitation. Given the controversy and ethical concerns surrounding the collection and continued use of HeLa cells, it is important to acknowledge the wrongs of previous generations and to be aware of the history of the cells that catapulted our scientific understanding.

Chapter 2

Optical Design and Calibration

2.1 Introduction

Diffraction-limited systems are those in which light's wavelength limits resolution. These systems can be improved using post-imaging analysis such as super-resolution radial fluctuations (SRRF) microscopy. [11] Techniques such as epifluorescence and total internal reflection fluorescence microscopy are diffraction-limited laterally despite the improved axial (Z-axis) resolution provided by total internal reflection fluorescence. [41, 42] Another example of diffraction-limited microscopy is confocal microscopy, where the system rejects out-of-focus light, improving the resolution. However, the resolution still depends on the fluorescence emission wavelength. [43]

Super-resolution systems overcome the classical diffraction limit using a variety of different mechanisms. STimulated Emission Depletion (STED) microscopy, for example, achieves this by having two beams depletion and excitation. The excitation beam is the wavelength that will excite the structure into fluorescence, and the depletion beam has a phase shift from a phase mask that only allows a small area of the excitation beam through the centre with a wavelength that will cause de-excitation in the structure, effectively reducing the area of excitation and increasing the resolution. [44] STochastic Optical Reconstruction Microscopy (STORM) relies on the stochastic activation of individual fluorophores with photoactivable properties. Fluorophores blink through randomised excitation, and their position is localised and mapped to build an image. [45] STED has a high-power density at the sample, which can cause burning or photobleaching or is not a good option for live biological samples. STORM is limited by the available fluorophores for photoactivation, which may not be suitable for an experimental setup. Even so, research has been conducted using STED for live-cell measurements in mammalian cells expressing Citrin-tubulin and epidermal growth factor in human embryonic kidney cells, achieving a resolution of 80 nm. [46]

Where a large field of view is required, there is a trade-off between the numerical aperture and the field of view since a reduction in numerical aperture reduces the angle over which fluorescence can be detected. Manipulating the numerical aperture to magnification can enlarge the field of view whilst maintaining cellular resolution in systems such as the Mesolens. [47] The Mesolens provides a 4 x magnification combined with a 0.47 numerical aperture, which translates to a field of view of 6 x 6 x 3 mm and a lateral resolution of 640 nm. Computational alternatives include stitching and tiling methods, in which an image is acquired, and either the sample or the detection is moved in the imaging plane. Another image is acquired, where these images are then computationally joined, increasing the effective field of view. [48] Stitching and tiling is a lengthy process where artefacts are typically produced with non-linear illumination, causing banding at the stitch of the image. Overlapping images can be acquired and overlapped, though this increases acquisition time.

Excitation in most fluorescence microscopy systems utilises lasers for their coherent output and higher power density than light-emitting diodes (LEDs). Lasers come in a variety of powers and wavelengths, selected to match the experimental parameters required. [49] There are techniques to reduce speckle and inhomogeneities in the beam profile, such as vibrating the laser fibre. Methods like total internal reflection fluorescence and light-sheet microscopy reduce the excitation volume by shrinking the beam profile; total internal reflection fluorescence via the evanescent field, and light-sheet microscopy via beam focusing into a thin strip. [42], [50]

Detection has various options, again, dependent on the measurement being recorded, and cameras are predominantly used for widefield detection in this research. Cameras come in a variety of configurations from sCMOS to CCD to EMCCD, each camera increasing in sensitivity (as well as cost) with higher photon detection sensitivity in EMCCD than that available in sCMOS. Photomultiplier tubes (PMT), typically used in confocal microscopy, do not provide spatial information but are very sensitive to photon collection. PMTs are a good choice if the experimental parameters rely solely on the fluorescent output, rather than on spatial information, unless used in a configuration such as a scanning confocal, where images are built pixel by pixel.

The optical design in this work is prompted by a need for a system that is sufficiently simple for non-experienced users and still enabled wide-field imaging for biological samples. The design presented in this work has two modalities with microwave implementation: epifluorescence microscopy and total internal reflection fluorescence microscopy. Epifluorescence benefits from a simple alignment procedure with fewer optics. Total internal reflection fluorescence is a more complicated system; however, using a rooftop prism makes alignment easier, as total internal reflection fluorescence occurs when the excitation beam enters the prism parallel to the table, avoiding the need to fine-tune the angle of entry manually and providing enhanced optical sectioning, a benefit for more complex measurement schemes. Further, the camera utilised is a standard mid-range CMOS, making this system a fraction of the cost of that usually employed.

2.2 System Design

An optical system is designed to enable dual fluorescence using total internal reflection fluorescence and epifluorescence methods. The system's resolution had to be sufficient to resolve the fluorescent nanodiamond (FND). A theoretical resolution of 248 nm is calculated; the effective pixel size at the sample plane is 55 nm, thus the system is oversampling the Nyquist limit. The microwave delivery system is also presented in Fig. 2.1.

Epifluorescence is achieved using an RGB laser (Compact-RGB laser with FC Connector, Alrad Instruments, United Kingdom) delivered via a multi-mode fibre (540 nm, 520 nm and 635 nm at 60 mW); the output of the fibre is collected using a condensor lens (ACL50832U, ThorLabs, Germany) to focus onto the back aperture of the objective lens (421090-9902-000, Zeiss, United Kingdom) with 100x magnification, numerical aperture of 1.45 and oil immersion. A dichroic mirror (Di02-R532-25x36, Laser 2000, United Kingdom) is used to position the focused light onto the objective lens back aperture, and a beam dump is utilised to collect unwanted transmission through the mirror. Focusing on the back aperture produces a beam parallel with the objective lens that fills the field of view, giving epifluorescence illumination.

Total internal reflection fluorescence excitation is generated by a 532 nm laser diode with maximum power 300 mW (MSL-FN-532nm-300mW-19061472, Changchun New Industries Optoelectronics Tech. Co., China). Using a 1/2 λ waveplate (WPQ10E-532, ThorLabs, Germany) and a polarising beam splitter (CCM1-PBS25-532/M, ThorLabs, Germany), the power can be tuned, and the excess power reflected into the beam dump. A beam expander (GBE05-A, ThorLabs, Germany) is put in reverse to reduce the size of the beam from 3 mm to 0.6 mm, and a cylindrical lens (LA1708-A-ML, ThorLabs, Germany) is used to focus and shape the beam further before entering the prism (PS991, ThorLabs, Germany). By placing a mirror directly in front of the prism, the beam angle entering the prism can be adjusted to illuminate different regions of the sample. The prism is cut at an angle, so if the beam enters the prism parallel to the table, an evanescent field is generated at the centre of the prism surface. The light that is not transferred into the evanescent field exits the sample and is collected by a beam dump.

Detection is performed via a common path for both modalities. Light is collected at the sample by the objective lens, transmitted through the dichroic mirror (Di02-R532-25x36, Laser2000, United Kingdom), and passed through a filter (FELH0650, ThorLabs, Germany) to remove the excitation wavelength and only collect Nitrogen Vacancy (NV-) centre emission. A tube lens (TTL165-A, ThorLabs, Germany) then focuses the image on the camera sensor (CU235MP, ThorLabs, Germany).

The acquisition is controlled via a computer which connects to the camera and microwave hardware. Both frequency generators (TGR6000, Aim-TTi, Germany) (USG-LF44, GW-Instek, United Kingdom) for the microwave generation in ODMR measure-

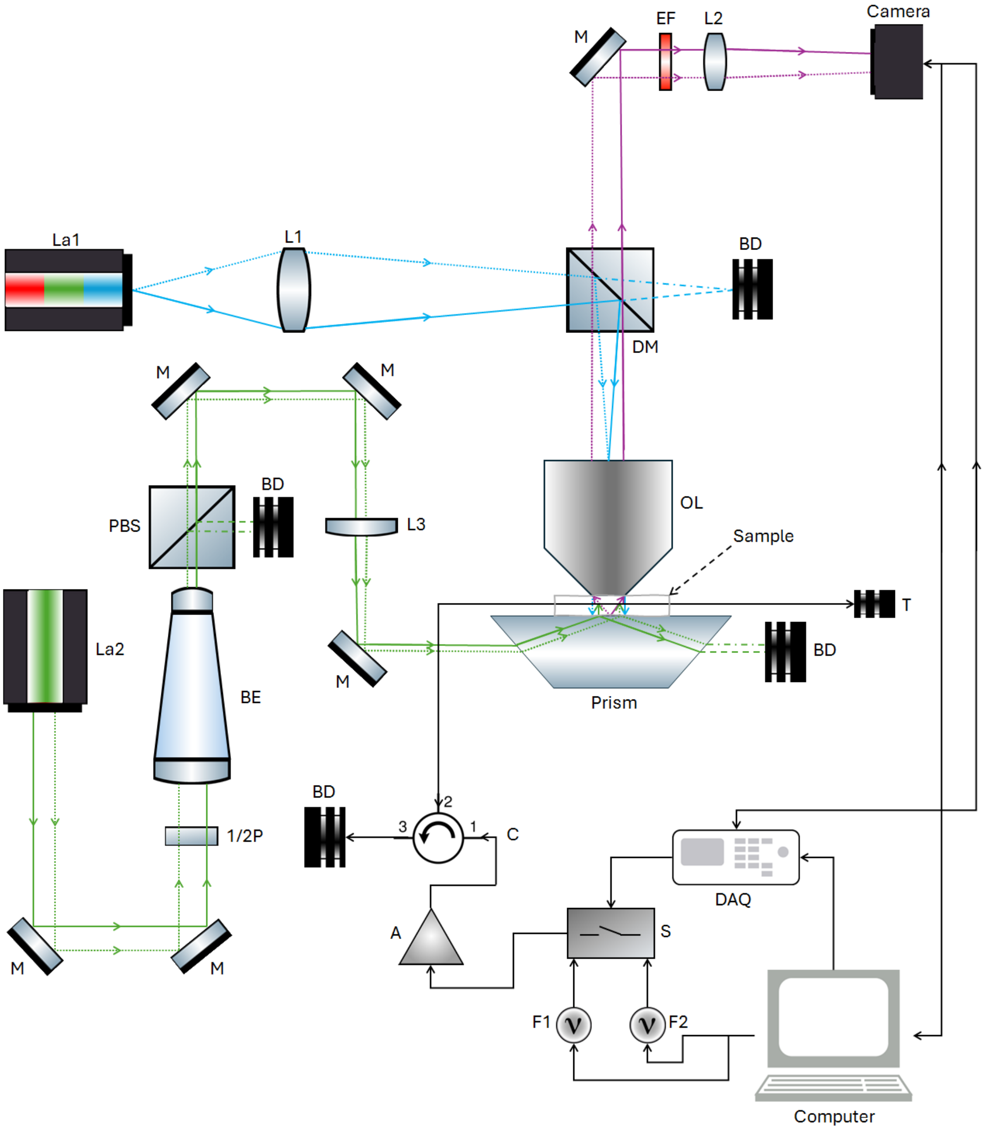

Figure 2.1: Ray diagram presenting the microscope used in this work. The epifluorescence system consists of La1, an RGB laser diode; L1, a condenser lens; DM, a dichroic mirror; and OL, an objective lens. Total Internal Fluorescence Reflection excitation is La2, 532 nm Laser diode; M, mirrors; 1/2P, 1/2 waveplate; BE, 5x beam expander reversed; PBS, polarising beam splitter; L3, focusing lens; and prism. Fluorescence collection starts at OL and passes through DM; M redirects to EF. The emission filter is a 650 nm long-pass filter, L2 is the tube lens, and the camera is a Thorlabs CU235MP CMOS. Microwave excitation is controlled by the Computer and DAQ, Data Acquisition module; microwave delivery is via F1, scanning generator, and F2, reference generator; S, switch, allows selective throughput; A, amplifier; C, circulator; to BD, beam dump, or Sample ending at T, terminator. Green shows total internal reflection fluorescence excitation, blue is epifluorescence, and purple is the fluorescent emission ray diagrams.

ments are fed through a microwave switch (ZASWA-2-50DR+, Mini-circuits, United States) with TTL control via DAQ (BMC-2110, National Instruments, United States) to allow one microwave frequency to pass onto the microwave amplifier (AM64-2.7-3.1-40-40, microwave amps, United Kingdom). A circulator (PE83CR1004, Pasternack, United States) is used to direct any microwaves reflected from the sample interfaces into a microwave beam dump. Microwaves that pass through the sample are collected in a terminator.

The intention had been to use two USG microwave generators; however, their outputs contained multiple harmonics that could interfere with the measurements, so the decision is made to include a TGR6000 microwave generator with a narrow-linewidth output for scanning frequencies. The USG microwave generator is used as the reference frequency, since dependence on a single harmonic is less crucial, as the frequency is chosen to be sufficiently off-resonant. Reference frequencies needed to be included because, without normalisation, the CWODMR scans could not reliably generate data suitable for NV- spectroscopy, as longer frame integration times increased noise in the spectrum. LEDs were tested for excitation in place of laser excitation, however, the power density at the sample is insufficient to produce NV- centre emission at sufficiently high intensity within the time limitations of data acquisition, as evidenced by the inability to produce images in which the NV- centre fluorescence is detectable. Finally, the inclusion of the 532 nm laser is due to its sufficient power output (330 mW at the source) for total internal reflection fluorescence excitation of NV- fluorescence; lower power densities led to issues similar to those observed with LED excitation. This system is designed with as few optical and microwave hardware components as possible, resulting in a compact system suitable for NV- centre spectroscopy.

2.3 System Characterisation

Characterisation of the microscope involved calibration of the effective magnification, the effective pixel size at the sample, and the field of view. All measurements are acquired from a single brightfield image of a graticule loaded in FIJI. [28]

A line profile is taken across the graticule, and the full width half maximum is identified, such that the number of pixels between the start of a line in the graticule and the start of the concurrent line is determined. The distance between these lines is known to be 10 microns. By dividing 10 microns by the number of pixels, we found that the adequate pixel size at the sample plane is 55 nm. By multiplying the effective size of the pixel at the sample plane by the number of pixels on the detector, the field of view is 105 x 66 μm. Dividing the sensor's physical size by the field of view yields a magnification of 94x, which could be brought to the nominal 100x by adjusting the distances between the objective lens, tube lens, and detector.

Optical resolution is characterised using FND imaging. Since the 90 nm FND is smaller than the diffraction limit of the microscope, it can be assumed to be an infinitely small emitter, hence the full-width-half-maximum is equivalent to the measured resolution. Using a nebuliser, 90 nm FND are adhered to a coverslip, using deionised water as a mountant, and sealed with commercially available nail polish. Image acquisition is performed in epifluorescence with a 520 nm laser excitation and a power of 40 mW at the source. Using FIJI, a line is drawn through the centre of an emitter, and a plot profile is produced; the fit is set to Gaussian, and the σ value is obtained. Multiplying σ by 2.350 gives the full-width-half-maximum of the Gaussian fit. An average of 5 emitters found the σ to be 0.101 times 2.350, yielding a resolution of 290 nm. For this system, the theoretical diffraction limit is 270 nm for a 650 nm emission wavelength. This measurement could be slightly out of focus, leading to a slight discrepancy from the theoretical value.

2.4 Characterisation of Total Internal Reflection Fluorescence Microscopy

2.4.1 Numerical Modelling

Due to the ease of preparation, the use of a rooftop prism ensured the user knew the expected geometries for total internal reflection criteria to be met, so the laser entered parallel to the optical table for total internal reflection fluorescence excitation to be viable. Employing Snells Law (Eq. 1.7) allows the calculation of the angle when entering the prism and is found to be 41^o, if the assumption is made that the beam is entering exactly central to the prism face (5 mm height and width) and focusing on the centre of the prism (21 mm from the edge of the long top) it can be determined using trigonometry that the angle of incidence normalised to the prism face is 73^o corresponding to a penetration depth of 74 nm.

Total internal reflection fluorescence characterisation and calibration is calculated mathematically using Eq. 1.13 and Eq. 1.14 to obtain theoretical values for perfect alignment, dependent on the angle of incidence and its correspondence to the penetration depth and laser intensity. The values for the calculation are: the initial excitation wavelength is 532 nm, the refractive index of glass is 1.52, and the refractive index of water is 1.33. If theoretical perfect alignment is achieved, the penetration depth is 990 nm at the critical angle of 61^o; however, because the imaging system is explicitly designed to compensate and allow alignment throughout the prism volume, we will also include the smallest possible penetration depth with the angle of incidence at 80^o, which provides a penetration depth of 61 nm. The reduction of the penetration depth as a function of the angle of incidence is presented in Fig. 2.2

To mathematically determine the effective power at the sample plane in a given sample, two assumptions are made:

1. Optical losses from the laser entering the prism is 8% as provided in the specifications of the prism from the manufacturer.
2. The depth at which the intensity measurement is calculated (using Eq. 1.14) corresponds to the centre of a particle sitting directly on the surface, and so is equivalent to the nominal radius of the fluorescent microsphere or FND being measured.

Numerical modelling of the angle of incidence as a function of the resulting laser intensity at the height of the sample from the surface is shown in Fig. 2.3. The intensity at the height of the structure decays exponentially with increasing angle of incidence, enabling imaging of larger structures, such as microspheres. Calculating the precise

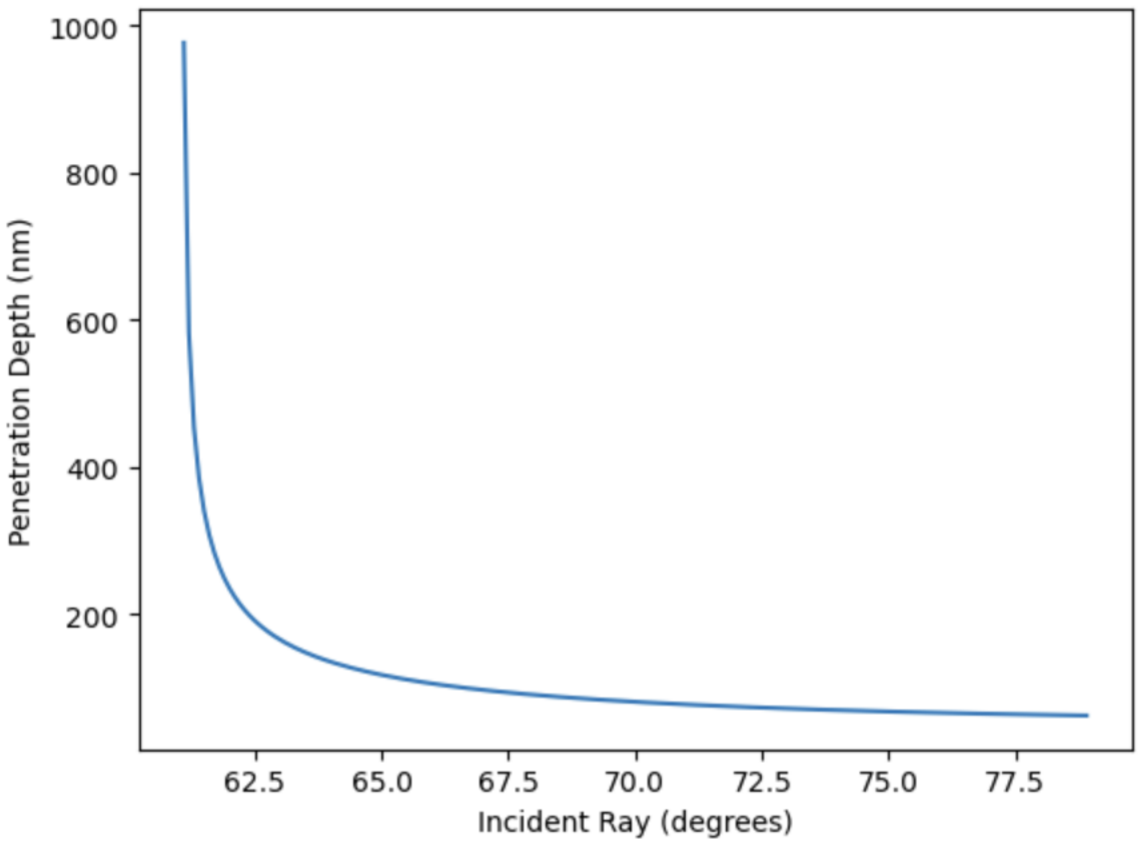

Figure 2.2: Numerical Modelling of penetration depth of the evanescent field at 532 nm as a function of angle of incidence ranging from 61^o to 79^o.

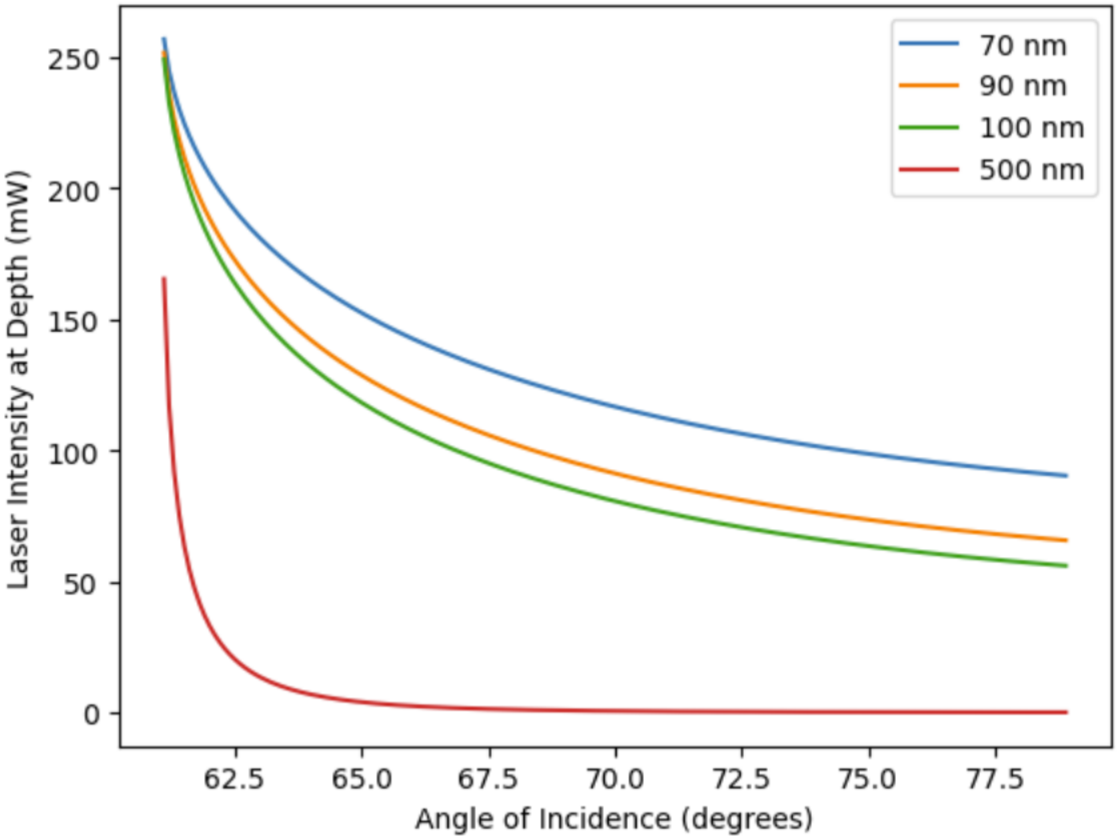

Figure 2.3: Numerical simulation of the laser intensity for varying penetration depths and the relationship to the angle of incidence.

height of the beam path relative to the prism entry, as this alters the angle of entry to the same spot at the prism's end facet, is the best way to ensure the greatest throughput from laser excitation.

2.4.2 Results - Optical Sectioning in HeLa Cells

A key benefit of using total internal reflection fluorescence is the enhanced optical sectioning over epifluorescence excitation. To visualise and characterise this improvement, it is beneficial to examine focal adhesions in HeLa cells; these structures are present throughout the cell and are directly in contact with the coverslip. Optical sectioning improves when epifluorescence shows poor structural localisation, with out-of-focus fluorescence within the depth of field. However, the total internal reflection fluorescence shows a significant improvement in localisation due to small-volume excitation limited to structures closest to the coverslip and the removal of out-of-focus emission.

Qualitatively, there is notably less fluorescence observed in Fig. 2.4 in the total internal reflection fluorescence excitation due to the superior optical sectioning, as out-of-focus structures are not excited. In epifluorescence, the localisation of individual structures is indistinguishable from that under total internal reflection fluorescence excitation, especially in the area where the yellow line passes; this line corresponds to the intensity profile shown in Fig. 2.5.

The first notable difference is that the raw fluorescent profile shows a much higher output in the epifluorescence sample because many out-of-focus structures can constrain the ability to distinguish structures. The laser power can be comparable before entering the sample; however, only a small fraction (approximately 10%) of the light entering the prism is transferred to the evanescent field, whereas the epifluorescent field carries the same power as the incident light.

Further, the total internal reflection fluorescence excitation allows the user to distinguish at least two structures that the epifluorescence hides behind out-of-focus fluorescence, as shown in the normalised plot. The normalised plot indicates that the edge of the structure is overcome with out-of-focus emission in epifluorescence by comparison to the total internal reflection fluorescence, where the peak at 3.5 micron is half the intensity of the peak at 10-11 micron (and 20% less than the epifluorescence signal at this point), which is comparable to the epifluorescence intensity.

2.4.3 Discussion

Total internal reflection fluorescence offers optical sectioning, unlike epifluorescence. This can allow better control of multi-channel excitation because fluorescent nanodiamonds can be excited using total internal reflection fluorescence separately from photosensitive fluorophores or chemicals, which can be excited using epifluorescence, so that photosensitive samples are not constantly excited by FND's excitation wavelengths.

A significant drawback of the total internal reflection fluorescence excitation is poor optical power transference from the excitation beam to the evanescent field, which

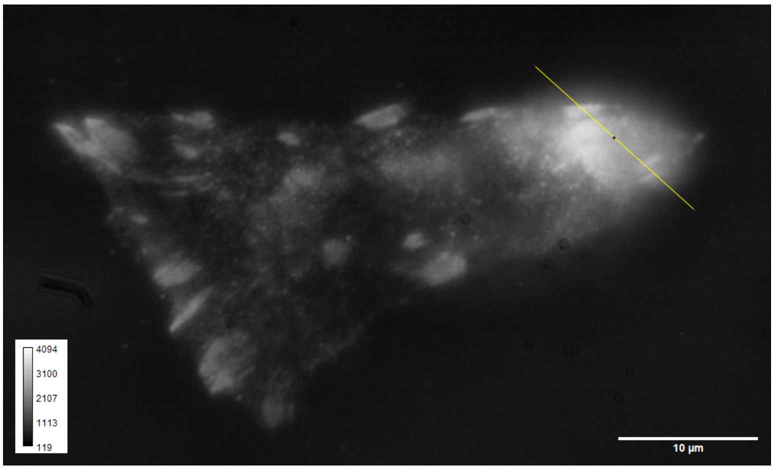

(a) Widefield Epifluorescence

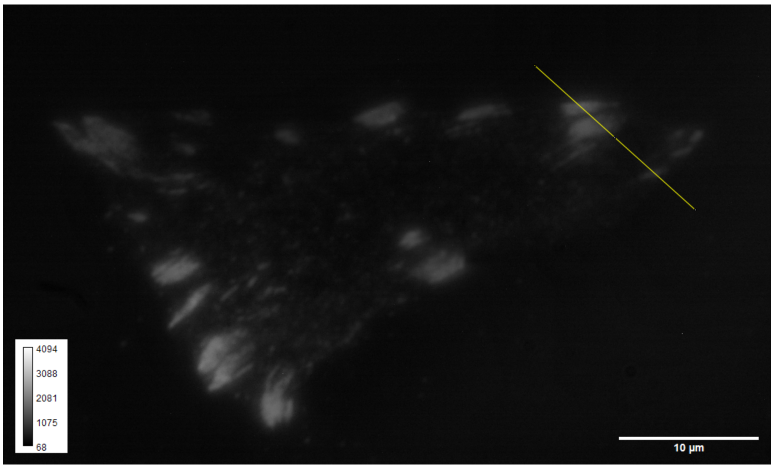

(b) Total Internal Reflection Fluorescence

Figure 2.4: Images of HeLa cells with Alexa488 bonded to the focal adhesions via paxillin, yellow lines are the region of interest for the line plots used in Fig. 2.5.

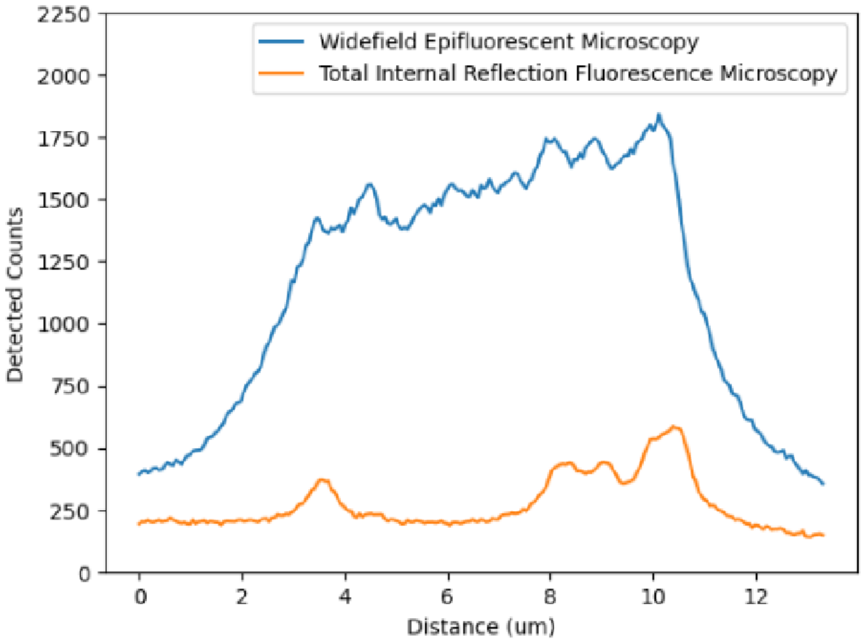

(a) Raw Fluorescent Output

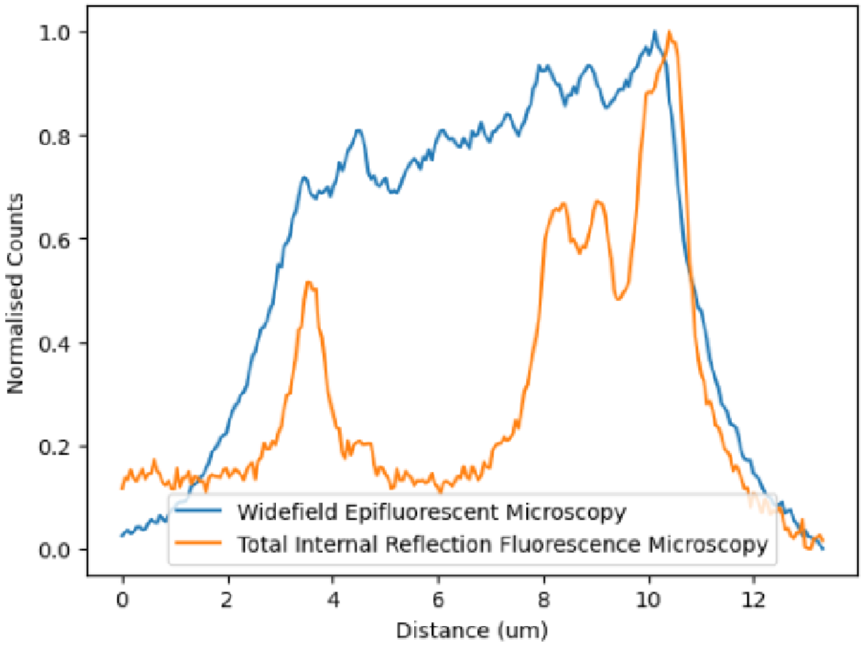

(b) Normalised Fluorescent Output

Figure 2.5: Line intensity plots from a single plane showing the lower background and increased spatially varying features of total internal reflection fluorescence vs epifluorescence optical sectioning.

means less optical excitation of any structure. However, this can be mitigated by adjusting the camera control to improve photon collection, using camera gain to multiply the collected signal, or increasing the frame integration time to increase the time available for photon collection.

2.5 Laser Noise

Initial experimentation focused on the system's optical characteristics to characterise the stability of each modality and evaluate improvements in optical sectioning between modalities. To determine the best method for evaluating these parameters, it is decided to initially conduct these experiments with fluorescent microspheres rather than fluorescent nanodiamonds (FND). Fluorescent microspheres are more efficient (higher fluorescence detected at a lower exposure time) at producing fluorescence than the FND available; more FND could have been acquired with a higher concentration of optically active centres; however, with appropriate fluorescent microspheres available, this seemed redundant.

2.5.1 Sample Preparation and Acquisition Schemes

Before imaging FND, we wanted to test the optical stability of our microscope. Samples are prepared by dry adhering (depositing a liquid suspension and allowing the liquid to evaporate) fluorescent microspheres (FluoSpheres F8812 (580/605 nm), Thermo Fisher, United Kingdom) to a 16 mm round coverslip. After the water had evaporated, deionised water is used as a mountant, and the slide is sealed with a 13 mm round coverslip and commercially available nail polish. To obtain efficient total internal reflection fluorescence illumination, there must be no additional refractive index changes close to the region of the sample being imaged, apart from the glass/sample medium transition. In practice, this means that the coverslips used to mount the sample should themselves be mounted on the roof prism using refractive-index-matching immersion oil, so that the evanescent field is produced at the coverslip rather than at the prism, which would not excite the sample due to the small volume of excitation.

To test the noise within the system, 5000 images are acquired continuously at 25 ms and 100 ms frame integration times for both total internal reflection fluorescence and epifluorescence modalities, corresponding to total imaging times of 2 minutes and 8 minutes, respectively. This provides two different frame integration times, facilitating comparisons of noise at a large and a small frame rate. The camera gain is set to 0 dB to limit camera noise during the experiment. Image processing is completed using FIJI, where stacks are loaded and lateral drift corrected for using the NanoJ drift correction plugin. [11],[28] A 5x5 pixel region of interest is selected that is visible in both epifluorescence and total internal reflection fluorescence modalities, and the plot Z-axis function is used to extract the mean fluorescent output of that region of interest for each frame. Similarly, no region of interest is selected across the entire field of view, and the plot Z-axis function is used to extract the average fluorescent intensity for each frame. Z-plot data is saved as a .txt file and opened in Python (JupyterLab standalone software) for plotting using custom code.

2.5.2 Results - Full Field of View

Measurement of laser noise over time is a valuable characterisation for microscopists studying fluorescence fluctuations, since fluctuations can cause unreliable results in time-dependent fluorescence measurements, especially in small regions of interest. Other factors contribute to the stability of the measurement: mechanical stability of the system (e.g. stage drift) can cause physical movement of the sample with respect to excitation and detection; temperature stability of the ambient temperature affects the noise characteristics of the camera, causes expansion and contraction of optomechanics, and can affect the fluorescent properties of some emitters; and external physical movement (e.g. vibrations introduced via construction works) can contribute to instability.

Some of these perturbations - such as lateral drift - are easily corrected using software; the use of an optomechanical table that is isolated from the building increases the physical stability of the optomechanics and provides thermal isolation by acting as a crude heat sink. After correcting for mechanical instability, fluctuations in continuous fluorescence measurements from a sample indicate the camera and laser stability.

When an optical power meter records no laser power fluctuations but fluorescent intensity varies across an image, this indicates non-uniform excitation across the field of view. Camera instability would also be evident in the background of the images as fixed-pattern noise across the field of view. The entire field of view is an optimal place to start determining the fluorescent fluctuations affecting the sample as a whole and the effective signal-to-background ratio.

Comparison of the graphs in Fig. 2.6 shows the instability of the laser excitation using the multi-mode fibre in epifluorescence, compared with the single-mode total internal reflection fluorescence excitation, with intensity fluctuations across the field of view rather than background noise. These fluctuations highlight the need to reduce their effects in time-dependent fluorescent data via normalisation to a reference. Further, a comparison of the effective fluorescence across the entire field of view shows the lower background in total internal reflection fluorescence. This is due to the smaller volume of excitation provided by an evanescent field (which is always smaller since the height of the excitation is limited), in contrast to the difference in the total volume in epifluorescence. The total internal reflection fluorescence evanescent field for excitation wavelength 532 nm ranges from penetration depths of 732 nm at 61^o angle of incidence to 61 nm at 80^o. Due to the geometries and alignment method, it is difficult to determine the angle of incidence in this setup, and it must be measured for each sample. Therefore, total internal reflection fluorescence alignment is ensured by measuring the optical power of the exciting beam before and after the prism. If the measurement post-prism is within 15% of the pre-prism measurement, it can be assumed this is total internal reflection fluorescence alignment; otherwise, a more significant loss would be anticipated from expected optical losses via reflection at interfaces in the process of total internal reflection within the prism.

2.5.3 Results - Region of Interest (Widefield Epifluorescence)

Fig. 2.7(a) shows a lower fluorescent intensity detected and higher frame-to-frame noise in comparison to Fig. 2.7(b), which has a higher frame integration time. Fluctuations over time show a pattern of fluorescence with poor temporal coherence of excitation

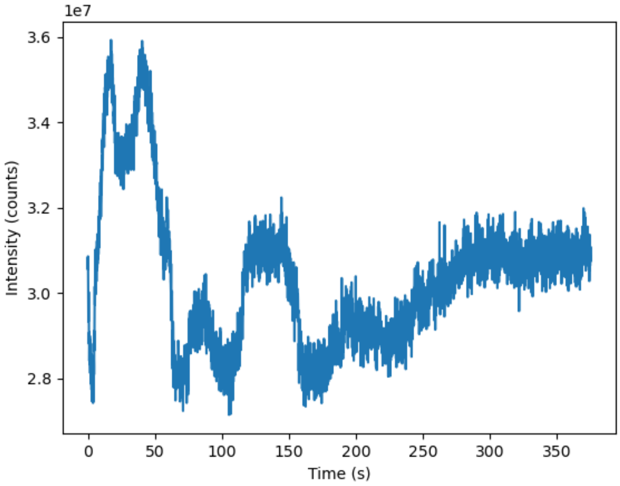

(a) Widefield Epifluorescence

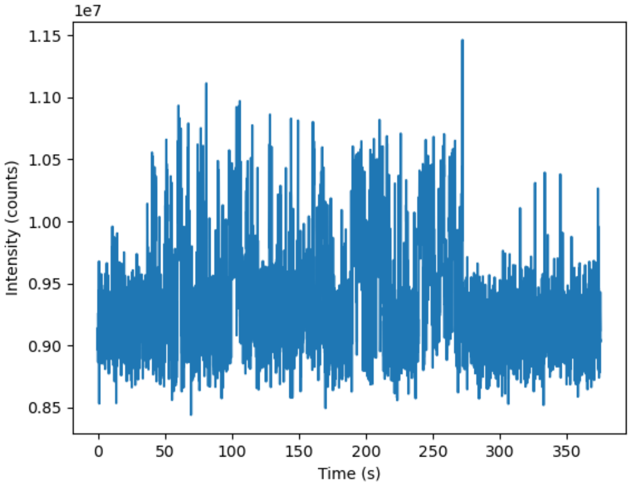

(b) Total Internal Reflection Fluorescence

Figure 2.6: variation of the fluorescent output of fluorescent microspheres over a full image with excitation using (a) epifluorescence and (b) total internal reflection fluorescence with a 25 ms frame integration time as a function of time.

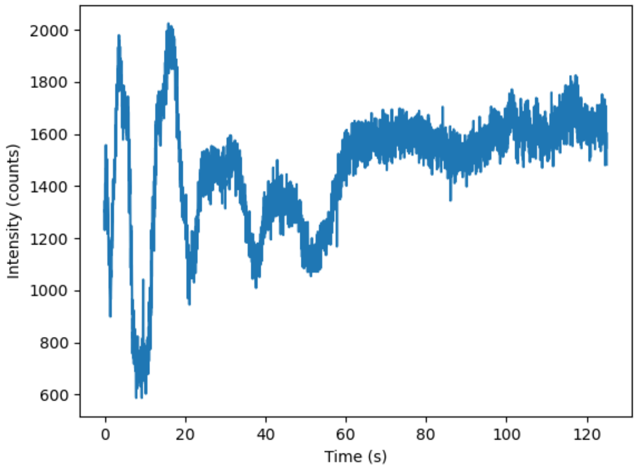

(a) 25 ms

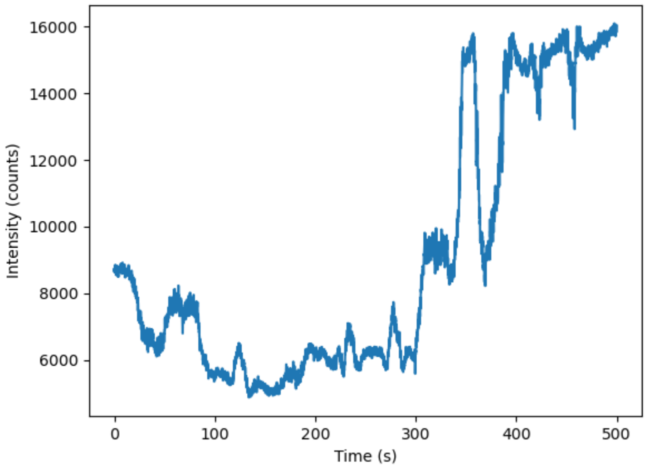

(b) 100 ms

Figure 2.7: Variation of the fluorescent output of a fluorescent microsphere in a region of interest 5x5 pixels in size for both (a) 25 ms and (b) 100 ms frame integration time using epifluorescence excitation as a function of time.

sources and random intensity fluctuations. Combined with image data, the poor spatial coherence can be identified, as the modes "walk" over a small region of interest of the area of excitation in the epifluorescence modality. As expected, multi-mode fibres are well documented for having poor spatial and temporal coherence [51].

2.5.4 Results - Region of Interest (Total Internal Reflection Fluorescence)

Following the epifluorescence excitation, the same experiment is conducted using total internal reflection fluorescence excitation from a laser diode. The uniformity of the output should be improved relative to the multi-mode fibre output to allow comparison with the epifluorescence excitation source regarding the uniformity and consistency of the excitation across the field of view.

Decay in fluorescent output can be attributed to either photobleaching of the fluorescent microsphere or to axial mechanical drift, which decreases the effective collection of photons. As the fluorescent microsphere moves out of focus (as with axial drift), photons are collected less effectively, leading to a reduction in the measured fluorescence at the camera. Using spatial information provided in the raw data, the decay is partially due to an axial drift in the sample. Fig. 2.8 shows similar findings statistically to the data presented in Fig. 2.7 with regards to a lower frame-to-frame noise with higher frame integration time and an increase in fluorescent detection. Axial drift has been observed to be higher in total internal reflection fluorescence experiments, likely due to optical heating from the significantly higher laser power at the source, despite most of the laser power passing through the prism; the losses are discussed further in 2.4.1.

2.5.5 Discussion

Frame integration time selection is essential for many reasons regarding imaging and selection. Longer frame integration times will average out short events (such as a sudden spike in detection or a sudden mechanical shift before returning to the previous state) across the entire frame integration time; they will also increase the number of photons collected per image, thereby increasing image signal-to-noise ratio. A short

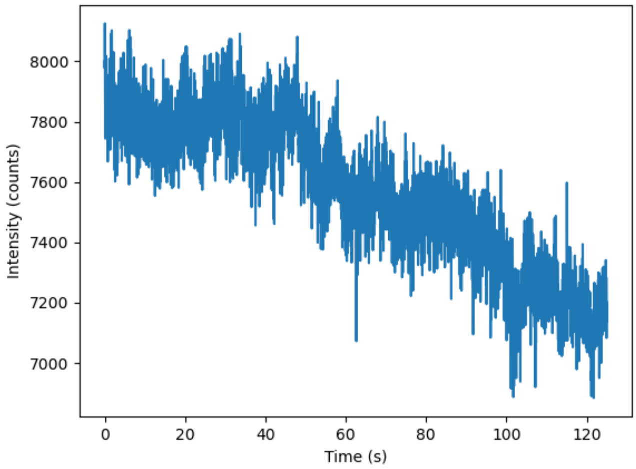

(a) 25 ms

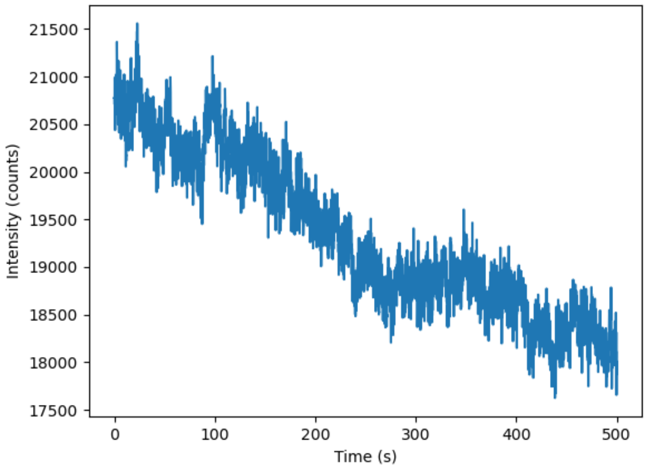

(b) 100 ms

Figure 2.8: Variation of the fluorescent output of a fluorescent microsphere in a region of interest 5x5 pixels in size for both (a) 25 ms and (b) 100 ms frame integration time using total internal reflection fluorescence excitation as a function of time.

event results in shorter frame integration times and a lower image signal-to-noise ratio because fewer photons are collected. However, the photon shot noise is likely to dominate the background noise from the camera, since the environment is thermally controlled and fixed pattern noise is exacerbated by higher camera gains that are not utilised here. This is demonstrated by comparing the graphs in Fig. 2.7.

Fig. 2.7 demonstrates the pattern of fluorescence evident with poor spatial uniformity of excitation sources with random fluctuations as the modes "walk" over a small region of interest of the area of excitation in epifluorescence modality. As expected, multi-mode fibres are well documented for having poor spatial coherence. By comparison, Fig. 2.8 shows a decrease in fluorescence that is indicative of defocusing caused by axial drift (confirmed by reviewing raw data), especially when the relationship for photobleaching is not linear. [52] The defocusing could be due to localised thermal heating by the laser used for total internal reflection fluorescence excitation because a larger excitation power is required to enter the prism to produce an evanescent field excitation with similar power densities at the sample to that of the epifluorescence mode, causing mechanical drift of the system.

Considering the effects of time averaging, extending the frame integration time to 100 ms can allow comparison of the noise frame-to-frame and its effects over a more extended acquisition period (8 minutes). Total internal reflection fluorescence remains dominated by axial drift, whereas epifluorescence shows a significant increase in fluorescent output over time; all measurements are taken from the same region of interest, which is thought to correspond to the same fluorescent microsphere considered. A magnitude variation can be attributed to a mode with more excitation power traversing the region of interest. Whilst axial drift may be present, this data does not indicate whether it is a contributing factor.

Otherwise, the collected data aligns with expectations for the camera acquisition boundaries at 25 ms. Total internal reflection fluorescence is dominated by shot noise because the region of interest is sampled to include only fluorescent areas, yielding 17 counts, or 6% of the peak intensity. At 100 ms, total internal reflection fluorescence exhibits shot noise of 29 counts, corresponding to 3% of the peak recorded intensity.

Epifluorescence is comparable. This is expected from a camera: as the acquisition time increases, more photons are collected, so the shot noise increases (17 counts vs 29), but the signal-to-noise ratio decreases (6% to 3%), improving the information recorded.

Overall, the data presented in this section, alongside the spatial information from images, provide a strong argument that the multi-mode fibre in the epifluorescence excitation is directly causing mode-mixing, producing a time-varying walking pattern. In contrast, the total internal reflection fluorescence excitation is a more stable source due to its coherent wavefront.

2.6 Conclusions

The optical design and characterisation of a multi-modal system capable of imaging structures up to 105 x 66 μm with an effective magnification of 94x and an effective pixel size at the sample of 55 nm. This microscope is comparable to those commonly found in biological laboratories. It can be assumed that if there is sufficient signal-to-noise to resolve biological images, then there is sufficient fluorescence for NV- sensing, assuming adequate excitation. It is also prudent that biological specimens are used, increasing the probability that future work will be able to provide the spatial information required.

The defining parameter on the success of this system for NV- sensing is the ability to image point sources (like fluorescent microspheres) and distinguish them from the background, which is achieved. The choice of an objective with a high numerical aperture ensured this, increasing the collection angle. It is also important to have a field of view large enough to image biological structures, as described further in Chapter 6.

For a fair comparison of modalities, using the same laser source would have been prudent. Therefore, no clear comparison can be made regarding differences in modalities in terms of noise characteristics, except for the rejection of out-of-focus light. Further, PSF measurements would have given insight into aberrations within the system. However, the system is limited at the time of measurement, with the z-axis control still under manual control.

Total internal reflection fluorescence is specifically chosen as a novel method of NV-centre imaging. The use of a small volume of excitation should improve the ability to select smaller clusters of nanodiamond, improving the homogeneity of the spectroscopic detection, since any nanodiamond outside this evanescent field should not be excited. A dual modality system is also novel, and specifically its use for simultaneous NV- centre imaging and biological imaging. To achieve this dual modality, capable of simultaneous excitation, two separate laser sources are required.

Chapter 3

Calibration of Nitrogen Vacancy Centre Sensing Using Widefield Imaging

Diamonds are both scientifically and culturally significant. Their use scientifically spans many fields from quantum computing and micro-electromechanical systems to thermodynamics and electrolysis. [53, 54, 55, 56] Sociologically, diamond is used as a gauge for research on gender equality and as a means of exploring the formation of worth. This speaks to the versatility and importance of diamonds, both in science and societally. [57, 58] This work focuses on its application as a biological sensor.

Diamond is a fluorescent allotrope of carbon that does not photobleach over time or under high-intensity excitation. It is also a brilliant tool for biological imaging due to its low cytotoxicity and sub-diffractional size (only nanodiamond), enabling high spatio-temporal resolution for biotracking and biosensing. Nanodiamonds have been used as markers for various super-resolution microscopy techniques, such as STORM, STED, and two-photon microscopy. [59], [60], [61] The Nitrogen Vacancy (NV-) centre in bulk diamond has been the subject of quantum measurements, including Rabi oscillations, relaxometry, and Zeeman splitting. [62], [63], [64] The ability to overlay samples on the bulk diamond also provides some benefit to sensing where samples are in close enough proximity to incite a change to the measurement scheme of the NV- centre because the NV- centre used for sensing should produce the identical spectra before and after sample preparation unless the sample is interacting with the NV- centre. [65]

Fluorescent Nanodiamond (FND), a diamond smaller than 1 micron, is of particular interest because it uses the same sensing schemes as bulk diamond; however, its small size allows targeting FND to structures of interest within biological samples. The process of targeting and binding to these structures is known as functionalisation. It increases the feasibility of live-cell imaging since the fluorescent marker moves with the structure of interest. [66] Sensing loses sensitivity due to the inhomogeneous broadening associated with the FND, whether continuous wave optically detected magnetic resonance (CWODMR) spectra or pulsed regime measurements, the loss of stability can often be counteracted by repeating sensing measurements to increase the sample size at the cost of temporal resolution. [67]

There are many proposed methods for measurement with an NV- centre, with the main differentiating factor typically being whether the optical excitation wavelength is pulsed or continuously incident on the sample. CWODMR is used to detect spin-state transitions because scanning over the possible microwave excitation frequencies (discussed in Section 1.3.4) allows the frequencies at which spin-state transitions occur to be identified. Using the CWODMR method, magnetometry and thermometry follow, as thermometry is based on the frequency shift at which the maximum fluorescent loss occurs, and magnetometry is determined by the Zeeman splitting associated with dips in fluorescence. Further, pulsed measurements, where the laser and/or the microwave excitation source can be pulsed, depending on the measurement scheme, facilitate the measurement of the chemical composition of the local environment, where pulsed measurements are the methods for relaxometry associated with the τ_1 decay, Hahn Echo, and Rabi oscillation detection.

To date, pulsed measurements have been used in a wide range of biological applications. Specifically, relaxometry has been used for Hemoglobin, cytochrome C and human spermatozoa. [68], [69], [70] CWODMR has been mainly used for magnetic field sensing and temperature sensing as a cellular probe, with alteration to the measurement scheme, 4-point ODMR is developed as a technique for faster sensing as discussed in

Section 1.3.5, noise-reduced thermometry and applied on C. elegans to show the temperature differential between gonad and head with heat applied. [6] Using 4-point measurements, the data acquired for an example scan drops from 65 frequency steps (2.800-2.930 GHz with 2 MHz steps) to 4 frequency steps for every temperature point, decreasing the computing required post-imaging and increasing the temporal resolution of temperature sensing. However, these 4 points are typically repeated to increase the sample size, so the reduction is not a direct 65-to-4 ratio.

Since there is an apparent need to use FND in biological measurements, the system proposed in this work is designed for wide-field implementation of NV- sensing in CWODMR using FND as a cellular probe. Determining the characteristics of NV-sensing across different imaging modalities and the long-term viability of the system for biological imaging is completed to inform subsequent biological studies.

3.1 Imaging Scheme

All data presented in this chapter is acquired using the microscope described in Section 2.2. The resonant or scanning microwave frequencies are alternated with the off-resonant or reference microwave frequency frame-by-frame, where τ_a is the length of time the microwaves are on, τ_s is a start delay, and τ_e is a stop delay that can be applied to the camera to allow time for frame data to be transferred from the camera to the computer. Reference frames are acquired to eliminate the effects of sample drift caused by sample heating when exposed to different microwave excitations, enabling continued acquisition, and to meet the requirement for normalisation post-imaging to extract the CWODMR spectra. Microwaves are used at an off-resonant frequency because, in their absence, the system experiences heating, leading to mechanical sample drift due to rapid heating and cooling cycles in the reference frame. Images are acquired with continuous 532 nm (total internal reflection fluorescence) or 520 nm (epifluorescence) excitation. Fig. 3.1 (a) shows that the camera frame integration time (τ_a - τ_s - τ_e, total microwave excitation pulse minus the start wait minus the end wait) is set. The reference frequency is 2.500 GHz, and the power is 0 dBm before the amplifier, measured with the USG USB microwave generator. The scanning frequencies vary but are typically 2.800 - 2.9300 GHz with 5 MHz steps and a power of 0 dBm unless otherwise stated, generated via the AIM-TTi TGR6000 Microwave Generator.

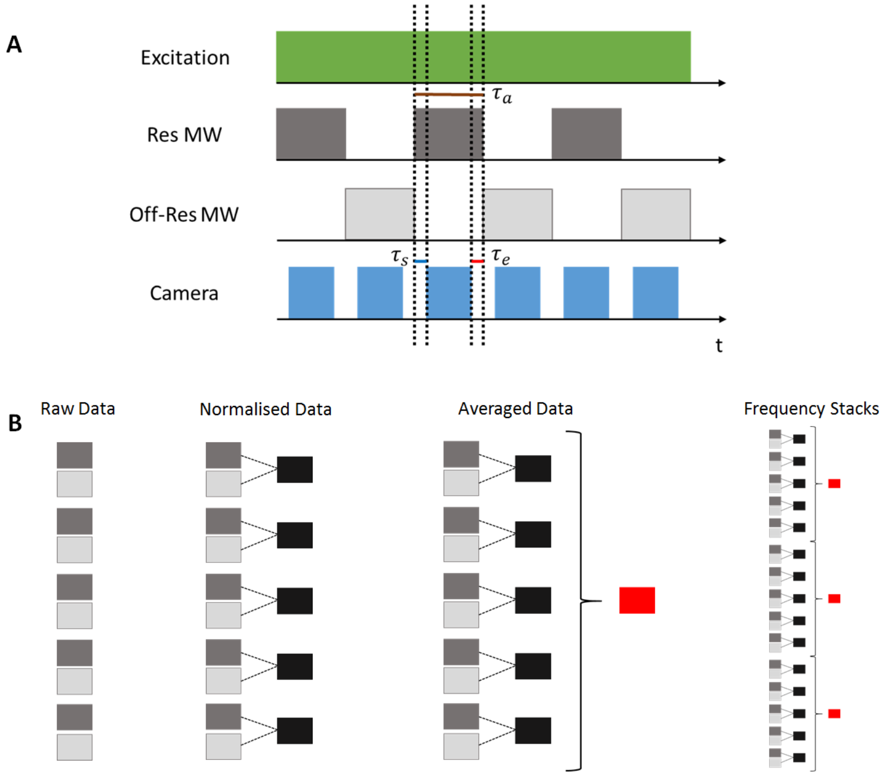

Figure 3.1: A) Scheme showing the relationship between microwave, camera and excitation for CWODMR using referencing for the microwaves. B) Image processing pipeline from raw data (grey) to normalisation (black) and the final frequency after averaging the normalised images (red) before continuous measurement has red as the final image for varying scanning frequencies.

3.2 Sample Holder Design for Multi-Modal Imaging

Sample preparation for NV- sensing includes FND mounting, a suitable excitation pathway (in the case of total internal reflection fluorescence), and appropriate microwave delivery. The method for microwave excitation is copper wire delivery; the copper wire is 50 microns in diameter and connected, using silver paint, to a waveguide on a printed circuit board that allows the sample holder to be connected to the microwave generation and switching hardware. The copper wire method is chosen because of previous studies within the group, as it offered scope for multi-sample imaging (e.g., diamond and biological specimens) and is not focused exclusively on NV- sensing. [1] Copper microwave delivery allowed greater flexibility in sample preparation, as the sample only had to be adhered between coverslips, and the ease of mounting made it a quick option with minimal optimisation.

Two mounting systems are required, dependent on the imaging scheme being employed, as portrayed in Fig. 3.2 for the FND, such that the FND could be mounted to a prism for total internal reflection fluorescence and a microscope slide equivalent for epifluorescence. The system designed for epifluorescence excitation only offers greater stability; the sample is secured to the waveguide, which limits its physical movement. Further, the implementation of microwaves in this scheme is more robust as the copper wire runs parallel to the rigid waveguide and coverslips. The epifluorescence sample-only system is ideal for initial stability measurements, as it limits the influence of measurement factors and uses a sample preparation method already well-characterised within the group [1]. However, there is no feasible way within the scope of this work to maintain this rigidity and stability whilst enabling prism-based total internal reflection fluorescence excitation.

The total internal reflection fluorescence is custom-designed; a prism holder is 3D-printed and mounted to the stage, as shown in Fig. 3.2. A small through-hole LED is under the prism and controlled via Raspberry Pi to facilitate transmission microscopy for sample viewing. For microwave delivery, a PCB waveguide is split in two and adhered to the prism mount. The copper wire is passed through the sample, and silver paint is used to adhere it to the waveguide. The prism, holder, and PCB board showed no deterioration over 2 years, despite many sample changes.

To ensure even mounting, two thin strips of packing tape are placed parallel to the copper wire at the edge of the coverslip, out of view of the microscope, to prevent uneven mounting of the top coverslip. The diamond and copper wire are then mounted in de-ionised water and sealed with commercially available nail polish to prolong the samples longevity.

FND are distributed on a coverslip using a nebuliser to achieve thin, dispersed coverage and reduce clumped diamonds. FND are suspended in de-ionised water (1:1000)

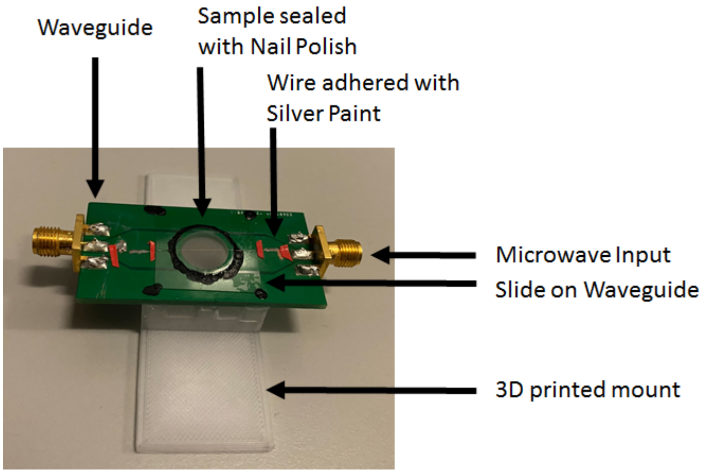

(a) Epifluorescence Sample only

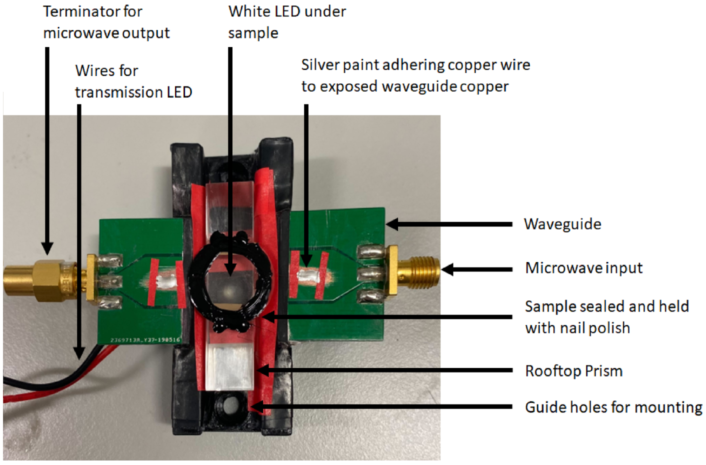

(b) Total internal reflection fluorescence and epifluorescence sample

Figure 3.2: Images showing the experimental method for sample preparation of (a) epifluorescence samples and (b) samples that can be used in total internal reflection fluorescence only or in conjunction with epifluorescence excitation.

and loaded into the nebuliser chamber; after initialisation and the required warming time to produce vapour (approximately 10s), the coverslip is held in the vapour cloud for 1 min. After removal from the FND vapour, a sample can be prepared with copper wire and de-ionised water as a mountant, as previously discussed in this section.

3.3 Data Processing

Images acquired are interlaced with reference and scanning frequencies, as shown in Fig. 3.1 (b). The data is normalised by dividing the reference by the scanning data; those points are averaged over the number of frequency repeats. Due to lateral sample drift corresponding to the stage or sample present over the acquisition time, drift is corrected using NanoJ drift correction in FIJI before processing. [11], [28]. The software analyses the position frame-to-frame after acquisition. It corrects it by shifting the images along the x- and y-axes so that structures appear at the same (x, y) position in both images. Typical drift varies between 2 and 15 pixels (110-825 nm) over the course of an entire CWODMR scan.

Using FIJI, the data is opened, drift corrected and is now ready for processing. Data is deinterleaved, an image calculator is used to divide the images for normalisation, and a group Z project is used to average image frequency repeats before plotting the Z-axis profile. Noise is calculated from the total photons collected, assuming shot noise at each normalised frequency point, since the region of interest includes only fluorescent areas, and is plotted as error bars on the fit. The resulting plot region of interest can be selected and evaluated across the field of view.

After drift correction, a region of interest can be selected, and the Z-axis profile can be saved as a .txt file for processing with the custom Python code to enable more in-depth analysis. Averaged fluorescent intensities are multiplied by the number of pixels in the region of interest, so that the total number of photons detected is analysed rather than the average. The resulting data is then plotted as normalised intensity against microwave frequency. Two scripts are used: one performs a double-Lorentzian fit to the data, and the other is used for the four-point thermometry measurements, which calculate the optimal frequencies for the analysis.

3.4 Improving Image Contrast for Region of Interest Selection

3.4.1 Sample Preparation and Acquisition Scheme

A sample of 90 nm FND is drop cast onto a 22 mm square coverslip and allowed to evaporate. The mounting medium is de-ionised water. A 50 micron copper wire is placed, then sealed with an 18 mm round coverslip and nail polish, and mounted using the method for total internal reflection fluorescence imaging as presented in Section 3.2. The acquisition scheme used a 250 ms frame integration time with a camera gain of 0 dB, and 1000 repeats of normalisation (a frame each for off-resonant and scanning microwave frequencies) over the frequency range 2.600 GHz to 2.870 GHz. Reference and scanning acquisition is used to improve SRRF outputs, since scanning at a resonant frequency and reference at an off-resonant frequency would increase fluorescent variability frame-to-frame. Separate CWODMR scans are taken for processing of the NV- response from 2.800 GHz to 2.9300 GHz with 5 MHz steps and 5 repeats per frequency.

3.4.2 Results - Region of Interest Selection

The choice of region of interest used to measure the change in fluorescence is crucial because the efficiency of the optical response of the NV- centre can vary from FND to FND within the field of view; the characterisation of this variation allows the best selection of region of interest to produce CWODMR with the most significant dip depth and highest signal-to-noise, reducing the apparent ODMR noise. Characterisation determines the best method for selecting the optically active region of interest for CWODMR and the optimal conditions for region-of-interest selection to increase signal-to-noise whilst increasing the resulting dip depth. To demonstrate the importance of the region of interest selection, the fluorescent output of three different regions of interest (Fig. 3.3) are plotted against the laser excitation in Fig. 3.4. When selecting a region of interest, we separate it into three groups: single crystal, cluster, and clump.

A single crystal is typically the dimmest emitter in the field of view. These are

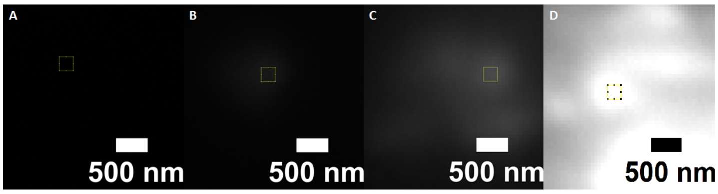

Figure 3.3: Image of various emitters across the field of view where a) is a background, b) single crystal (dimmest emitter), c) cluster (resolvable emitters nearby) and d) clump (unresolvable emitters nearby) of FND.

separated from other FNDs and, because they are thought to be single crystals, exhibit a uniform crystalline orientation, typically resulting in the smallest bandwidth in the CWODMR spectra. A cluster is a mid-ground where separate, resolvable emitters are in proximity to each other. The captured fluorescence is an average of many different NV-centre optical responses, which can vary depending on orientation, intrinsic crystalline properties, or responsivity, broadening any Lorentzian fit. The clump is a large mass of FND in which the emitters cannot be distinguished; their Lorentzian fits are often very broad and typically cause camera saturation in imaging criteria where single crystals are resolvable. A Gaussian fit would be a better model for fitting in cases like this.

The graph in Fig. 3.4 shows that, even with increased laser power, there is a negligible change in the background under total internal reflection fluorescence excitation. There is little fluorescent output from a single FND at lower excitation powers; in both the cluster and the clump, increasing excitation power increases the fluorescent output until camera saturation. For low laser excitation around 5 mW, the fluorescent output is below 500 counts on detection for all region-of-interest types; this is far from the camera's full dynamic range. Single FND does not approach 500 counts despite the total incident laser power, although it does increase above the background, which is indistinguishable from it. The background does not increase with total incident laser power, indicating a lack of excitation breakthrough (laser emission not completely filtered from detection, which increases the background of a fluorescent image) within the imaging system.

For a cluster, the fluorescent intensity is doubled by 25 mW and tripled by 45 mW; saturation is achieved at 45 mW for clump samples. Cluster region of interest closely

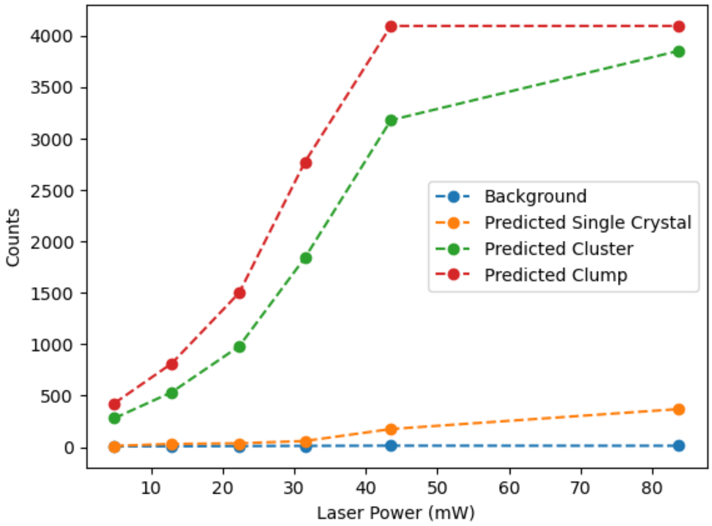

Figure 3.4: Laser power (measured at laser output) plotted against the fluorescent output of the emitters described in Fig. 3.3. The saturation of the presented (maximum value) corresponds to the camera's detection range. Populations are labelled as predicted because there is no way to verify the claim; predictions are based on the expected behaviour (single crystals having lower fluorescent output than clusters or clumps) of emitters within the field of view.

follows at 3750 counts at 85 mW. The benefit of cluster and clump region of interest selection is that the laser powers required for excitation are much lower than those for a single FND. However, the randomised orientation of the crystalline structures causes power broadening, as described in [71], since the fluorescence collected is a mixture of different NV- centre responses. For quantum spectroscopy of FND, a single crystal is preferable, as CWODMR is more sensitive to environmental changes due to its narrower bandwidth and higher contrast.

3.4.3 Results - Contrast Limited Adaptive Histogram Equalization

Contrast Limited Adaptive Histogram Equalization (CLAHE) is a plugin available in FIJI that scales image contrast to improve the visual identification of structures. This is useful for region of interest selection; in raw images (Fig. 3.5(a)), it is challenging to distinguish FND from the background because, in the acquisition scheme, a low frame integration time and gain are statistically beneficial as low exposure time increases the time sampling and low gain reduces the noise characteristics by reducing the effects of fixed pattern noise and amplifier noise. By applying CLAHE to the images, the dimmer FNDs, which are more likely to be single FNDs, provide better ODMR parameters and are more easily visible in the field of view (Fig. 3.6). This is particularly notable in the centre and upper right of the field of view. Notably, CLAHE only reregisters pixel values after saving the data; if the data is not saved, the data presented will have a LUT applied, with no change to the pixel values. By not saving first, a region of interest can be identified and the raw values extracted from the raw data, whilst still having the benefit of improved visualisation.

When CWODMR spectra are obtained using a region of interest selected from a structure that is not visible in raw images but is visible in post-CLAHE images, the contrast is 16%. It is difficult to determine the quality of the bandwidth determined by a smaller bandwidth always being preferable as it is closer to the classical Lorentzian response expected in CWODMR [72] and splitting of the double Lorentzian as the sampling is not sufficient to define these well, if a smaller step size (2 MHz instead of 5 MHz) had been used the sampling may have been sufficient for this. The fitting parameters in Fig. 3.6 are adjusted by altering the full width half maximum that the script expects for each dip. However, the fit could not recognise the 1% increase in fluorescence at the minima of the curve.

The CWODMR contrast in the CLAHE sample is huge, 8 times the magnitude of the noise, taken from Fig. 3.6. The noise is 2% at the outer edges of the frequency scan. The CWODMR spectra exhibit a notably deep dip and confirm the benefit of visually improving image contrast for region-of-interest selection. CLAHE avoids re-registering pixel values until saving, so as long as data is collected before then, there is no change to the data. To ensure this, the same region of interest is evaluated in a raw dataset without CLAHE, yielding the same plot.

3.4.4 Results - Super-Resolution Radial Fluctuations

Another option for spatial enhancement is Super-resolution radial fluctuations (SRRF), another NanoJ plugin available via FIJI [11], [28]. SRRF enhances the spatial localisation of sub-diffraction emitters.

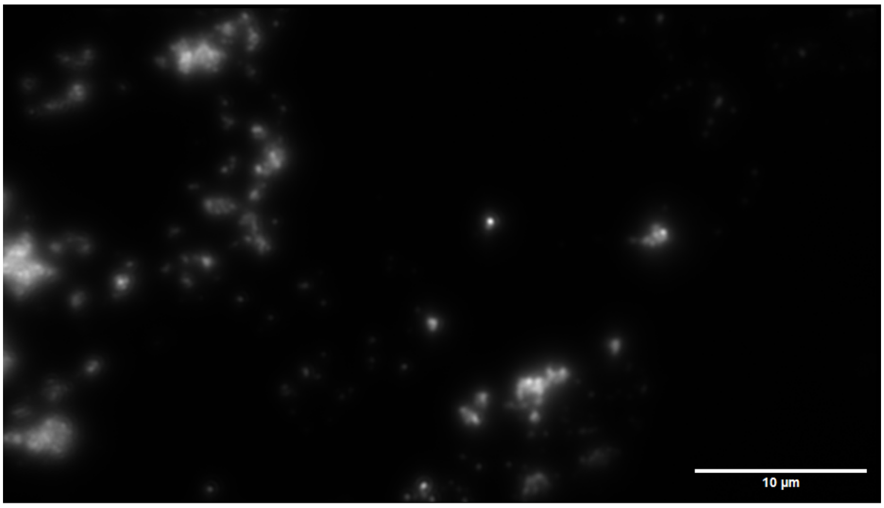

(a) Raw image with no processing

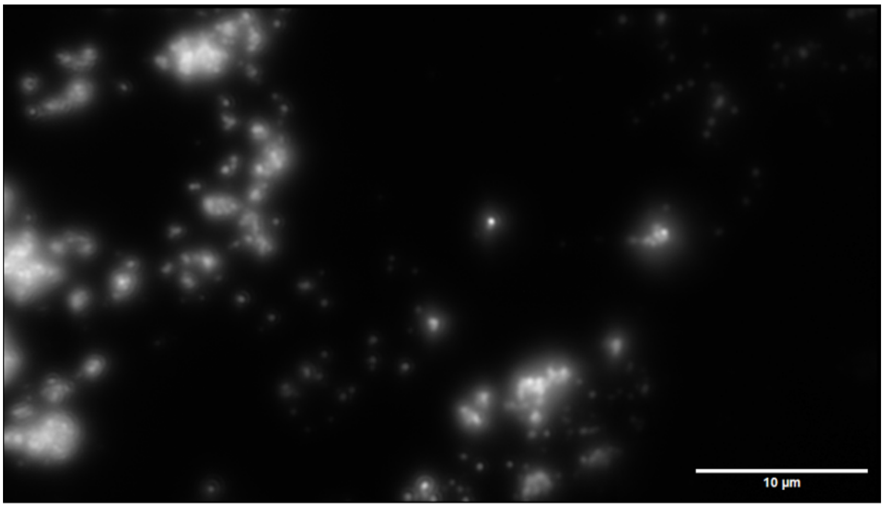

(b) Image after CLAHE

Figure 3.5: Image comparison of the a) raw image and b) a frame after CLAHE balance adjustments.

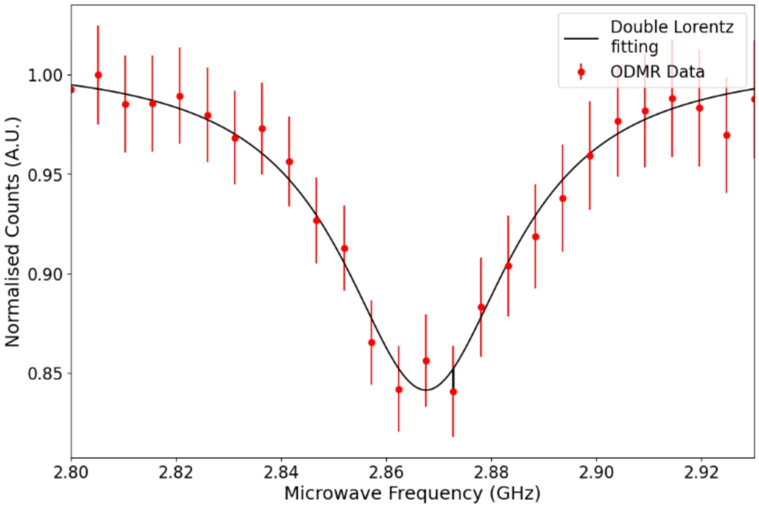

Figure 3.6: CWODMR spectra collected from a 5x5 region of interest after applying CLAHE to the dataset and selecting a region of interest that isn't previously visible in the raw data. The scan range is 2.800-2.930GHz with a step size of 5MHz, 5 repeats per frequency, 250ms acquisition time, and no camera gain (0dBm)

The motivation for SRRF combined with NV- sensing is two-fold: to improve the spatial accuracy of an emitter within the field of view and to determine the optically active NV- centres. To determine the features corresponding to ODMR active FND, 1000 off-/on-resonant frequency repeats are normalised with respect to the signal channel rather than with respect to the reference. As such, the expected ODMR fluorescence dip will now be seen as a peak, and the SRRF algorithm can process it accordingly; this is peak-normalised and presented in Fig. 3.7(a). The opposite is also presented, where the normalisation is completed with respect to the reference; this is dip-normalised and is presented in Fig. 3.7(b), and SRRF is taken from these resulting images.

When images are divided positively, the resulting image after SRRF processing produces small, bright objects above the background, where the existing emitter is visible in the raw data before normalisation and also new points that are not distinguishable (see raw image 3.5). Negative division results in a map showing dark circular structures surrounded by high background levels, and these voids are now the optically active NV- centres with CWODMR responsivity. These voids are likely artefacts, constructed from the variation in fluorescence detected (black void) to entirely background/camera noise (orange).

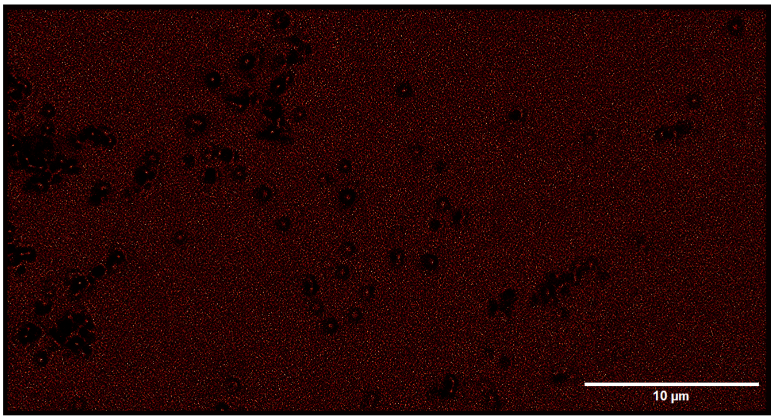

(a) Resonant Frequency divided by the reference frequency (peak-normalised)

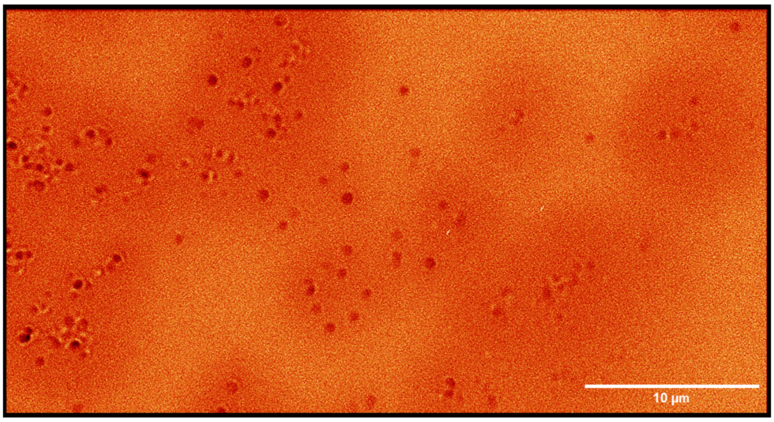

(b) Reference frequency divided by the resonant frequency (dip-normalised)

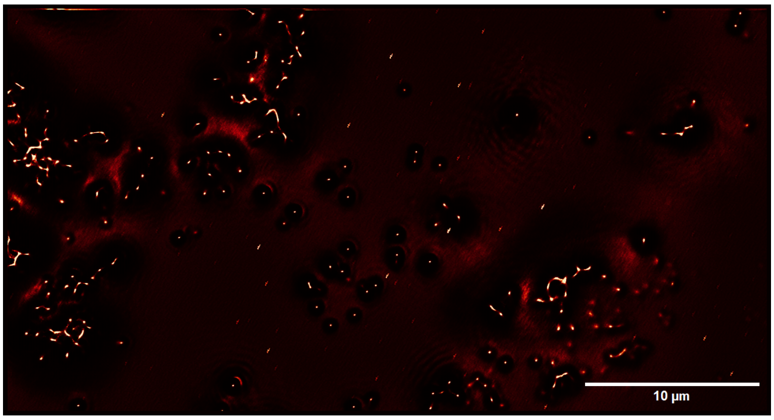

(c) No normalisation

Figure 3.7: SRRF images with 2000 images in pairs of resonant (2.75 GHz) and off-resonant (2.500 GHz) microwave excitation.

Comparing the resulting images shows comparable spatial information regarding (x,y) position, with no benefit to one processing method over the other. Further examination of the field of view in the data processing without normalisation in Fig. 3.7(c) shows numerous extra features, for example, those marked with dashed rectangles, in the SRRF processed image, indicating that not every emitter is optically active.

By taking CWODMR spectra from an area that is optically active in Fig. 3.7(a) and translating the (x,y) position to raw CWODMR scan data - since it provides a higher spatial resolution of the location of an emitter compared to Fig. 3.7(b) - we can evaluate the quality of the spectra in Fig. 3.8. The spectra acquired have a CWODMR contrast of 10% and noise around 2%; splitting of the spin states is evident, with the spin state on the right weighted. The bandwidth of the curve is around 20 MHz, and the curve width is overall spread over a large area due to the inhomogeneous broadening.

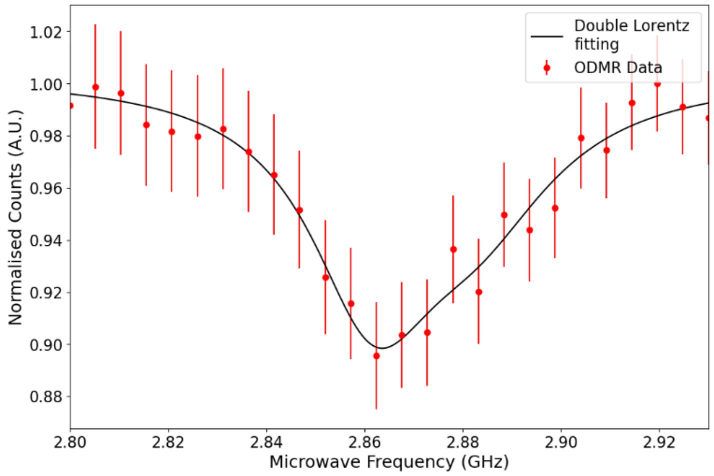

Figure 3.8: CWODMR spectra extracted from region of interest determined by Fig. 3.7 to ensure structure is optically active.

Because the SRRF process removes any fluorescent fluctuations, frame-to-frame testing of emitters is possible. CWODMR spectra involve identifying the emitter of interest in Fig. 3.7 and locating the same point in the raw data. The pixel count increases in the image after SRRF compared to the raw data, making region-of-interest identification even more difficult in the raw data.

3.4.5 Discussion

Region of interest selection is crucial for performing the NV- spectroscopy measurement. Section 3.4.2 demonstrates the importance of selecting regions of interest that are most likely to be single crystals for an improved spectral resolution and to facilitate measurement free from FND interaction leading to inhomogeneous broadening. Enhanced dip depth is also beneficial for magnetic and thermometry sensing because it provides better tolerance to fluctuations and increases the thermometry range, as discussed in Section 1.5.2.

Enhancing the visibility of emitters within the field of view makes it easier for the user to select the dimmest fluorescent features that correspond to a single ND. The CLAHE plugin works on a single image. However, there is code explicitly written to process stacks with CLAHE [73]. Using this code, the entire stack is enhanced whilst maintaining the relative fluorescent output frame-to-frame, so the stack only needs to be processed once. CWODMR spectra can be extracted from the stack without additional steps, since the pixel intensities are not overwritten, unlike after SRRF processing, which can only be used to reference a point back to the initial raw data.

Whilst SRRF provides more precise spatial information about the optically active emitters, this is balanced by the need for a large number of frames to accurately improve the spatial precision of the point emitter. Acquiring that data takes a long time, which may be impractical for samples with a time limit (e.g., live biological or fluorophore-labelled samples). Interestingly, SRRF indicates that not all emitters in the sample are optically responsive to microwave excitation for CWODMR, since the structures are likely to exhibit more artefacts and less fluorescent variability. Instead, this is explainable by the contrast provided by the NV- the centre of that emitter being dominated by the noise. This can occur when the crystalline alignment is antiparallel to the detector, resulting in the lowest spectral contrast.

SRRF improves spatial accuracy in the detection of optically active emitters. CLAHE enables the selection of regions of interest that would otherwise be invisible without contrast enhancement. It can simultaneously evaluate CWODMR spectra without reference to another dataset, enabling the selection of the entire region of interest.

3.5 Characterisation of Optically Detected Magnetic Resonance

3.5.1 Sample Preparation and Acquisition Scheme

Samples of 90 nm FND are made using the same method presented in Section 3.2 for total internal reflection fluorescence mounting. 90 nm FND is chosen as a compromise between the larger frame integration times required for smaller FND due to fewer NV centres per crystal and the measurement's sensitivity, as with a greater number of NV centres per FND. It is known that sensitivity to environmental changes is lost due to the greater inhomogeneous broadening in common (not custom, high-end) FND. [40] The excitation wavelength is 520 nm at 40 mW at output in epifluorescence. Images are collected with a frame integration time of 200 ms and a camera gain of 10 dB. CWODMR spectra are collected with 2.800-2.930 GHz scan parameters, 2 MHz step size, and 10 point repeats per frequency. For total internal reflection fluorescence, the same measurement parameters are observed at a laser power of 210 mW.

For single-source dual excitation, the sample is excited at 520 nm (40 mW) and 450 nm (19 mW) in epifluorescence, with both laser wavelengths provided simultaneously by the epifluorescence laser. Images are collected with a frame integration time of 200 ms and a camera gain of 10 dB. CWODMR spectra are collected with 2.800-2.930 GHz scan parameters, 2 MHz step size, and 10 point repeats per frequency.

For dual source excitation, the sample is excited using 532 nm at 210 mW (22 mW at the sample plane) in total internal reflection fluorescence and 450 nm at 35 mA (10 mW at the source); the 532 nm excitation is from the total internal reflection fluorescence laser and the 450 nm is from the epifluorescence laser, both incident on the sample at the same time. Images are collected with a frame integration time of 200 ms and a camera gain of 10 dB. CWODMR spectra are collected with 2.800-2.930 GHz scan parameters, 2 MHz step size, and 10 point repeats per frequency.

3.5.2 Results - Microwave Characterisation

Microwave delivery is an essential method in this spectroscopic scheme. With two separate generators, it is important to evaluate the microwave delivery through a sample. By connecting an RF detector, we can observe the generator's output.

By looking at the signal before and after the sample, we can determine the losses through the sample, the actual output relative to the generator output, and the output's full-width half-maximum. Using Fig. 3.9, we can see the output (a) before and (b) after the sample using the scanning frequency generator. The microwave peak frequency is 2.875 GHz for each, and the loss between the generator and the sample is 1.3 dBm, as the generator output is 0 dBm. Losses through the sample are 19 dBm, which is substantial. They are either attributed to the silver paint connection to the waveguide not being impedance-matched or to absorption in the sample, as excitation of the sample occurs simultaneously with imaging.

Similarly, it is also important to characterise the reference frequency output as shown in Fig. 3.10. Before the sample, 0.5 dBm power is applied at 2.875 GHz, which is much higher than the scanning frequency generator and could cause drift due to heating differentials caused by the power differential. This higher output power is also concerning because the generator's output should have been 0 dBm, yet the TRG6000 measurement shows a total differential of 1.8 dBm, suggesting the actual output of the USB microwave generator is 1.8 dBm when set to 0 dBm. The broadening is also much more considerable at 1 MHz; in the scanning frequency, this would be a block in the imaging scheme. However, because this frequency is held off the excitation frequencies at 2.500 GHz, and the chosen frequency only needs to be non-exciting for NV centres to be suitable for reference, as long as it is constant, it is acceptable for NV spectroscopy. The discrepancy between the input microwave power and the measured value is within the manufacturer's guidelines for the spectrum analyser, at ±1 dB.

3.5.3 Results - Epifluorescence

In reference to Section 3.4.2, which discusses the region of interest selection criteria, this section looks at the effects of using region of interest selection of single FND and

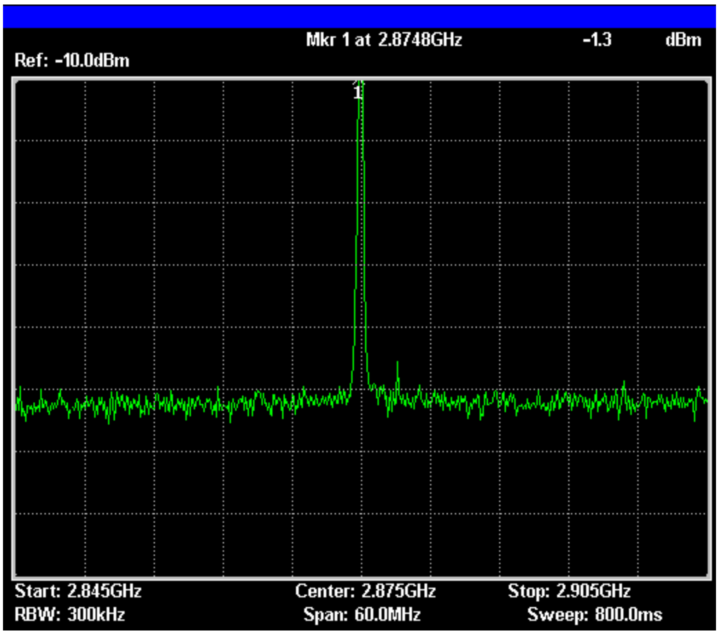

(a) Before Sample

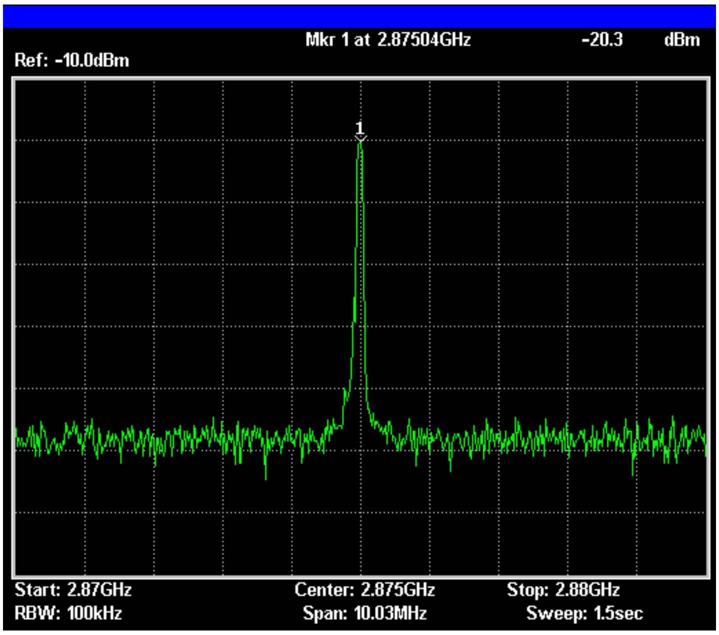

(b) After Sample

Figure 3.9: Microwave output of TRG6000 microwave generator recording taken from RF oscilloscope before (full scan 60 MHz) and after (full scan 10 MHz) the sample (total internal reflection fluorescence mounting) to demonstrate the loss of power throughout the sample and the narrow bandwidth of excited frequencies at 2.875 GHz output.

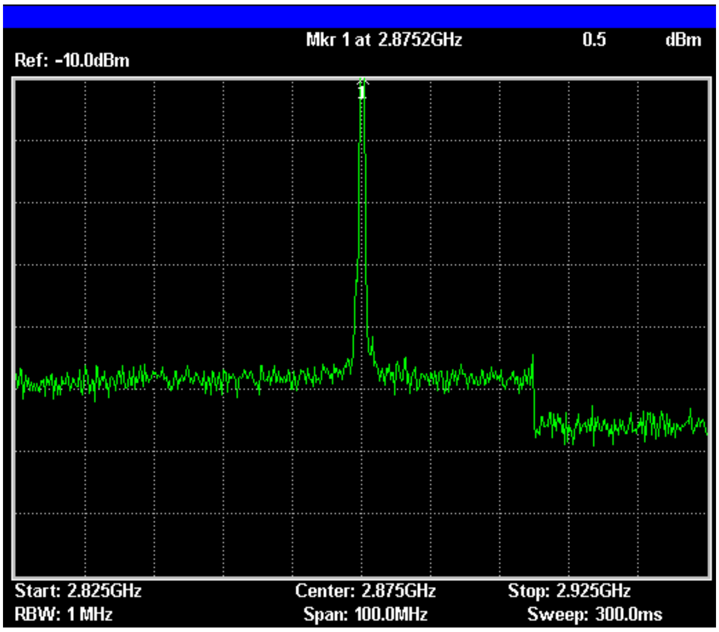

Figure 3.10: Microwave output of USG USB microwave generator recording taken from RF oscilloscope before sampling for comparison to the TRG6000 microwave generator, as the peak power is mismatched compared to the expected output power (full scan is 100 MHz).

cluster emitters. By comparing the graphs produced in Fig. 3.11, we can see that both graphs have similar bandwidth (4 MHz and 5 MHz, respectively) (single is marginally smaller). However, the reason for this varies by sampling. For the single crystal, it is because two Lorentzian curves have been fitted with different weighting to the $|-1\rangle$ and $|+1\rangle$ spin states, clearly seen at 12% on the right-hand side of the curve. In the cluster sample, it is because of the broadening of multiple NV- centres nearby and the inhomogeneous broadening due to strain on individual NV- centres.

3.5.4 Results - Total Internal Reflection Fluorescence

The difference between the broadening is evident in Fig. 3.12. The broadening doubles between a single crystal and the multiple FND regions of interest despite being the same sample size. Of note, the fitting quality is poorer in the multiple FND selection since the points calculated vary greatly from frequency to frequency; the fit is much better even where noise is calculated from the extremes of the graph.

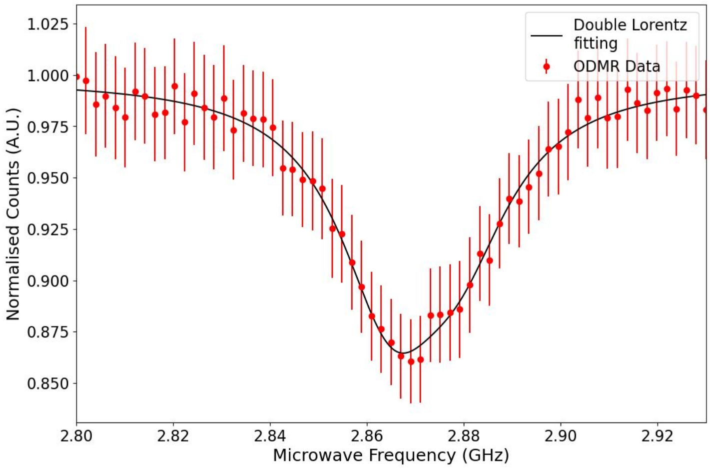

(a) Single Crystal

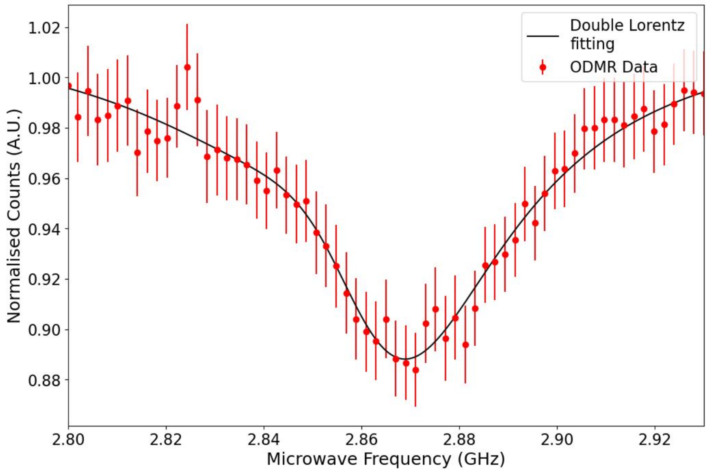

(b) Multiple FND

Figure 3.11: CWODMR between 2.8GHz and 2.930GHz with 2MHz steps, where region of interest selection varies from a) suspected single crystal and b) a cluster of FND in epifluorescence.

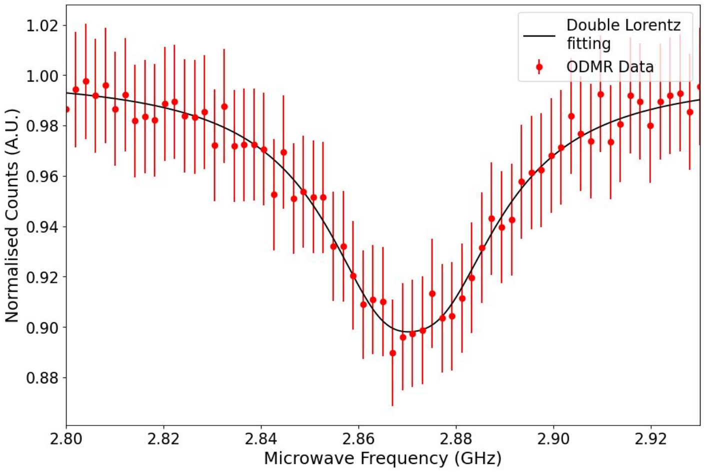

(a) Single Crystal

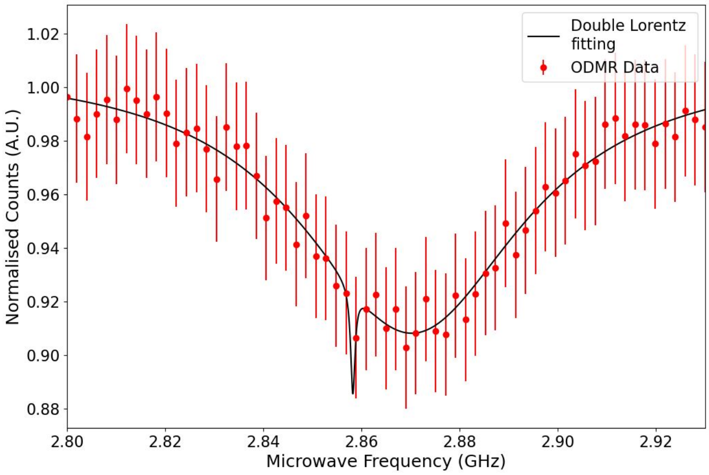

(b) Multiple FND

Figure 3.12: CWODMR between 2.8GHz and 2.930GHz with 2MHz steps, where region of interest selection varies from a) suspected single crystal and b) a cluster of FND in total internal reflection fluorescence.

There is also a difference in contrast: the single FND shows 11% contrast, while the multiple FND shows 9%. Whilst a difference of 2% may seem small, this is beneficial for magnetometry and thermometry, where the larger the contrast, the more accurate the measurement becomes.

3.5.5 Results - Dual Excitation

Dual excitation becomes important later in this work when applied to biological specimens, so that excitation of FND can co-occur with excitation of fluorescent labelling of structures; the effects of dual excitation on the FND are essential for troubleshooting any unexpected broadening or noise.

Excitation using exclusively epifluorescence produces a curve with unequal weighting between $|-1\rangle$ and $|+1\rangle$ spin states, the cause of which is unclear but is consistently observed throughout measurements. Fig. 3.13 clearly shows similarities in CWODMR between dual excitation using the epifluorescence exclusively and the total internal reflection fluorescence and epifluorescence combination: the minima are similar at 2.862/2.878 GHz and 2.864/2.879 GHz, and the contrast is similar at 9%. There is one additional component: the fit accuracy, which depends on the measurement noise. From Section 2.5.3, we discuss at length the effects of the laser noise in epifluorescence; the noise and poor fit can be attributed to the laser noise present in excitation, since an increase in the noise would increase the variation of the detected intensity.

It is essential to ensure that 450 nm does not excite the NV- centre during measurement and does not contribute to the CWODMR spectra. Fig. 3.14 uses 450 nm epifluorescence with no green excitation to produce spectra. The plot shows consistent detection not exceeding 2% contrast, which, from previous plots, has been equal to the noise, indicating no contribution from the 450 nm leads to a NV- response.

3.5.6 Discussion

Characterisation of CWODMR spectra across all excitation configurations provided an overview of the system's capabilities and restrictions. Separately, epifluorescence and total internal reflection fluorescence demonstrated that selecting a single-crystal

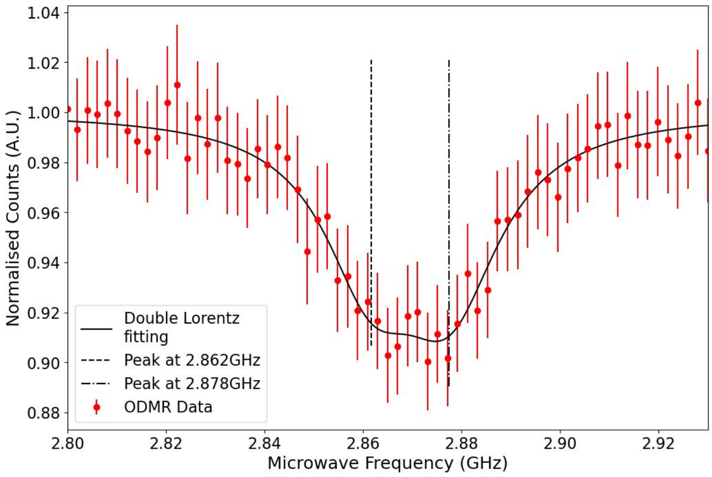

(a) Epifluorescence dual excitation only

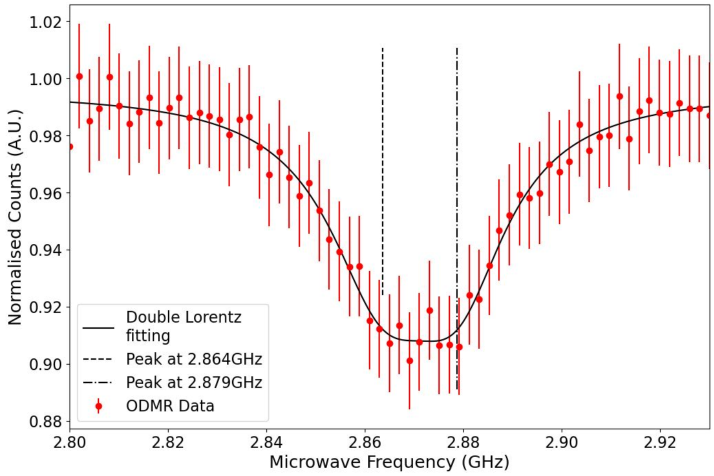

(b) Total internal reflection fluorescence and epifluorescence dual excitation

Figure 3.13: CWODMR between 2.8GHz and 2.930GHz with 2MHz steps, where excitation is completed using a) epifluorescence only exciting 450 nm and 520 nm and b) total internal reflection fluorescence exciting 532 nm and epifluorescence exciting 450 nm in the same suspected single crystal.

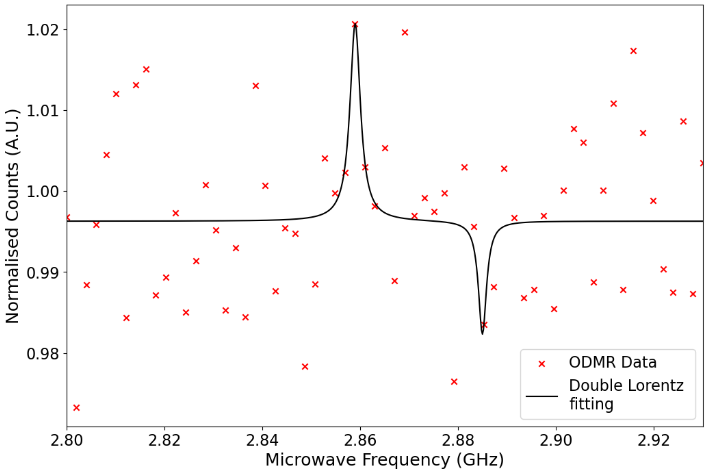

Figure 3.14: CWODMR between 2.8GHz and 2.930GHz with 2MHz steps, region of interest selection from a suspected single crystal in epifluorescence with only 450nm excitation.

region of interest for CWODMR improves contrast, bandwidth, and fit accuracy, while reducing noise. Fig. 3.11 and Fig. 3.12 show that selection in epifluorescence and total internal reflection fluorescence can affect the CWODMR contrast by 2% change and 1% change, respectively, which could be due to the difference in excitation wavelengths, where 532 nm is the peak excitation, and 520 nm is slightly off-peak, which could lead to a lower fluorescent output. [74] As previously discussed, this improves accuracy for magnetometry and thermometry by increasing the probability that the spectral contrast increases the gradient of the dip slope, which increases the likelihood of observable change from an external factor and increases the range over which measurements can be completed.

Surprisingly, the contrast of epifluorescence is larger than that of total internal reflection fluorescence. It would be expected that, because of the background reduction in total internal reflection fluorescence, an improved signal-to-noise ratio should improve spectral contrast. However, the effective optical power at the sample of epifluorescence is larger than the total internal reflection fluorescence excitation.

Furthermore, dual excitation does not influence the CWODMR total internal reflection fluorescence excited spectra. In Fig. 3.13, dual excitation utilising only the epifluorescence RGB laser produces a contrast of approximately 10% with 2% noise;

this is much lower than only 520 nm excitation. However, it can be argued that increased noise from mode-mixing in the fibre delivery leads to greater frame-to-frame instability, distorting the average fluorescent signal in a small region of interest.

Finally, the spectral contrast of 10%+ is comparable to that of systems using bulk diamond, EMCCD [75], and single-photon cards, often outperforming other systems described in the literature. [76] The compensation for this is high microwave powers (0 dBm) and high laser excitation compared to confocal systems, where 1 mW is sufficient [72]. However, this is likely to be a much higher power density, since confocal utilises a diffraction-limited spot. Epifluorescence has a power density of 175 $\mathrm{mW/mm^2}$ with input optical power of 40 mW, compared to 2 $\mathrm{kW/mm^2}$ in confocal microscopy using an input optical power of 1 mW.

3.6 Magnetometry

3.6.1 Sample Preparation and Acquisition Scheme

Samples are prepared using the method described in 3.2 for an epifluorescence-exclusive sample using 90 nm FND in water mounting. Excitation is completed using 115mA (40 mW) epifluorescence excitation; the acquisition is completed using 800 ms frame integration time, 10 dB camera gain and 10 repeats per frequency for a 2.800-2.930 GHz scan with 5MHz steps. A single neodymium magnet is placed 10 mm below the sample, and magnetometry measurements are performed with 20 repeats per frequency.

Another sample is prepared similarly with the inclusion of Iron(III)Oxide nanoparticles donated by Dr Liam Rooney, prepared via methods detailed in literature [77]. A slurry of Fe(III)O and 90 nm FND is suspended and dropcast onto a coverslip and mounted in 10% agarose because the magnetoparticles are present within the biological specimen when doing NV- measurement in Section 6.2. Samples are excited using 115mA (40 mW) epifluorescence excitation; the acquisition is completed using 800 ms frame integration time, 10 dB camera gain and 10 repeats per frequency for a 2.800-2.930 GHz scan with 5MHz steps. A single neodymium magnet is placed 10 mm under the sample, and a scan is completed with 10 repeats per frequency for magnetometry measurements. A second neodymium magnet is added to the same position as the initial magnet, and the scan range is extended to 2.75-2.95 GHz with 5 MHz steps to include both dips in the fluorescence fits.

3.6.2 Results - Magnetic Field

The effects of a magnetic field bias on the NV- centre results in Zeeman splitting, which, in CWODMR, appears as two distinct dips in the fit. Monitoring the spread of these dips can indicate a relative shift in the magnetic field within the same sample. Data presented in Fig. 3.15 demonstrates the magnetic splitting.

Data is acquired using a 90 nm FND mounted in de-ionised water using epifluorescence. Acquisition time is 200 ms. The camera gain is 5 dB, and each frequency is averaged over 10 repeats.

Plots shown in Fig. 3.15 show the splitting before a magnetic field is applied, which is determined to be separated by 14 MHz. After moving a single Neodymium magnet (approximately 0.7 T) into proximity and repeating the measurement, the separation is now 32 MHz. This is expected via Zeeman splitting of the spin states. There is also a perceived difference in the weighting of the spin states, where the greater contribution is attributed to the $|-1\rangle$ state before magnetism and the $|+1\rangle$ state after magnetism, which could be due to further strain on the crystalline structure in the presence of a magnetic field. The scales and spin-state weighting are consistent with previously published research. [78]

Previously, the importance of spectral contrast for CWODMR measurements is discussed; these graphs demonstrate it. When both states overlap, the contrast is much higher because they reinforce each other. However, there is less shared contribution after Zeeman splitting, so the contrast is 4% lower.

3.6.3 Results - Iron(III)Oxide Magnetoparticles

Fe(III)O nanoparticles are used in NV- sensing for *C. elegans* to stress the sample [77]. Because these nanoparticles are known to exhibit magnetic properties when exposed to a magnetic field, these nanoparticles are used to determine if there would be any adverse

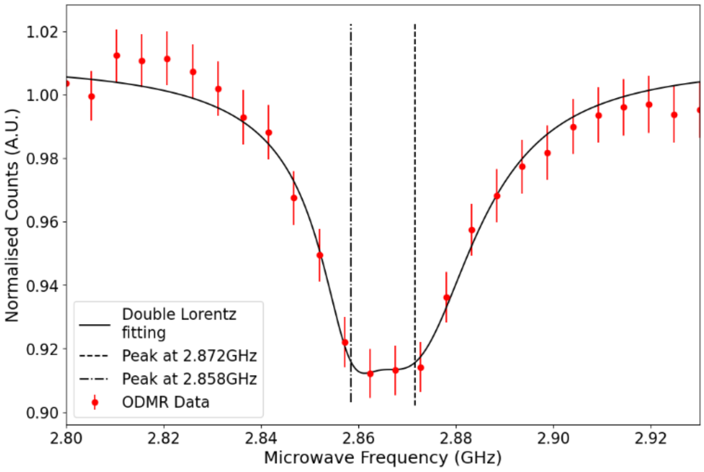

(a) No magnetism

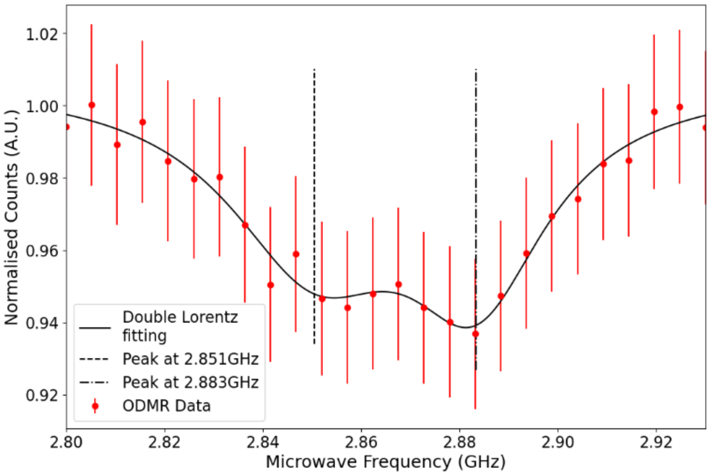

(b) One magnet

Figure 3.15: CWODMR between 2.8GHz and 2.930GHz with 5MHz steps, with and without a magnetic field applied on the same suspected single FND.

effects on the CWODMR spectra produced in proximity to the magnetoparticle.

The effects of Zeeman splitting are evident between all three spectra produced in Fig. 3.16. When no magnetic field is applied, the separation is 15 MHz; with one magnet, it is 30 MHz; and with two magnets, it is 149 MHz, which produces a larger magnetic field, clearly demonstrating the effect of a larger magnetic field on the magnitude of the Zeeman splitting.

Contributions to the contrast also match expectations, with overall peak contrast decreasing as the spin states are further separated. Noise also stays within expectation from a spectrum produced with epifluorescence excitation. Contribution to the weighting of the spin states is similar; however, in both cases, a larger bandwidth is evident in the $|-1\rangle$ spin state, vastly so in the sample with two magnets, likely due to the additional strain in the crystalline structure or inhomogeneous broadening due to the different projection onto the NV- centre axis relative to the orientation of the defect.

3.6.4 Discussion

This system can detect magnetic field shifts. These shifts are mostly unaffected by the presence of magnetoparticles in proximity. Both Fig. 3.15 and Fig. 3.16 demonstrate this, with very similar spectra, spectral contrast, and noise. The most explicit difference is bandwidth where one magnet is applied; the fit in Fig. 3.16(b) is less accurate compared to 3.15(b), measurements are acquired with fewer repeats per frequency in the presence of magnetoparticles (10 repeats vs 32) decreasing the accuracy of an individual fluorescent frequency measurement.

This system has no known magnetic field shape or strength other than an approximate expected separation output without (14 MHz) a magnetic field and with (30 MHz) a single neodymium magnetic field. With more time, consideration could have been made to characterise further with an independent measurement of the magnetic field. These experiments would involve using a magnet with a variable magnetic field, positioned next to the sample, to hold the sample consistently in place and enable imaging of the same region of interest. Comparison of CWODMR spectra relative to the applied magnetic field, specifically the positions of the minima, would allow a direct correlation

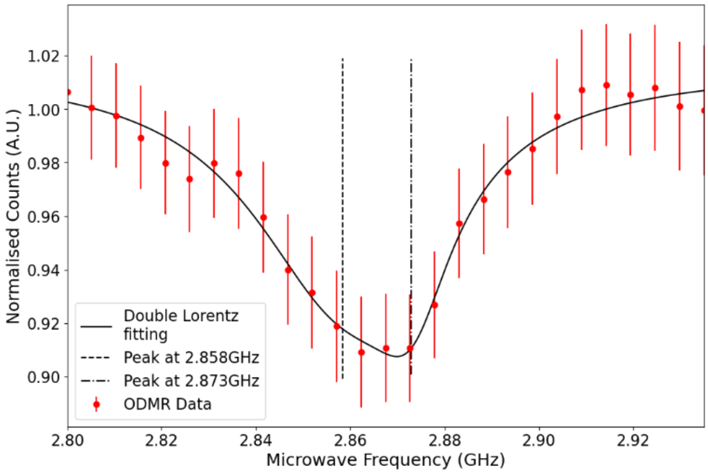

(a) No magnetism

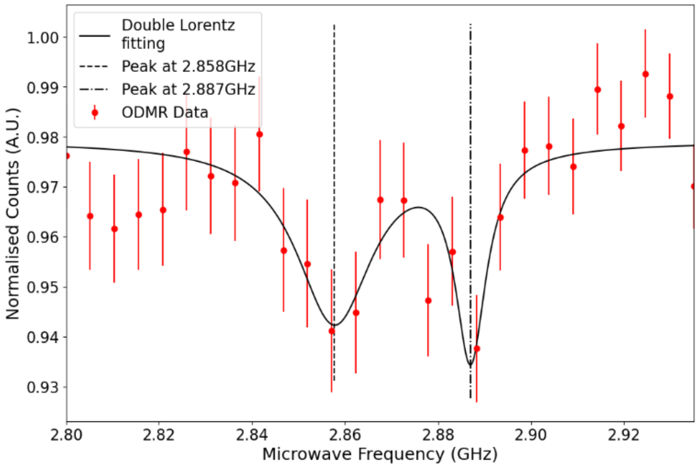

(b) One magnet

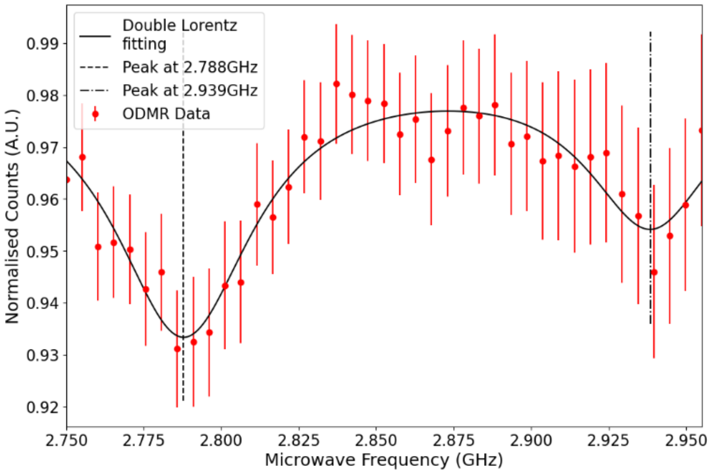

(c) Two magnets

Figure 3.16: CWODMR between 2.8GHz and 2.930GHz with 2MHz steps, all acquisition schemes the same with 32 repeats per point, where (a) and (b) are the same region of interest and (c) is different.

between spin-state separation and the applied magnetic field.

3.7 Conclusions

The system presented is capable of measuring CWODMR with results comparable to or exceeding those of previously published results from more sensitive systems [79]. Presenting total internal reflection fluorescence as a microscopical NV- centre spectroscopy method is novel and has not been reported previously. The combination with epifluorescence for dual excitation is also novel. Using epifluorescence and total internal reflection fluorescence excitation expands the range of applications in photosensitive materials, where photoactivation can cause fluorescent decay or alter the systems steady-state. Exploiting this for measurement is discussed later in this work.

Since this experiment is developmental, a large portion of the work presented is characterisation. Since widefield measurement of NV- centres using CMOS cameras is less well documented in the literature than other high-precision measurement techniques, the focus is on determining the optimal approach for acquiring and processing CWODMR spectra. Improving image contrast to identify highly optically responsive centres is vital for understanding the measurement quality possible with the system. Using SRRF, it is shown that the optically active emitters can be determined more easily. However, after measurement, implementing CLAHE proved more valuable as the dimmest structure could be taken as the closest emitter to a single crystal which reduced the confusion of multiple diamonds interacting with each other, considering the dimmest structures would have the lowest image contrast so visually would be difficult to distinguish. Further investigation could have been done to characterise the precise differences between spectra dependent on region of interest, and to automate the process by using region of interest detection to detect areas of low image contrast whilst rejecting areas with no image contrast over a set area relative to the size of the FND being imaged.

The data presented is a small selection; however, it should be noted that it is typical of the other CWODMR scans and of the processing performed. For FND clusters, it is typical to have a spectral contrast of 5-10% and noise of 2%. When single crystal FND is processed, it is common to achieve 10-18% spectral contrast and noise around 2%. [80] Measurement variation can differ across FNDs within the field of view and between datasets. The variability is due to several factors, including NV-centre-axis orientation, laser excitation, strain on individual FNDs, and microwave excitation. Despite this variation, measurement-to-measurement, the data presented in this chapter are representative of what is produced in every widefield CWODMR acquired throughout this work.

A key measurement missing from this section is the characterisation of CWODMR spectra as a function of distance from the copper wire supplying microwaves. Other researchers have already completed this work and report a decrease in spectral contrast of 1% over 300 μm, which is much larger than the field of view available to this system and agrees with preliminary data from the system that have not been presented. [35]

There is little difference between the total internal reflection fluorescence and epi-fluorescence spectroscopy outputs that cannot be explained by component differences, namely the quality of the excitation laser and the uniformity of the beam output. In epifluorescence, the spectral noise is increased because of the mode mixing present in the laser output compared to the total internal reflection fluorescence excitation, where the beam is uniform. However, for both methods, the same contrast, bandwidth, and scanning frequency are extracted from the measurements at the highest contrast. This is also true for the dual excitation despite the increase in background signal.

No deterioration in measurement quality is noted due to the use of a lower-quality microwave generator as the reference frequency. The scanning generator is of much better quality than the reference generator. This build is designed to be low-cost; implementing the lower-quality microwave generator (available for 400GBP) dramatically reduced the cost of excitation microwave equipment (TRG6000 is available for 5000GBP), without sacrificing the quality of the observed spectra.

Characterisation of the magnetic field would have been better served by using a single-variable magnet. However, this is difficult to implement. Many available magnets are only variable with the current and voltage supply, which does not directly indicate the magnetic field output of the magnet and would have required another method to measure and monitor the fields magnitude. Further, experimentation with three-axis control of the magnetic bias could have improved contrast by orienting the incident field on the crystal to maximise output; however, this is outside the scope of this work.

The acquisition time in this detector is entirely determined by the frame integration time, rather than by the scanning area as in other detectors. Reducing the detection area yields a smaller dataset for processing, enabling more information to be acquired in a shorter time. Each experiment involves maximising frame integration time, camera gain, and laser excitation power. However, this is no different from any other microscope system.

A significant drawback of this system is likely its complex assembly; experienced users of optical equipment could assemble it easily. Many parts of this system are custom and require knowledge of electronics, 3D printing, microwave delivery, hardware triggering/control, and computing. Whilst this system would cost less than another system for exact measurement, its reproducibility is complex inhibiting uptake; however, with proper presentation, it would be suitable for people looking to expand into NV- sensing.

Chapter 4

Thermometry

Thermometry in live-cell imaging is a complex process. Conventional thermometry methods are typically either very disruptive to a sample or expensive and complex for the user. However, the ability to characterise biological events - such as photosynthesis and thermogenic activity in brown apidose tissue cells - using a cell's thermal properties has long sought as a method to determine biological characteristics and chemical processes. [81], [82]

Methods for temperature sensing include the introduction of a thermocouple comprising a tungsten substrate, polyurethane, and platinum for insertion into individual cells. [83] These probes had great response rates to thermal deviations of 400 ns and matched the measured thermal deviation compared to macro-probes. Insertion into a cell required micromanipulation and provided information on the cell's drug reactivity. However, the authors note that this disruption is significant and could influence key metabolic and physiological processes they are trying to measure. [84] Moreover, the experimental design requires extensive knowledge of the apparatus.

A non-invasive, non-fluorescent method is a bimaterial micro-cantilever. [85] This cantilever is comprised of gold and silver nitride and bends when exposed to a temperature differential in proximity to the cell. As a non-invasive technique, this allows cells to be observed in a natural state. This method has been used to detect a total shift of 0.4 K in brown adipocyte cells that have been stimulated using norepinephrine and has been characterised for a total variation of 15 K. This method benefits from not distorting the natural biology of a cell, however, it cannot be used for more than a single cell to determine where the temperature change is occuring so multi-cellular organisms are not suitable for this method. Complex manufacturing is also involved in producing the microcantilever.

Finally, many fluorescent thermometry techniques exist, including genetically coded thermometers, quantum dots, synthetic polymers and gold nanoclusters. [86] Many of these techniques rely on fluorescent lifetimes to estimate the temperature differential observed. Fluorescent lifetime imaging microscopy (FLIM) is a lengthy process that requires costly pulsed lasers and is sensitive or undersampled in the time domain, depending on the method used. [87] Gold nanocrystals can also cause heating themselves within cells and have been used for such purposes. [88] These methods present some of the issues discussed previously and require experienced users or costly methods to achieve temperature resolutions of 0.5 K.

Fluorescent nanodiamond (FND) has been shown to have promising thermometry detection with *C. elegans*, where the experimental method injected NV- centre dense FND into the gonad, and the head is heated to determine the temperature dispersion within the organism. [6] The temperature resolution reached 0.22 K, which is more precise than the other methods presented. To achieve this, four points are selected to track the intersection of two lines, reducing acquisition time and increasing the sample density achievable in a short time. This system relies on an avalanche photodiode for fluorescence detection, coupled with a CCD camera for widefield imaging via a flipping mirror to redirect the detection beam. [89]

Considered factors included the custom-designed bath for characterising the individual's thermodynamic response to the experiment, and the increased noise associated with CMOS detection, which may have caused much greater deviations between intersections in four-point steady-state measurements. Using CMOS detection would facilitate whole-body detection throughout acquisition and reduce the complexity of the optical pathway required to acquire spatial information with a highly biocompatible, minimally invasive measurement technique that could be applied to systems larger than a single cell.

This chapter aims to explore the feasibility of characterising the temperature response of Nitrogen vacancy (NV-) centres using thermistors. A temperature bath is designed so these measurements could be taken in steady state, which is required for the characterisation of the thermometry response for NV- centres, because NV- centres have a different temperature per frequency response depending on the size of the nanodiamond. A proportional-integral-derivative (PID) device is used to control the temperature of the bath, and the thermistor is coupled into this to maintain a steady temperature, so the NV- response could be measured without fluctuation. Therefore, the interaction of the thermistor and the microwave excitation had to be characterised to ensure there are no anomalous readings that would cause temperature variation before the CMOS measurement.

The microwave excitation does interact with the thermistor, so characterising that interaction became the focus to determine whether it is a limiting factor. However, even without full NV- temperature characterisation, a qualitative discussion can be had about the ability to sense thermometry instead of a quantitative measurement, which is discussed in Section 6.4.

4.1 Experimental Design

The experimental design for this Chapter is split into three main components: the electronics required, a bath to homogenise the heat load, and mechanical designs for direct cover slip application to the heating element.

4.1.1 Electronics

The thermometry measurements utilised a custom temperature control stage. The electronics on this stage comprised a thermistor, PID control unit motherboard (MTDEVAL1, ThorLabs, Germany) and daughterboard (MTD1020T/MTD415TE, ThorLabs, Germany), and a heating element (TECH5S, ThorLabs, Germany). The motherboard has an interchangeable daughterboard that allows switching between different thermistor types to communicate PID feedback and maintain the temperature set by the heating element.

4.1.2 Direct Coverslip Application

Mechanically, a sample is adhered to the "cold" face of the heating element using oil, which has high thermal conductivity for heat transfer. The "warm" face of the heating element is then in contact with the x, y, and z stage via an aluminium block, with heat paste to dissipate the heat generated by the Peltier and improve the unit's energy efficiency.

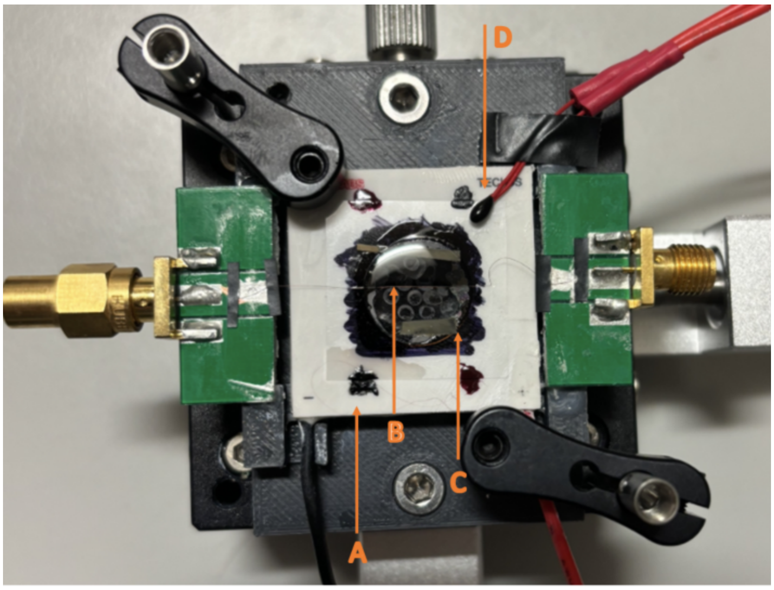

Figure 4.1: Picture of the experimental set up where (A) indicates the peltier unit, (B) the copper wire for microwave delivery, (C) is the coverslip with heat paste on its backside and (D) is the thermistor used for temperature reading in the PID unit.

4.1.3 Bath for Heat Load Control

Instead of direct coverslip adherence to the heating element, the use of a bath is optional; the bath is filled with glycerol, heated to a temperature, and that temperature is recorded. The benefit of adhering to the bath vs direct heating is an increased response time to small fluctuations in the Peltier heating and cooling, thereby dampening them and improving stability. The bath temperature can be recorded using a handheld thermometer.

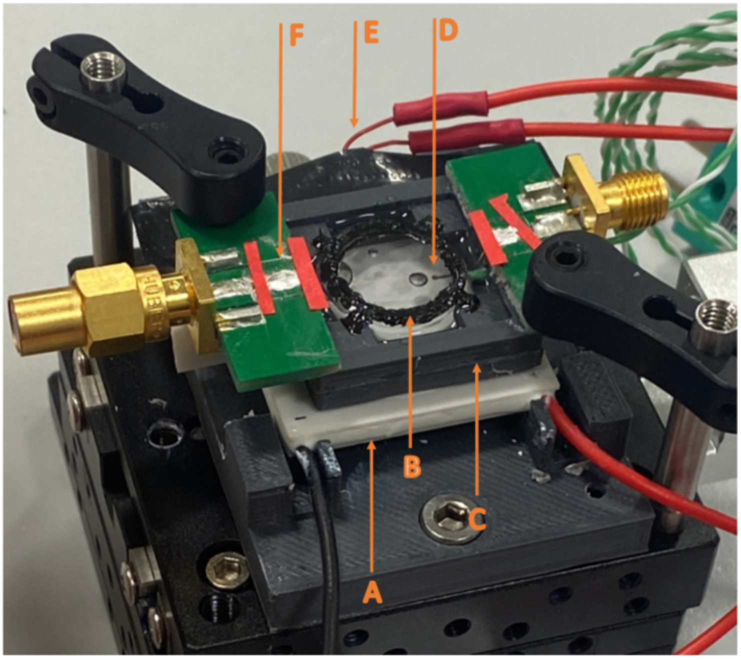

Figure 4.2: Picture of the experimental set up where (A) indicates the peltier unit, (B) the sample (C) is the bath with glycerol, (D) is the thermistor embedded in the bath to monitor the bath temperature on a handheld device, (E) is the thermistor used for temperature reading in the PID unit and (F) shows where the copper wire for microwave delivery attaches to the PCB.

4.2 Temperature Stability in Bath

Initial testing is done to ensure the heat bath could sufficiently increase and decrease temperature without rapid fluctuations. To do so, the bath is set up with a K-type handheld thermometer, the heating element is set to 50^oC, and the temperature is recorded every 2 minutes until 50^oC is reached. The heating element is then turned off to record the time taken to cool back to the original temperature. The graph showing the heating/cooling cycle is displayed in Fig. 4.3.

The bath reached maximum temperature in approximately 14 minutes and cooled to room temperature in approximately 20 minutes without active cooling. This indicates that glycerol has a higher heat capacity than air. The long heating time reassures that the bath will not be affected by small temperature fluctuations resulting from the PID loop trying to maintain a steady temperature, unless it exceeds 1 minute. The

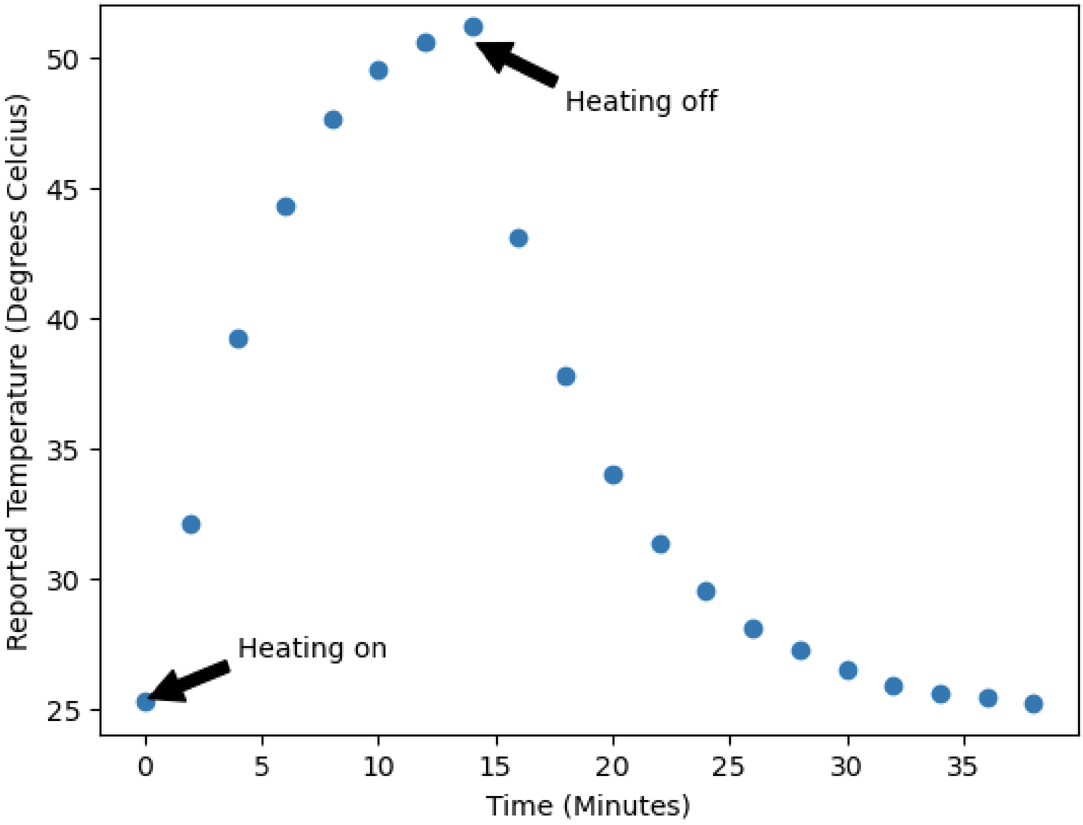

Figure 4.3: Plot showing the temperature increase and decrease of a glycerol bath with 50^{o}C heat applied via heating unit, where heating on to off is heat applied and heating off onwards is heat not being applied.

integration time is 200 ms, making it suitable for long-term stability control.

Further investigation could be conducted into the long-term stability of the bath at consistent temperatures using another probe that records temperature at a similar refresh rate to the PID temperature sensor to confirm that the bath observes no fluctuations. However, the available hardware is limited, and to include this measurement with the MTDEVAL unit, a second unit would need to be purchased and used on a separate system, since there is currently only one detection channel. However, the bath appears to maintain a steady temperature when measured at 1-minute intervals over 30 minutes.

4.3 Microwave Implementation

4.3.1 Continuous Wave Optically Detected Magnetic Resonance without Bath

To determine the extent to which initiating microwave radiation affected the system's stability, continuous wave optically detected magnetic resonance (CWODMR) is performed without additional heating from the heating element. A temperature change should have been detected if there had been a fluctuation in the incident microwave excitation. A thermistor recording is initiated, followed by the CWODMR scan to determine whether a temperature change is observable during the scan. The microwave excitation parameter is a frequency sweep from 2.800 GHz to 2.9300 GHz in 5 MHz steps with a 0 dBm output power (see Section 3.5.2). Fig. 4.4 shows the resulting temperature reading.

Since the frame integration time is set to 100 ms, each peak and trough correspond to a frame with the microwave scanning frequency applied, then the microwave reference frequency is applied for the 10 repeats per frequency. Notably, the temperature differential between scanning and reference generators depends on the scanning generator's frequency output. The various sections are indicated in the image to allow a quick approximation of the frequency applied by the scanning generator. At lower frequencies, this temperature differential is around 2 ^{o}C, whereas at higher frequencies it is almost 6 ^{o}C. This change is not linear: the temperature differential at 2.800 GHz and 2.865 GHz is comparable, as is that at 2.815 GHz and 2.865 GHz, yet no comparison can be made at the end of the spectrum.

The high/low variation at rapid intervals suggests it is unlikely to be a direct temperature measurement. Instead, coupling the microwaves to the thermistor yields an inaccurate measurement that is not related to the actual temperature. This variation limits the ability to conduct measurements using the PID control since it is constantly trying to self-correct, and there is no nominal temperature to characterise the NV-temperature shift per frequency.

These measurements show a strong frequency dependence in the probe-registered

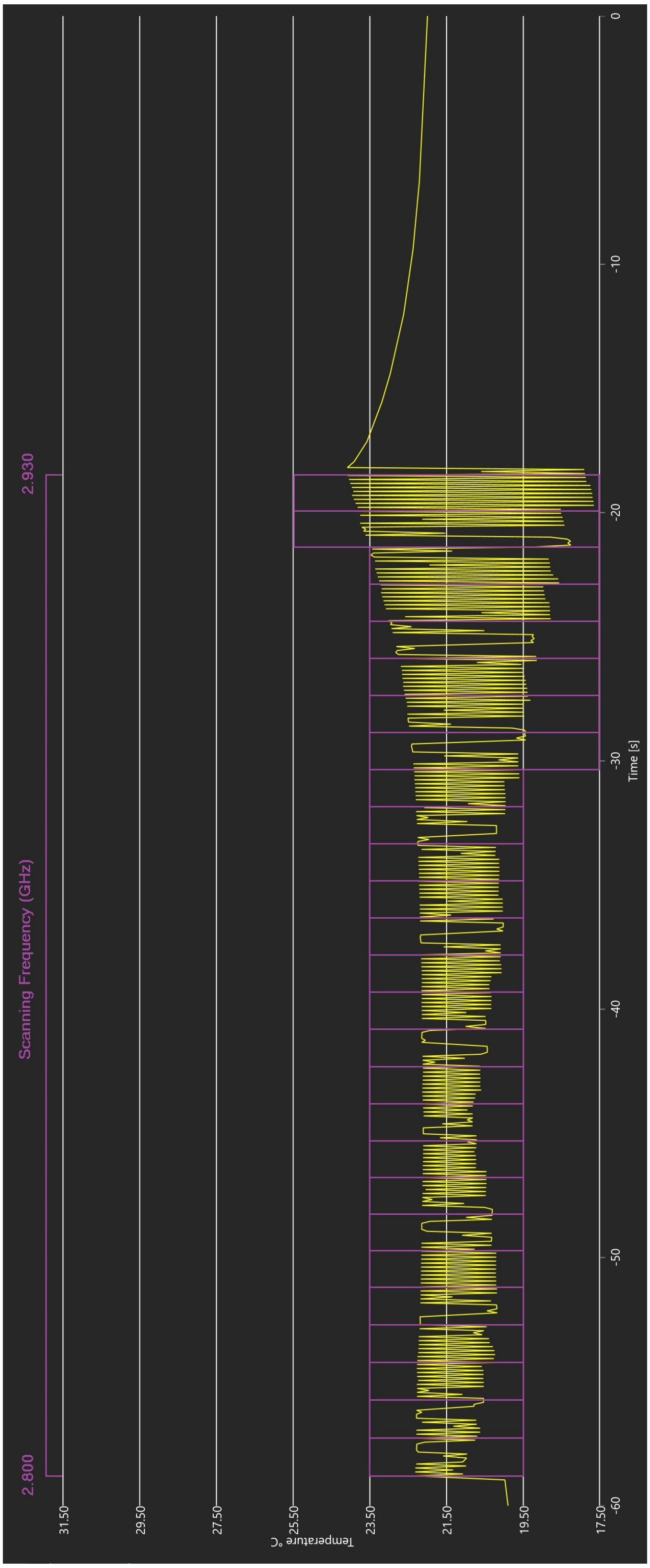

Figure 4.4: Screenshot of the temperature reported during CWODMR scan, where purple boxes indicate a single frequency.

temperature, as it varies frame-to-frame. Different applied microwave frequencies at the same nominal power might have differing heating effects, depending on their transmissibility through the silver paint and copper wire. The combination of power and frequency differences could allow the user to tune each frequency and its corresponding power to remove detection fluctuations. However, doing so would mean that what the sample is being exposed to would vary wildly, and since NV- sensing is dependent on the frequency and power of the microwaves applied, the measurement itself would not be valid. [90] The fluctuations in detection are a hardware issue and not representative of the microwaves being the cause of temperature fluctuations. However, these fluctuations from high to low, dependent on the microwave source, are a feedback for temperature control, which would make temperature control unreliable. The data presented in this Chapter confirm this hypothesis, as inaccurate temperature readings impair measurement performance. Using four frequencies from four-point measurements, we attempted a power-matching protocol under the hypothesis that two separate microwave generators caused differential heating, only to realise the issue is the probe itself. The protocol is included in this work because it would provide reliable measurements in a system without the microwave calibration error.

4.3.2 Four Point Measurement Characterisation

To demonstrate how the instability recorded would be reflected in an experimental measurement, four frequencies are extracted from previous experiments, and the signal generator is programmed to output each of them. These frequencies span a narrower range than those tested above, as they relate directly to CWODMR and are typically centred around 2.875 GHz.

An initial measurement is taken with no power or frequency matching at the sample, as seen in Fig. 4.5, and hasn't been calibrated due to microwave interference, which causes inaccurate probe detection. This measurement clearly shows the exact error from previous measurements, with the maximum disparity around 3.5 ^{o}C at the highest applied frequency (2.896 GHz). The measurement is repeated to improve this, but this time included limited power matching. The reference generator's power output is

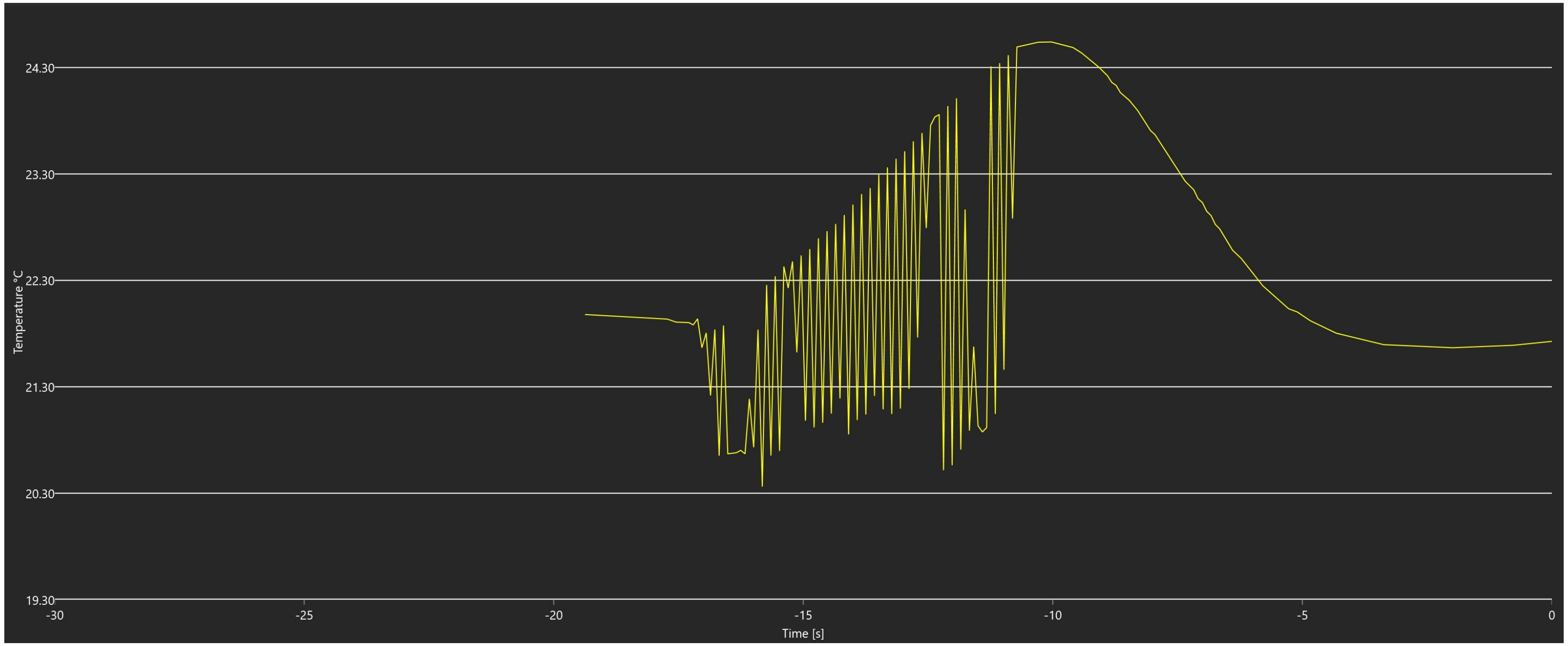

Figure 4.5: Four frequency points are extracted from previous measurements, and the signal generator is set to 2.849 GHz, 2.859 GHz, 2.882 GHz and 2.896 GHz. The reference generator is set to 2.500 GHz. Each frequency had ten repeat measurements, and each four-point measurement consisted of 10 repeats. Both generators are set to 0 dBm throughout the measurement.

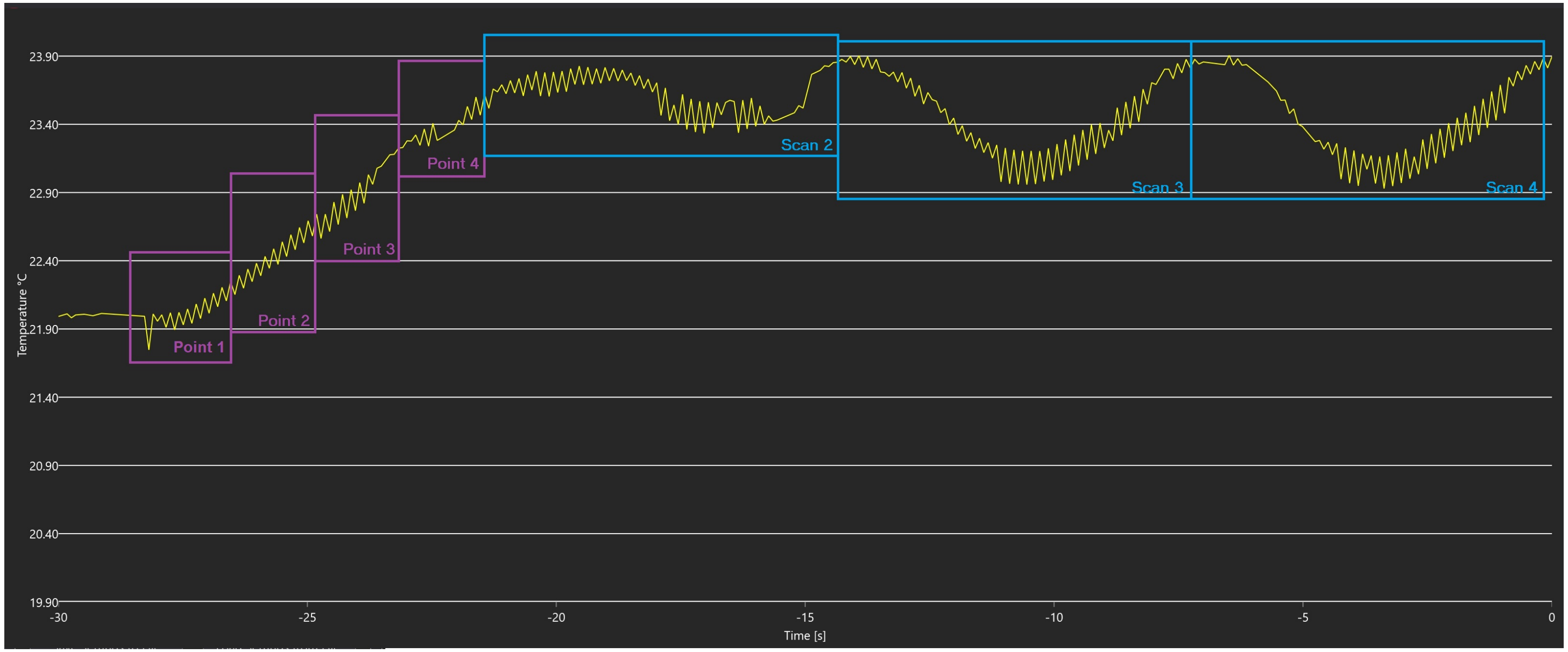

Figure 4.6: Four frequency points are extracted from previous measurements, and the signal generator is set to 2.849 GHz, 2.859 GHz, 2.882 GHz and 2.896 GHz. The reference generator is set to 2.500 GHz. Each frequency had ten repeat measurements, as indicated in (b), and each four-point measurement consisted of 40 repeats. The reference generator is set to -3 dBm, and the signal generator is set to -6 dBm, -7 dBm, -7 dBm, and -9 dBm at the respective frequencies, with multiple four-point repeats.

reduced to -35 dBm. The measurement is repeated, tuning the scanning generator's power output at each frequency until the temperature differential is minimised. The required power difference increases with frequency. This is shown in Fig. 4.6.

A measurement is performed with multiple repeats of the four frequencies to determine whether long-term stability is viable (as noted in the scan sections on the graph). As shown in points 1 through 4, tuning these powers reduced the temperature differential to less than 0.3 ^{o}C for each frequency. The overall temperature continued to increase by almost 2 ^{o}C before stabilising and entering an oscillation spanning roughly 1 ^{o}C. This oscillation caused the sample to continuously move in and out of focus on the stage due to the optical heating. Whilst the apparent temperature change (an erroneous probe measurement) is more stable when the generators' power outputs are matched, it reduces the true temperature stability, as seen at the sample plane, where focusing and defocusing are caused by temperature fluctuations.

A more in-depth discussion of the physical properties causing the interaction between thermocouples and microwave excitation can be found [91].

4.3.3 Comparison of Sensors

If the issues presented previously in this Chapter are due to hardware, changing the hardware could mitigate them. The motherboard and thermistor are replaced to see if the results persisted; the new components are MTD415TE and LMT84, a CMOS temperature sensor alternative to the previously used thermocouple, and the daughterboard for compatibility with the probe type. Data presented in Fig. 4.7 results from the temperature reported by the probe when the heating element is inactive, and the microwave generator scans through applied frequencies. There is no reference microwave frequency in this scan or the reference generator incident. This measurement aimed to test whether the probe also reacted to microwave frequency. Notable frequencies have been indicated.

An extensive microwave frequency range is explored to assess the extent of temperature fluctuations observed by the thermocouple at different frequencies. When no microwaves are incident on the sample, the thermocouple reads a temperature of

22.7 ^{o}C. When microwaves are implemented at 2073 MHz, the reported temperature increases by almost 10 ^{o}C. The most significant temperature change observed between the steady state without microwave excitation and one of the frequency set points is 20^{o}C, occurring between 2550 MHz and 2696 MHz. Of most concern is the final portion of the capture where between 2800 MHz and 2930 MHz, there is fluctuation within the normal scan range for CWODMR (2800 MHz to 2930 MHz) and around the resonant frequency (2875 MHz) of the NV- centre, meaning CWODMR and thermometry measurements cannot be completed since an accurate record of the temperature cannot be determined which means the PID loop will be constantly trying to correct the incorrect temperature leading to poor thermal stability.

4.4 Conclusions

Characterisation of the NV- centre temperature shift per frequency unit is imperative to complete quantitative thermometry measurements. Implementing a bath for temperature stability enabled homogeneous temperature control by increasing the thermal mass. Over time, this method would provide greater temperature stability, as seen in the sample, since small fluctuations in the heating element are less likely to affect it.

Implementing the microwave excitation caused issues with hardware detection; both thermistors are affected by the microwaves, leading to unpredictable temperature readings and resulting in high fluctuations in the heating element's output to compensate for reported fluctuations that are not present. Even over long-term imaging repeats, this would have resulted in a temperature uncertainty of 2^{o}C, which does not provide the stability required for the characterisation. From the literature, the expected characterisation is 75 MHz/K, meaning a 2^{o}C variation would have made readout difficult even using the 4-point method.

It would have been prudent to investigate other forms of temperature detection. However, this is limited by the types of temperature sensors compatible with the ThorLabs MTDEVAL, all of which are thermistors, which have been documented to behave erratically in the presence of microwave excitation [92]. Other detection methods are available; for example, the K-type thermistor used for the thermal bath showed no response to the microwaves, although this may be due to the handheld thermometer's slow response time. Future research would include using an electronic cold junction to improve the PID loop's temperature accuracy and implementing the Thorlabs TC300B to replace the MTDEVAL board.

As this work is done in parallel to the thermometry work presented in Section 6.4, it is essential to include the limitations characterised in this section inform those presented in the future section. The future measurements described in this work are not presented with quantitative values because the nanodiamond could not be properly characterised to determine the Hz/K shift. However, a qualitative comparison can be made, as the blue shift is evident in the change in minimum position with frequency, which is sufficient to show that thermometry can be measured using CMOS detection.

Module Name: MTD415L
Firmware Version: FW1.2.5
Temperature Range: 5°C to 45°C
UUID: 46FB97E970E6ED11A4A98

Set Temperature	25.000	°C
Temperature Window	± 1000	mK
P Share	1.000	A/K
I Share	0.200	A/(K*sec)
D Share	0.100	(A*sec)/K
Cycle Time	50	ms
Current Limit	1.00	A
Temperature Protection Delay	6	s
Critical Gain	2000	mA/K
Critical Period Duration	2000	ms

Status: Disabled
Temperature: 23.830 °C
Temperature Deviation: -1170 mK
Current: 0.00 A
Voltage: 0.00 V
Power: 0.00 W

Figure 4.7: Screenshot of temperature recorded as the applied microwave frequency is scanned through, with notable frequencies (in MHz) indicated.

Chapter 5

Allan Deviation

Noise is a well-established contributor to problems with continuous measurement, which can be characterised and evaluated to either remove or mitigate using various methods [93] Noise is variant in its source when completing sensitive measurements; it can be emergent from the mechanics in the measurement setup, such as cameras or lasers, or from environmental factors, such as ambient temperature or mechanical influence. However, there are methods to optimise measurement parameters to optimise the data acquisition required for maximal uncertainty reduction. This chapter will evaluate the use of Allan Deviation to assess noise statistics and contributions in each imaging modality by characterising the fluorescent output of NV- centres against camera and laser parameters, and determine the optimal number of repeats per frequency to improve the continuous wave optically detected magnetic resonance (CWODMR) fit.

Bayesian analysis can predict the most efficient frequency points for acquiring fluorescence measurements, thereby reducing the number of repeats required for optimal CWODMR. [94] The method in [94] cannot be applied to the microscope system presented in this work currently as continuous measurement is required with numerical values to input into the code, commonly from photodectors with 2D readout (value and frequency), compared to widefield detection with 4D readout (x, y, frequency and value) which requires the selection of region of interest after each measurement to reduce to 2D which has yet to be implemented for on-the-fly measurement rather than post-imaging processing. While the Bayesian method improves the signal-to-noise ratio typically present in nitrogen vacancy (NV-) sensing schemes, more data are required for the analysis to yield a significant improvement or to quantify the noise being rejected, since the probability is not directly related to the noise. [95]

A method for fully characterising the noise present within a system is the Allan Deviation. Developed to determine the deviation in oscillation times between two generators for atomic clocks, Allan deviation determines the deviation between a set number of time points, allowing selection to maximise the measurement parameters as presented in Section 1.4. Notably, it has not been applied to fluorescence directly despite the ability to characterise and change noise-inducing parameters and compare easily, although it has been used to characterise the noise in the output of spectroscopy measurements, such as the 4-point method in NV- sensing [89]

This chapter describes the noise characterisation for both imaging modalities by evaluating exposure time, gain, and laser power as functions of the number of repeats per measurement interval. These results are then used to evaluate whether a lower standard deviation in the number of repeats per frequency directly affects the quality of the double-Lorentzian fit in the CWODMR measurement.

5.1 Fluorescence Stability as a Function of frame integration time

5.1.1 Sample Preparation and Acquisition Scheme

Samples are prepared to allow a solution of fluorescent microspheres (FluoSpheres F8812 (580/605 nm)) to dry, so the microspheres adhered to a 16 mm round coverslip. After the solution had evaporated, de-ionised water is used as a mountant, and the slide is sealed with a 13 mm round coverslip and commercially available nail polish. To adhere to the prism, imaging immersion oil is used between a rooftop prism and a sample - fluorescent microsphere coverslip on the prism - to meet the criteria for total internal reflection by having a continuous refractive index from the prism until the sample plane.

5000 images are acquired continuously at frame integration times of 25 ms, 50 ms, 75 ms, 100 ms, and 200 ms. Camera gain and laser power are held constant throughout imaging, with camera gain set to 5 dB and laser power to 175 mW for total internal reflection fluorescence excitation and 45 mW for epifluorescence excitation. Image processing is completed using FIJI, stacks are loaded, and drift corrected using the NanoJ drift correction plugin. [11],[28] A 5x5 pixel region of interest is selected that is visible in both epifluorescence and total internal reflection fluorescence modalities, and the plot Z-axis function is used to extract the fluorescent output of that region of interest for each frame. Similarly, no region of interest is selected for the entire field of view, and the plot Z-axis function is used to extract the fluorescence from each frame. Data is then saved in a .txt file.

Allan deviation processing is done via Stable32, where plots are drift corrected in the Stable32 software to correct for axial drift by fitting to a straight line before processing for Allan fit to correct intensity drift from defocus in the z-axis.

5.1.2 Results

Acquisition time is varied to 25 ms, 50 ms, 75 ms, 100 ms, and 200 ms; camera gain is fixed at 5 dB; and the laser power remained fixed for both modalities (175 mW in total internal reflection fluorescence and 45 mW in epifluorescence). The graphs shown in Fig. 5.1 are plots for each modality, with values taken from Stable32 and imported into Python.

Different modalities use different excitation sources; as such, the Allan deviation plots between modalities cannot compare the precision of an imaging method, but rather the combination of the imaging method and the excitation source. The laser intensity variation is discussed in Section 2.5; therefore, a comparison between imaging modalities is not possible. Further, when evaluating the Allan deviation plots, τ is taken to be the number of repeats. For example, 0.05 s is the acquisition time for one frame, and the final acquisition time of 51.2 s corresponds to 1024 frames. Fig. 5.1 presents both the epifluorescence and total internal reflection fluorescence excitation resulting in fluorescence from fluorescent microspheres. Both graphs had their gradients evaluated. Looking at exposure time equal to 50 ms in epifluorescence, the initial gradient is equal

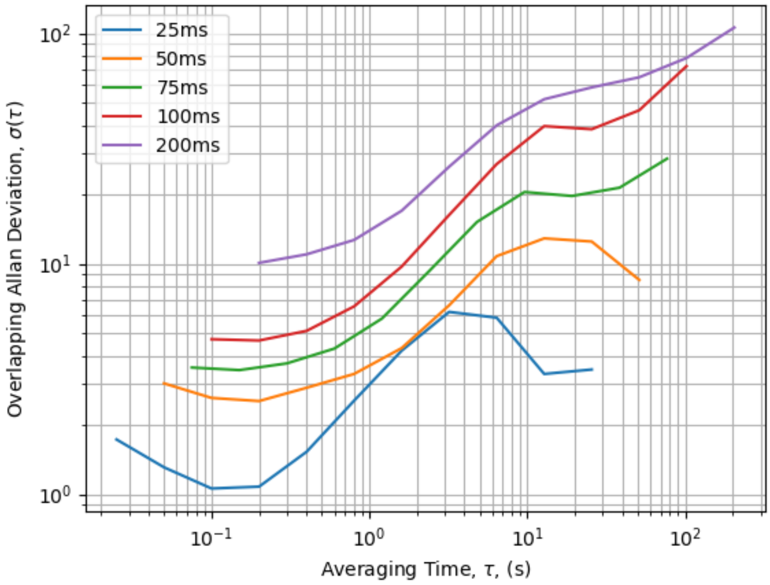

(a) Widefield Epifluorescence

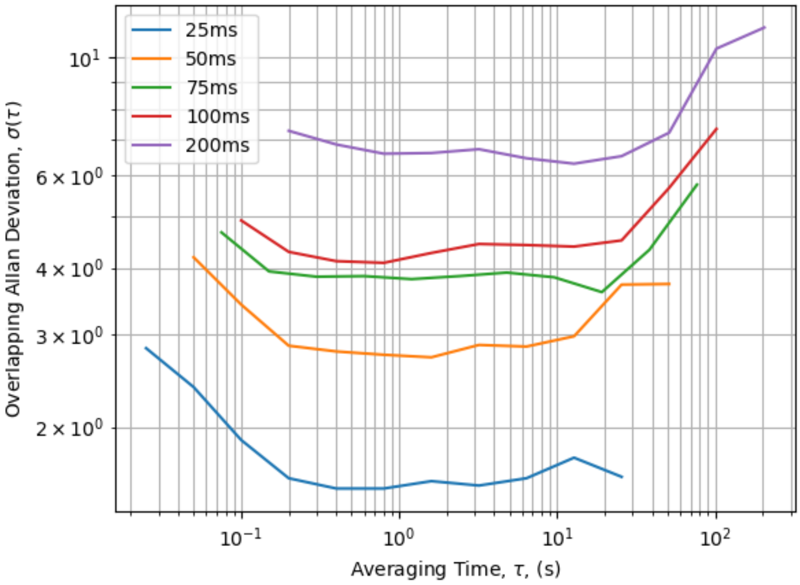

(b) Total Internal Reflection Fluorescence

Figure 5.1: Overlapping Allan deviation graphs processed using Stable32 and imported into Python for plotting, all exposure times for each modality are present, and a comparison between the epifluorescence (a) and total internal reflection fluorescence (b) modalities can be assessed.

to 0, which indicates bias instability as discussed in Section 1.4; from the 5th to the 8th data point, the gradient is 1, which correlates with rating ramp noise, this occurs when there is a slow change of intensity and it is considered stochastic - likely due to the mode walking present in the laser output - before returning to bias instability then processing into quantisation noise with a gradient of -1. Conversely, total internal reflection fluorescence at an exposure time of 50 ms starts in quantisation noise before plateauing in bias instability, showing a slight increase during the rate ramp before returning to bias instability. By comparison, the epifluorescence initially exhibits a lower standard deviation (or sigma), indicating higher precision for short-term measurements than the total internal reflection fluorescence. The difference in standard deviation is slight, 2.54 in epifluorescence and 2.71 in total internal reflection fluorescence; however, the prolonged stability over many repeats makes the total internal reflection fluorescence the more precise option since measurement times for a full CWODMR spectrum with 2 Mhz step size are more comparable to the final measurement point (1300 frames or τ equal to 51.2 s). For each frequency, higher precision is observed with 4 repeats in epifluorescence than in total internal reflection fluorescence. Still, in a full scan, higher precision is observed with total internal reflection fluorescence excitation.

5.1.3 Discussion

Epifluorescence shows a trend toward larger standard deviations at 1024 repeats, despite similar initial standard deviations for a single repeat. The increase in standard deviation is thought to propagate from the selection of a small region of interest, which, as discussed in Section 2.5, is due to the high rate of mode-hopping present within the laser profile. This is confirmed by the raw data, which show variation in frame-to-frame intensity across the region of interest. There is also a difference in acquisition time, which, when higher (e.g., 200 ms vs 25 ms), leads to a higher standard deviation. The higher standard deviation supports the theory that mode-hopping in the laser profile is causing greater deviation, since the change in frame-to-frame intensity is determined by the time it takes for the mode to hop. This relationship is not linear and stochastic, leading to the increase between the 5th and 8th points seen in Fig. 5.1

for epifluorescence, and this shows that a longer exposure time leads to higher frame-to-frame variability. Conversely, total internal reflection fluorescence provides a much lower standard deviation per repeat than the epifluorescence because it has already been demonstrated that the total internal reflection fluorescence excitation provides a less stochastic excitation across a small region of interest (Section 2.5). It can be assumed that this deviation is due to the camera rather than mode-hopping. The scope of camera noise has been discussed in Section 1.2.6. It has been noted that thermal noise increases with frame rate for many manufacturers due to the read-out process heating the pixels. For exposure times, there is a higher associated read-out noise and thermal noise contribution. The increase in both noise sources is likely why the standard deviation decreases at 25 ms and 50 ms, but increases at all other times. Because this is not a randomised noise source, the Allan deviation primarily reflects bias instability, since there is no variability in the noise source.

5.2 Fluorescence Stability as a Function of Camera Gain

5.2.1 Sample Preparation and Acquisition Scheme

Sample preparation is described in Section 5.1.1.

Frame integration time and laser power are held constant throughout imaging, with frame integration time set to 50 ms and laser power to 175 mW for total internal reflection fluorescence excitation and 45 mW for epifluorescence excitation. Camera gain is examined, with data acquired at 0 dB, 7 dB, 10 dB, 12 dB, and 15 dB.

5.2.2 Results

The Allan deviation graphs comparing camera gain followed the same trends across the respective modalities, so the graphs shown in Fig. 5.2 are the modalities, values taken from Stable32 and imported into Python for plotting.

The value comparison is similar to that of the previous section; this time, camera gain is varied over the acquisition, and the data presented in Fig. 5.2 shows the Allan deviation for each modality and respective camera gain. The epifluorescence curves

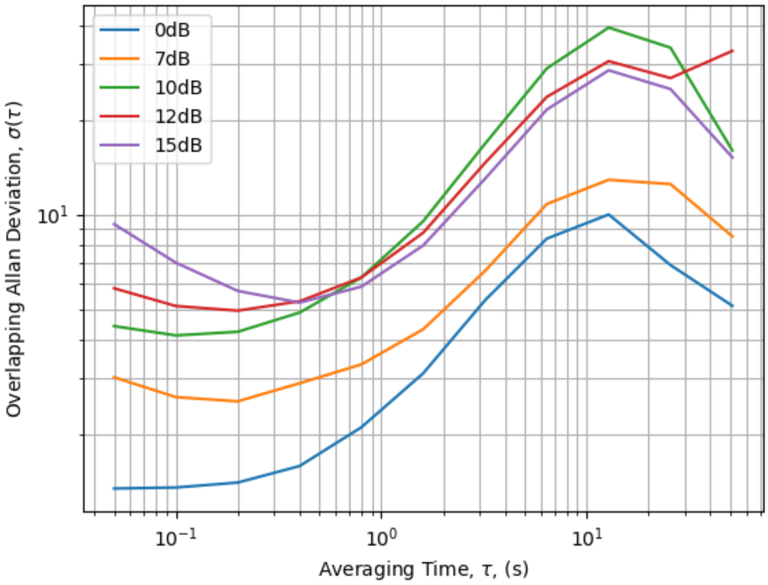

(a) Widefield Epifluorescence

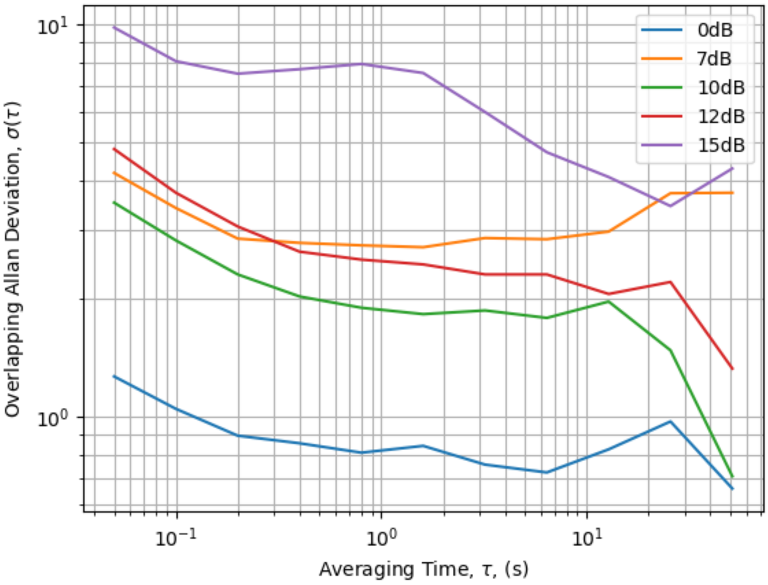

(b) Total Internal Reflection Fluorescence

Figure 5.2: Overlapping Allan deviation processed using Stable 32 and imported into Python for plotting, where all camera gains are available, and a comparison between the epifluorescence (a) and total internal reflection fluorescence (b) modalities can be assessed.

show an initial bias instability, followed by rate-ramp noise, characterised by slow, stochastic intensity changes, then briefly returning to bias instability before decreasing through quantisation noise. total internal reflection fluorescence again shows initial quantisation noise before settling into bias instability for most of the plot, then progressing into rate ramp noise or quantisation noise. The characteristics of these graphs indicate that large amounts of stochastic noise are present in the epifluorescence but not in the total internal reflection fluorescence; the total internal reflection fluorescence is more stable throughout the measurement and reaches this stability more quickly than the epifluorescence. The epifluorescence shows a lower standard deviation with fewer repeats (2.54 for 4 repeats) than total internal reflection fluorescence (2.71 for 32 repeats). However, the standard deviation for 4 total internal reflection fluorescence repeats is only marginally larger at 3.41.

5.2.3 Discussion

When comparing the effect of camera gain changes, a clear trend emerges: Allan deviation decreases for total internal reflection fluorescence but increases for epifluorescence as the sample size grows, as shown in Fig. 5.2. This divergence is attributed to the stochastic noise inherent in epifluorescence, as discussed in Section 2.5, which cannot be entirely suppressed by increasing the sample size alone.

Compared with previous results, the epifluorescence standard deviation decreases with larger sample sizes, indicating improved measurement precision. However, this improvement is limited due to the nature of camera gain. Unlike acquisition time, which changes the amount of signal collected, camera gain amplifies the existing signal. This amplification affects the magnitude of the output without altering its relationship to sample size or the original input signal.

In contrast, total internal reflection fluorescence is less affected by excitation-related stochastic noise because the sample is exposed to a uniform wavefront. As a result, the system exhibits bias instability over larger sample sizes, rather than increased noise. Since total internal reflection fluorescence does not suffer from the mode-hopping issues present in epifluorescence excitation, its precision improves with sample size, and amplified noise remains consistent, thus not obscuring measurement variation as severely. However, the sudden change into quantisation noise for some gains may indicate that the effects of gain amplification can eventually be averaged out in a sample where mode-hopping is not the dominant noise source. Although this would require further exploration to confirm by extending the number of data points acquired to ensure the trend remains in quantisation noise.

The analysis of Allan deviation under different gain settings confirms that gain amplifies the incoming signal and that output variability depends directly on input characteristics. This behaviour is well understood in camera systems; however, Allan deviation suggests that it is not overcome by increasing sample size when mode-hopping is the dominant noise source.

5.3 Fluorescence Stability as a Function of Laser Power

5.3.1 Sample Preparation and Acquisition Scheme

Sample preparation is described in Section 5.1.1.

Frame integration time and camera gain are held consistent through imaging, with frame integration time set to 50 ms and camera gain set to 5 dB. Laser power is examined, with data acquired at 175 mW, 185 mW, 200 mW, 250 mW, and 278 mW using total internal reflection fluorescence excitation; epifluorescence excitation is evaluated at 40 mW, 45 mW, 50 mW, 55 mW, and 60 mW.

5.3.2 Results

The graphs shown in Fig. 5.3 include data for all laser powers and modalities investigated.

Fig. 5.3 varies from the last two sections as the Allan deviation graph for total internal reflection fluorescence begins with quantisation noise before moving into angle random walk noise, ending in white noise. An angle random walk is attributed to thermal instability within a system, and white noise is noise not quantified at its source. Angle random walk noise cannot be corrected unless it is found to be ambient or due

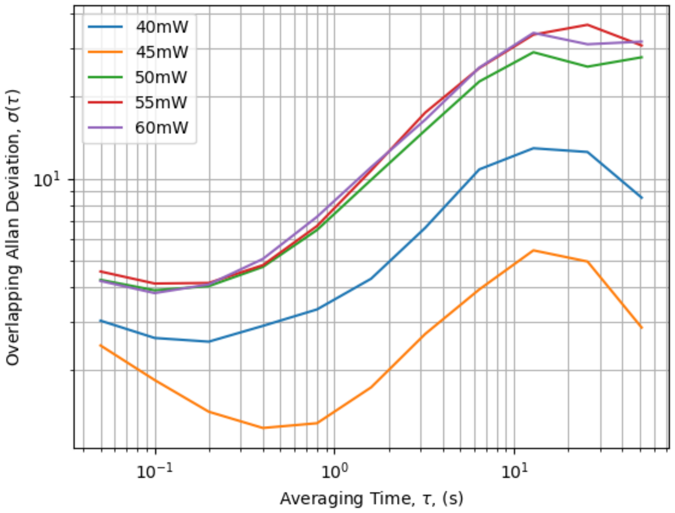

(a) Widefield Epifluorescence

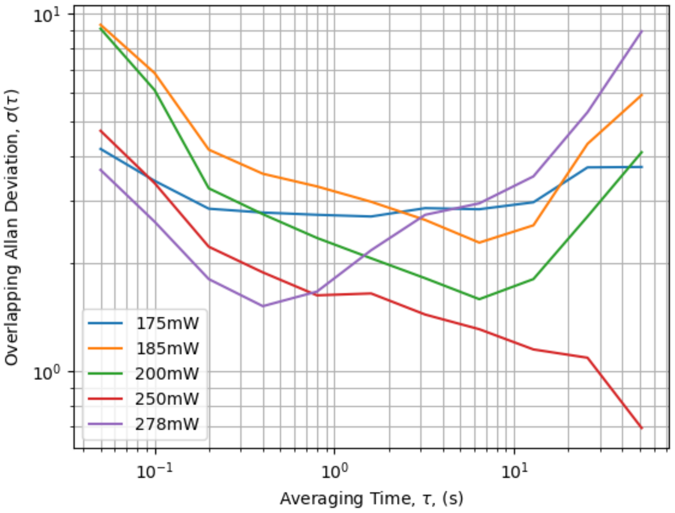

(b) Total Internal Reflection Fluorescence

Figure 5.3: Overlapping Allan deviation processed using Stable 32 and plotted in Python, where all laser powers and modalities are presented. A comparison between the epifluorescence (a) and total internal reflection fluorescence (b) modalities can be assessed.

to a piece of equipment that periodically causes considerable variation, which could be due to instability in the optical transfer when adjusting the incident power of the excitation on the prism. When angle random walk noise is present, the sample size can be increased to improve precision. However, this will not improve until the sample size is much larger than the perturbation (when this graph moves into white noise).

5.3.3 Discussion

A working hypothesis to justify the anomolous trend at 175 mW is the laser being recently turned on and hence less stable as noted in the datasheet the stability period for the laser occurs after 10 mins. For 185 mW, 200 mW, and 250 mW, increased laser input equates to higher levels of fluorescence output for the same spot, hence reducing the standard deviation as the number of photons collected is much higher for each acquisition. At 278 mW, the laser is at its maximum output, and non-linearities are observed at higher outputs, as all laser power is transmitted to the sample rather than certain polarisations, which produce higher standard deviations in averaged frames due to high fluctuations between frames. This again shows the benefit of Allan deviation, as it indicates that measurements should be made with the laser output below 250 mW at the sample to achieve statistically improved results, even though spectral contrast is improved with higher laser powers.

Despite a similar Z-axis profile for the fluorescent output, the Allan deviation graph produced shows, in Fig. 5.5, quantisation noise for smaller τ before transitioning to being dominated by random walk or drift noise. This may be due to a minor intensity fluctuation. For epifluorescence, the results are more stable than those seen in fluorescent microsphere measurements, as the Allan deviation shows quantisation noise until it reaches bias instability. Its consistently lower value distinguishes the total internal reflection fluorescence by directly comparing the standard deviations.

This confirms the previous hypothesis that the epifluorescence is primarily limited by the stability of the multi-mode fibre and the RGB laser excitation, but not by total internal reflection fluorescence excitation. To ensure the laser excitation is the source of the noise, it would have been ideal to test the total internal reflection fluorescence excitation on the epifluorescence optical path; however, this would have required a significant revision to the optical path.

5.4 Fluorescence Stability of Fluorescent Nanodiamond

5.4.1 Sample Preparation and Acquisition Scheme

A sample of 90 nm FND is prepared by diluting 1:100 in de-ionised water. It is then drop-cast and dry-adhered to an 18 mm round coverslip. A 50 micron wire (for microwave excitation) is suspended in water and then sealed with a 13 mm round coverslip and commercial nail polish. The sample is adhered to a 10 mm rooftop prism using immersion oil before standard preparation.

5.4.2 Results

Repeat measurements are conducted to validate earlier findings of increased precision with repeats and to ensure no unanticipated differences between fluorescent microspheres and FND. Since FND is less fluorescent than fluorescent microspheres at the same excitation intensities, the acquisition had to be completed at longer acquisition times and higher camera gain than those used in the previous section.

Fig. 5.4 shows the equivalent fluorescent output over time as discussed with the fluorescent microspheres; the output of the FND with epifluorescence excitation fluctuates randomly across the time of acquisition from 270 counts to 370 counts before returning to 270 counts, compared to the total internal reflection fluorescence, which steadily averages 225 counts throughout the measurement. The variation is expected because mode-hopping changes the illumination magnitude directly over the region of interest; the measurement noise shows that the epifluorescence is higher (8%) than the total internal reflection fluorescence (6%). A notable missing feature is a loss due to axial drift, confirmed by the spatial information in the raw data, as structures do not come out of focus.

A natural progression from comparing the noise of epifluorescence and total internal reflection fluorescence is to evaluate whether microwaves, integral to the CWODMR

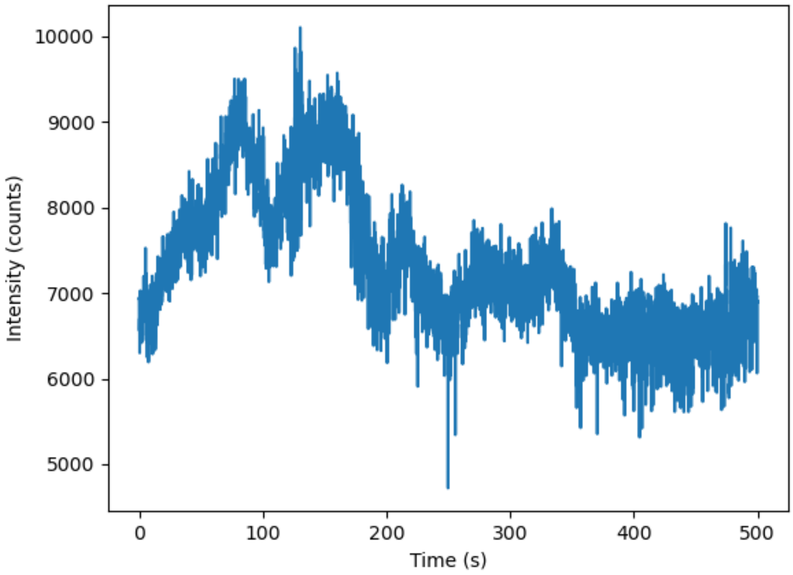

(a) Widefield Epifluorescence

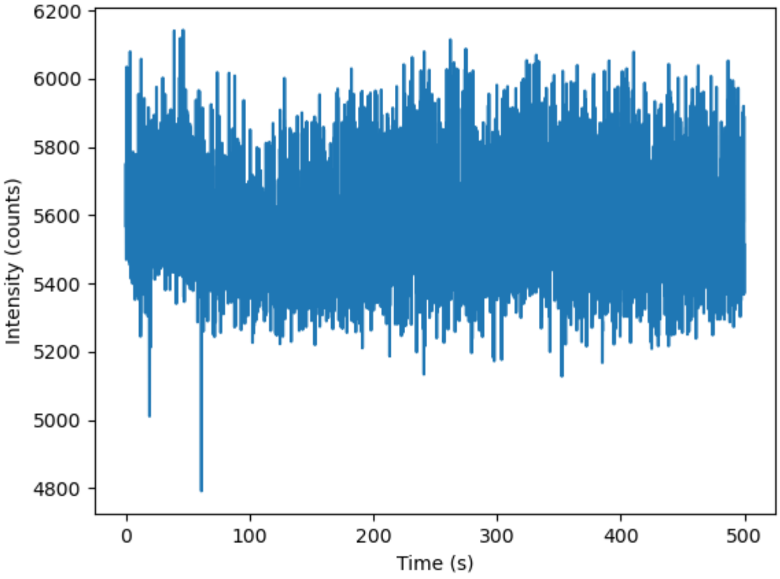

(b) Total Internal Reflection Fluorescence

Figure 5.4: Intensity of FND emission against time (ms)

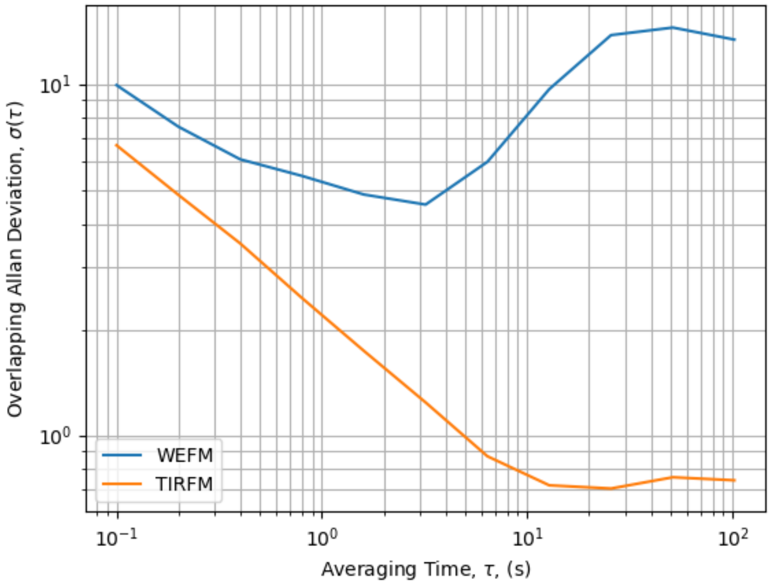

Figure 5.5: Overlapping Allan deviation processed using Stable 32 and imported to Python for plotting, where all acquisition schemes are the same for a) epifluorescence (WEFM) and b) total internal reflection fluorescence (TIRFM). Data is of continuous fluorescent output.

measurement, contribute to noise when referenced. The use of off-resonant microwave referencing is intended to reduce changes in heating caused by the on-and-off states of the microwaves typically used for referencing.

The normalisation by division of on- and off-resonant microwaves (as used in CWODMR scans) shows a marked improvement in epifluorescence fluctuations (Fig. 5.6) compared to the unnormalised case. Data presents without the magnitude fluctuations previously noted, with an average noise of 7%. total internal reflection fluorescence is still consistently better-performing, with an average noise of 4%. However, when the same normalisation is applied to resonant microwaves and no microwaves (rather than off-resonant microwaves), as time proceeds, the normalisation still increases in noise. This increase in noise is likely due to defocusing and refocusing in the raw data, caused by optical heating induced by switching microwaves on and off.

Allan deviation directly shows the benefits of referencing. Fig. 5.7 presents the Allan deviation of the normalised (division of on- and off-resonant microwaves) for both

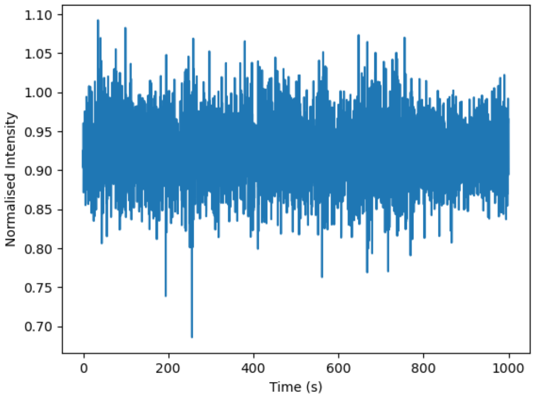

(a) Widefield Epifluorescence

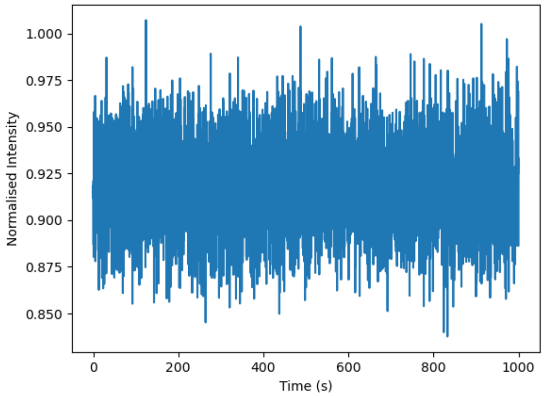

(b) Total Internal Reflection Fluorescence

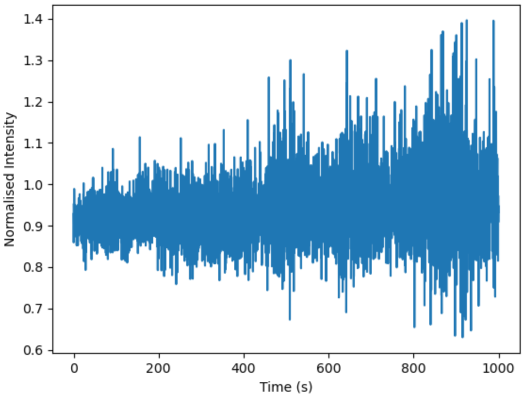

(c) Total Internal Reflection Fluorescence alternating between resonant microwaves and no microwaves

Figure 5.6: Normalised emission intensity of FND emission against time (ms)

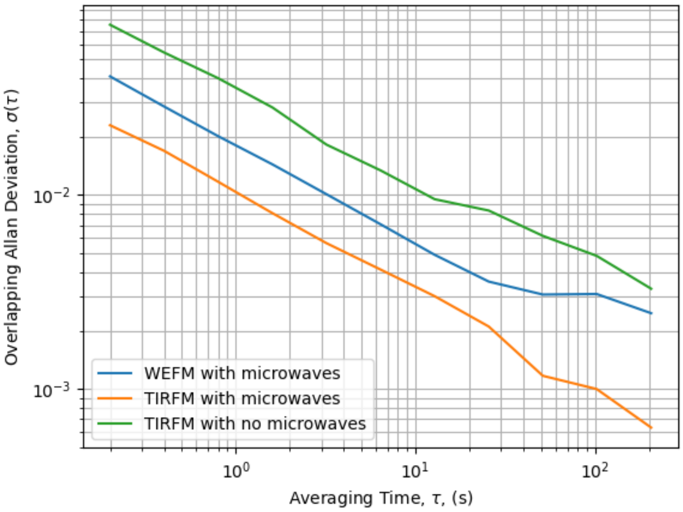

Figure 5.7: Overlapping Allan Deviation processed using Stable 32 and plotted in Python, where all acquisition schemes are the same for a) epifluorescence (WEFM), b) total internal reflection fluorescence (TIRFM), and c) total internal reflection fluorescence with no reference microwave excitation. Data is of normalised fluorescent output.

epifluorescence and total internal reflection fluorescence, and the total internal reflection fluorescence with no reference normalisation. The same continuous plot of quantisation noise with a gradient of -1/2 is evident in all three Allan deviation plots. At the same time, this is a clear improvement for epifluorescence, making its stability comparable to that of total internal reflection fluorescence without reference normalisation. Reference normalisation also improves the stability of the total internal reflection fluorescence modality, as it prevents bias instability over a longer period (or the same number of point repeats), making the data increasingly accurate as more data points are averaged.

5.4.3 Discussion

Comparing the intensity-time plot in Fig. 5.4 confirms that epifluorescence excitation applied to FND produces mode-hopping similar to that seen previously with fluorescent microspheres. Subsequently, FND in total internal reflection fluorescence is more stable over time without the decrease in fluorescent output seen in fluorescent microspheres. This indicates that the decrease in fluorescent microspheres output is due to photobleaching and mechanical drift, and that autofocus could be implemented.

Microwaves are used to manage frame-to-frame variation without introducing a heat differential by turning them off and then back on, which would cause mechanical drift and likely electrical shock to the biological specimen. To assess the effectiveness of normalisation after referencing, fluorescence intensity plots are acquired for normalisation in both modalities; normalisation is performed without reference microwaves. Fig. 5.6 shows the resulting plots. Calculating the standard variation of each result in epifluorescence = 18%; total internal reflection fluorescence = 8%, and total internal reflection fluorescence with no reference microwaves = 29%. From previous results, the standard deviation is lower in epifluorescence and total internal reflection fluorescence than in the non-referenced case. The result without microwave referencing shows a much larger deviation in total internal reflection fluorescence than even epifluorescence with referencing; the normalisation increases the precision of the measurement. This confirms that mechanical drift is produced when microwaves are turned on and off within the system.

Allan deviation plots reveal that, despite higher instability in the fluorescence output, the data still improves in precision with more point repeats after normalisation, even after 205 s. This demonstrates the benefits of normalising microwave excitation with FND, even if that referencing generates heat differentials without microwaves, which are integral for implementing CWODMR. Fig. 5.7 does show the difference in improvement; however, total internal reflection fluorescence with microwave referencing still performs better compared to epifluorescence with microwave referencing, with the lowest deviation throughout. Although total internal reflection fluorescence without microwave referencing performs similarly to the epifluorescence with microwave referencing. This further confirms the instability of epifluorescence in this system and proves that total internal reflection fluorescence is the better option for stable, long-term measurements and that employing microwave referencing dramatically improves them.

Number of Repeats	Allan Deviation		Average CWODMR Scan Deviation	
	Epifluorescence	Total Internal Reflection Fluorescence	Epifluorescence	Total Internal Reflection Fluorescence
2	0.0286	0.0169	0.0144	0.0213
32	0.0101	0.0057	0.0055	0.0093

Table 5.1: Comparison of deviation calculated by the Stable32 software for the Allan deviation from normalised reference data presented in Fig. 5.7 ignoring changing frequency, and the average standard deviation of the frequency points measured in CWODMR shown in Fig. 5.8 and 5.9 by calculating the deviation of each frequency point and averaging across the full frequency spectrum.

5.5 Applying Allan Deviation to Nitrogen Vacancy Sensing

5.5.1 Sample Preparation and Acquisition Scheme

The same sample is used as in Section 5.4. The frame integration time is set to 100 ms, and the camera gain is set to 10 dB. A CWODMR scan is acquired from 2.800 GHz to 2.930 GHz with a 2 MHz step size, 2 repeats per frequency, and 32 repeats per frequency for each imaging modality, with the reference frequency set to 2.500 GHz.

5.5.2 Results

Allan deviation indicates the balance between averaging to reduce the effects of noise-dependent sampling perturbations and exacerbating them at different timescales. To that end, we compare the variation between 2 and 32 point repeats to the normalised Allan deviation in Section 5.4.

Due to the low repetition rate with 2 repeats per frequency, CWODMR spectra in Fig. 5.8 could be better fit to a double Lorentzian. A poor fit of the double Lorentzian typically indicates undersampling, either in the number of repeats per frequency, causing inaccurate normalised fluorescent intensity, or in the number of frequency points, which is too low and provides insufficient information to fit accurately. The data lack sufficient information to produce a precise plot for meaningful interpretation and to visualise the characteristic fluorescence dip for comparison with other repeats.

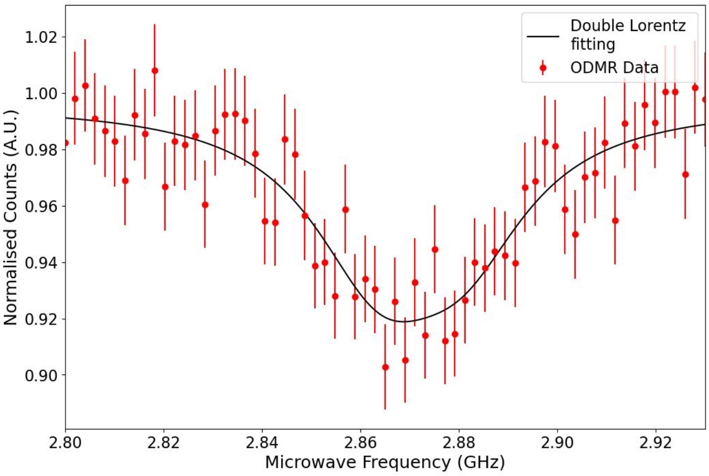

(a) Widefield Epifluorescence

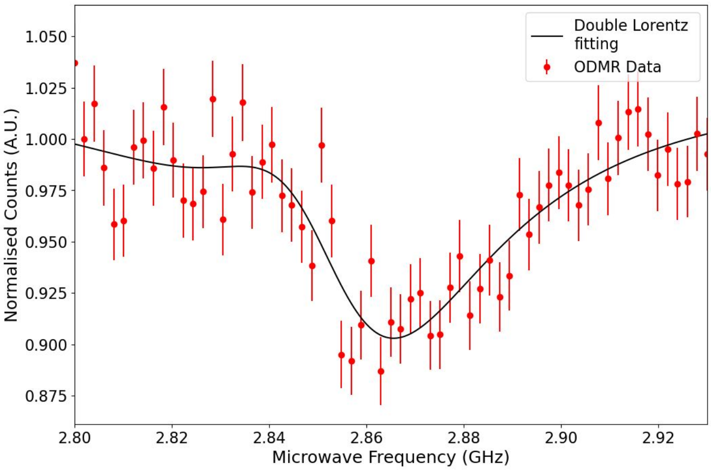

(b) Total Internal Reflection Fluorescence

Figure 5.8: CWODMR between 2.800 GHz and 2.930 GHz with 2 MHz steps, all acquisition schemes the same with 2 repeats per point from the same FND.

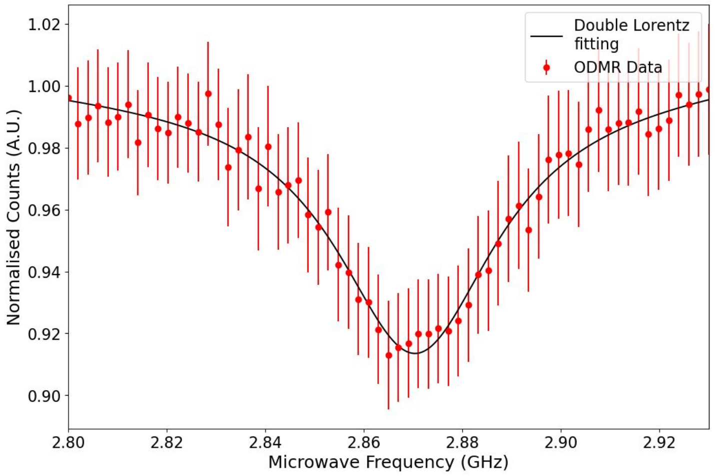

(a) Widefield Epifluorescence

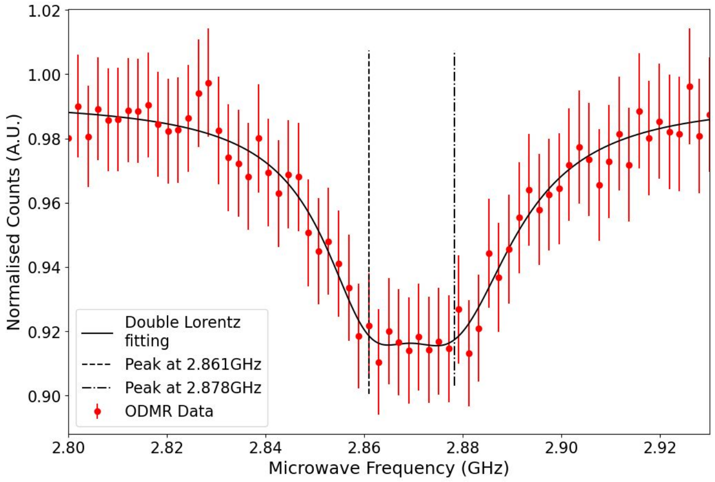

(b) Total Internal Reflection Fluorescence

Figure 5.9: CWODMR between 2.800 GHz and 2.930 GHz with 2 MHz steps, all acquisition schemes the same with 32 repeats per point from the same FND.

5.5.3 Discussion

Having collected all data on fluorescence stability and used them to inform acquisition schemes and preferred imaging modalities, experiments are designed to verify whether the Allan deviation directly translates into useful information about the sampling of point repeats in CWODMR measurements. Plots for 2 and 32 repeats can be compared using the Allan deviation and the fit deviation determined by the double-Lorentzian processing code for CWODMR. Pulling the number from the Allan deviation graphs presented in Fig. 5.7, Table 5.1 is compiled against the deviation of the data points from the fit.

The data presented in this table show that for epifluorescence, the Allan deviation is half that predicted by the fit. Qualitatively observing Fig. 5.8 and Fig. 5.9, it can be seen that the deviation to the fit is roughly improved by a factor of 2, which would lead to a noise improvement of approximately 2%, decreasing to 1% with respect to that predicted in the Allan deviation. The curve has a similar full-width half-maximum and spectral contrast.

Total internal reflection fluorescence, however, shows an increase in the deviation calculated from Allan deviation to the deviation from the fit. Again, qualitatively evaluating the curves, the fit in Fig. 5.8 could be improved; no distinct double peak is evident where the code fit one, and the curve should be more similar to the epifluorescence curve. Spectral noise is also doubled in this attempt to 2% (the error bar on each frequency point); a sample of two-point repeats produces large fluctuations because the sample size is reduced. Alongside this, with 32 repeats, the fit is not good; deviations on either side are significant and could be due to background noise or other influencing factors, since they are not present in the epifluorescence, and it has been shown that total internal reflection fluorescence excitation is more stable than epifluorescence excitation. Despite the poor qualitative fit, the deviation from the fit decreases in line with the Allan deviation values.

The process of completing Allan deviation does indicate the optimal imaging criteria. The data collected in Section 5.4 indicate that, to improve the precision of a normalised referenced frequency point measurement, the number of sample points should be increased indefinitely, and, in turn, the precision of each point should increase with the CWODMR scan, thereby reducing the error in a double Lorentzian fit. As verification, increasing the sample points would demonstrate the absence of photobleaching in FND and show the system's stability over long intervals, something that can't be demonstrated with fluorescent microspheres due to photobleaching. However, Allan deviation allows the user to identify potential noise sources. Given more time, it would be helpful to examine the effects of different acquisition schemes and compare them with the Allan deviation outputs, since a single snapshot does not account for the variation in statistical significance across frame integration time, camera gain, and laser power, all of which have different maximal criteria for each modality. Using full characterisation before imaging biological samples would reduce the imaging time required, thereby reducing phototoxicity to the organism.

5.6 Conclusions

The key motivation for this work is to determine whether Allan deviation is a valuable tool for selecting the optimal acquisition scheme for CWODMR. The reliance on imaging criteria to maximise the system's imaging efficiency is paramount when working with samples that cannot be exposed to high laser intensities or prolonged laser illumination. Allan deviation allowed comparison of statistical deviation across different imaging criteria for each available modality, which could have helped select acquisition time, camera gain, and laser intensity based on the number of repeats required to minimise deviation.

Epifluorescence consistently provided higher deviation than total internal reflection fluorescence across all parameters. This is because there is a higher background signal in the imaging of fluorescence, which decreases the signal-to-noise ratio, and the laser profile is less homogeneous with time-dependent localised fluctuations caused by the mode-hopping as shown in Fig. 5.4. As discussed in previous sections, the Allan deviation behaves appropriately for each parameter tested.

Interestingly, this deviates when comparing the number of repeats in Allan deviation with the CWODMR noise in scans with the same number of repeats per frequency. In epifluorescence, there is a proportional decrease in the Allan deviation and the deviation in the double Lorentzian fit from 2 to 32 repeats; the predicted improvement is approximately 3x. The measured improvement is approximately 2.5x. Importantly, there is still room for improvement, which supports the use of Allan deviation to determine the number of repeats required per frequency point and select the best imaging criteria. Further study would be beneficial, specifically examining how CWODMR changes with respect to imaging parameters, not just the number of repeats, and varying the number of repeats to see whether this remains on trend with the rest of the data points and is not just a product of increasing the sample size.

Allan deviation has provided insight into how sensitive the camera is to noise sources, especially within a region of interest within the field of view. It confirms what is known about noise in CMOS sensing: that gain amplifies noise, and that increasing exposure time can also increase frame-to-frame variability. However, Allan deviation has allowed an insight between the modalities, where it has been shown that the epifluorescence modality has larger variation due to inhomogeneous excitation compared to total internal reflection fluorescence, and that in NV- sensing, the use of referencing and normalisation eradicates the effect of this excitation variability.

The ability to pre-characterise the system and determine optimal CWODMR imaging parameters for different types of fluorescent nanodiamonds enables more targeted biological sensing. Instead of repeating measurements on the biological sample to achieve sufficient sensitivity for nitrogen vacancy sensing, the measurements can be performed separately. Since it is always preferable to limit laser excitation on live samples to avoid phototoxicity, this is advantageous. The ability to do this is discussed further in the next chapter.

Chapter 6

Nitrogen Vacancy Centre Spectroscopy in Biological Systems

6.1 Introduction

Measurement in biological specimens is limited by the resolution of the probe, whether spatial (dictated by the optical path and detection) or temporal (dictated by detection), both of which provide valuable information on histology, structure, behaviour, or the biological specimen's response to environmental or chemical stimuli. In fluorescence microscopy, measurements are limited by several factors, including nonspecific binding of fluorophores and the resolution of the imaging technique. The need for high temporal and spatial resolution drives research into super-resolution microscopy techniques such as CSLM, LSM, and TIRFM. Super-resolution techniques will provide spatial, temporal, and spectral information (i.e., the distribution, topography, and structure of cells). Progress has been made in thermometry and in measuring biochemical and structural characteristics at a cellular resolution using various other techniques. [96]

In terms of biological temperature sensing, fluorescent nanodiamonds (FNDs) are beneficial because they are biocompatible and, whilst a reaction is seen to local chemical differences, it is dominated by temperature and magnetic effects within a CWODMR scan. Pulsed measurements can be used to measure pH and oxygen levels via Rabi oscillations. [97] Their photostability is also a benefit for long acquisition imaging and can be exposed continuously to excitation indefinitely without concern for photodecay. However, continuous exposure to high laser powers can cause adverse effects in biological samples, leading to irregular behaviour. [98]

To test nitrogen vacancy (NV-) sensing in biology, three common biological models are imaged: *Caenorhabditis elegans*, *Tetrahymena pyriformis* and *Spirogyra varians*. *Caenorhabditis elegans* is a common biological model due to the rapid generation turnover and completely mapped neural pathways. They benefit from a precise number of cells in each adult model, which is useful for mapping and evaluating mutations within a species, and are among the easier models to cultivate. *Caenorhabditis elegans* is a roundworm member of the Nematoda phylum measuring around 1 mm in length with an average life cycle of only 3 days. [99] In adulthood, hermaphrodite *Caenorhabditis elegans* have 959 cells, estimated 20470 protein-coding genes, 35% of which have human homologues. They reproduce in two ways: self-fertilisation or hermaphrodites breeding with males. At 15 ^{o}C and in nutrient-rich conditions, they will complete all 4 larval stages in 3 days and remain in adulthood for 2 weeks. Previously, using FND, the gonads and intestine are used to determine the temperature differential when heat is applied externally. These organisms have also been used previously with FND, so they have documented preparation procedures and expected outputs for CWODMR spectra, as well as a measurement and biological model known to work. [99] Further, the optical transparency of the organism means no complex fixation and optical clearing is required for *in vivo* measurement, and cells can remain live during imaging.

Tetrahymena pyriformis is a unicellular eukaryotic organism with two nuclei. It has linear rows of cilia that pulse in unison, which have two functions: motility and directing nutrients to the oral apparatus. This oral apparatus is covered in elongated cilia, which bunch into 4 distinct bundles ("tetra"). These elongated cilia assist in movement, acting as a rudder whilst also allowing capture and consumption of nutrients. Throughout their bodies, there are discrete food vacuoles that store food until the residual vacuole expels it. The organism has been used in many genetic studies investigating RNA molecules, the cytoskeleton, endocytosis and phagocytosis, toxicology, evolution, membrane fusion, and more. [100] Their versatility is precisely why they are a choice model for biological experimentation with fast growth (doubling time approximately 3 hours). Since they are such diverse organisms, the potential for many interesting biochemical reactions is high; as such, the probability of detecting a magnetic bias or thermogenetic event is high and can be induced using various methods not discussed in this work. [5], [101] Similar to *Caenorhabditis elegans*, they are also optically transparent, and studies have been done to determine methods to reduce motility. [102]

Finally, chlorophyll in plants is chosen as a well-documented, well-understood pigment associated with photosynthesis. Photosynthesis is the biochemical process by which chlorophyll uses light to convert water and carbon dioxide into oxygen and hydrogen, or carbon dioxide and hydrogen into water, unless it is going through the dark reactions. [103] In light reactions, the reaction is endothermic; in dark reactions, the reaction is exothermic; therefore, a temperature change should be seen in the immediate environment. This temperature change can be gated since green excitation does not excite chlorophyll II; however, blue does without exciting NV- centres. We will demonstrate this with dual excitation characterisation experiments.

6.2 *Caenorhabditis elegans*

6.2.1 Methodology

Experimentation is conducted to improve current methods for cultivation, feeding, and extraction of *Caenorhabditis elegans* for imaging, aiming to maximise sample yield during feeding. [99] The current protocol for *Caenorhabditis elegans* imaging with nanodiamond is to ish a plate with *Caenorhabitis elegans* multiple times using 1 mL M9 Buffer where M9 Buffer is rinsed over the top of the agar and collected, putting this into a micro test tube and ishing 3 times with M9 Buffer, removing as much buffer as possible leaving the worms in a concentrated pellet then replacing with fresh M9 Buffer. The *Caenorhabditis elegans* are then placed in an incubator at 25^{o}C overnight in a solution of 10 μL and 20 μL MNP and FND to 80 μL M9 Buffer. The next day, this is ished 3 times again with M9 Buffer and is then ready for mounting. However, using this technique yielded a low number of *Caenorhabditis elegans* per plate, which are contaminated by the repeated ishing step and couldn't be used again because the initial ishing required to collect them continued.

Investigation into a method that would increase yield whilst allowing multiple uses of the plates is prudent. There are four methods identified for harvest before any processing with FND:

1. Removal of a section of Nemotode Growth Medium (NGM) (known as chunking) with organisms from a plate and leave in M9 Buffer overnight.
2. Chunk a section from a plate into M9 Buffer at 25^{o}C with a 200 rpm magnetic stirrer.
3. Chunk a section from a plate into M9 Buffer at 25^{o}C on a 100 rpm orbital shaker.
4. Individually select *Caenorhabitis elegans* from a plate and image.

These options varied in success, and all had their pros and cons. For example, option 4 would ensure the presence of *Caenorhabditis elegans*, but it is time-consuming and yields far fewer organisms than the other 3 options. High yield is important to increase the number of viable organisms harvested. However, option 2 has a much higher chance of destroying the samples, since a physical object is in solution. Having tested all options, these are the findings:

1. Leaving overnight with no agitation is the least likely to disturb the samples, as expected. Largely, *Caenorhabditis elegans* stayed in the NGM chunk; however, this is by far the most time-consuming option and do not yield a full harvest from the NGM.
2. The magnetic stirrer separated the *Caenorhabditis elegans* from the NGM within 5 minutes; however, any adult worms do not survive agitation.
3. The orbital shaker separated the *Caenorhabditis elegans* from the NGM within 5 minutes, also with the added benefit of not disturbing the adult worms.

4. Individual harvesting took the longest and made it very difficult to continue the steps of preparation, since starting with a much smaller yield and contaminated the plates. This method, however, is a good choice for ensuring single selection during imaging.

Due to their motility and the small field of view of the system design compared to their size, *Caenorhabditis elegans* are fixed using a solution of 1:1 Methanol: M9 Buffer for 2 minutes; this solution is strong enough to fix the sample, whilst the very short incubation time is selected to minimise the risk of dehydrating the sample. Dehydration is limited if present, as no shrinkage is visually apparent, and halting motility without additional steps to customise a mounting procedure facilitated a proof of concept for the viability of organism imaging.

After fixation, the *Caenorhabditis elegans* with 90 nm FND and MNP are placed on a coverslip and mounted in deionised water using the same method for epifluorescence exclusive mounting described in Section 3.2. The *Caenorhabditis elegans* strain used is VPR108, in which mCherry is tagged to the variably penetrant backward ventral coiler, which is present throughout the sample. mCherry peak emission is 610 nm. Using an excitation at 520 nm and a 600 nm long-pass filter, the emission from mCherry and FND is collected. Swapping to a 650 nm long-pass filter limits mCherry emission and allows FND emission to be visualised with minimal mCherry background fluorescence, providing spatial information. Images with the 600 nm long-pass filter could be subtracted from those with the 650 nm long-pass filter, since the mCherry will have higher fluorescence counts and its full emission spectrum should pass, helping better distinguish FND fluorescence from mCherry.

Datasets are acquired with the 650 nm long-pass filter in place for CWODMR measurements. Measurement parameters are 10 repeats per frequency, a scan range of 2.8000 - 2.930 GHz with 5 MHz steps, a camera gain of 15 dB, and a frame integration time of 300 ms. The resulting dataset is processed in keeping with previous work and plotted to fit a double Lorentzian.

6.2.2 Results

Fig. 6.1 shows two separate *Caenorhabditis elegans* samples, where (a) shows the mCherry channel in magenta and FND in cyan, proving there is the ability to see the spatial information of FND localisation that the system is designed for. Fig. 6.1(b) shows another *Caenorhabditis elegans* in the sample, the autofluorescence or the little mCherry fluorescence able to still pass through the 650 nm filter is evident, as this is only the FND fluorescence channel.

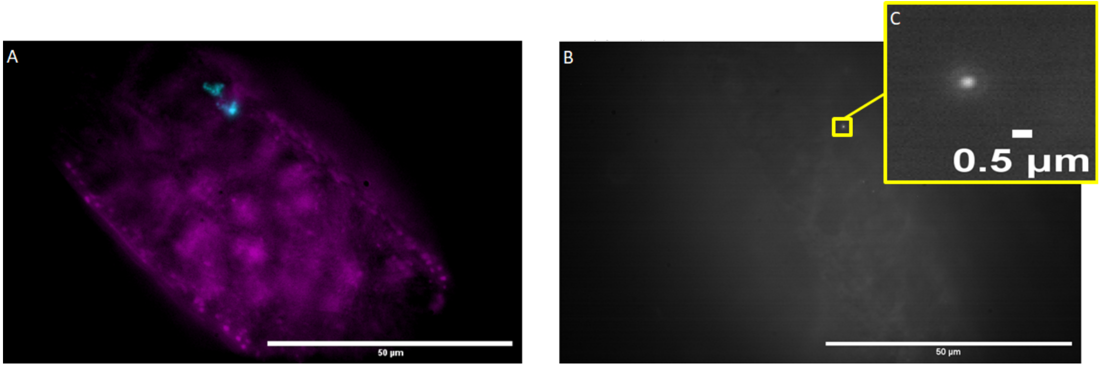

Figure 6.1: Images of fixed *Caenorhabditis elegans* where (a) is in the mCherry channel in magenta and the FND channel in cyan, (b) is another *Caenorhabditis elegans* sample in the FND channel, and (c) is a zoomed region of suspected FND.

A natural question is whether we are actually seeing FND or autofluorescence from the sample. Fig. 6.1(c) shows a region with suspected FND, due to the presence of Airy rings, which indicate it is a sub-diffraction emitter compared to the other emitters on the field of view. It appears to have stronger fluorescence at about 650 nm than the surrounding emitters, suggesting it is likely FND. [104] To check this, CWODMR is performed on the sample. Fig. 6.2 shows the ODMR curve taken from the FND.

The presence of a CWODMR spectrum clearly shows the ability to differentiate the FND in the sample. Moreover, this CWODMR spectrum shows splitting likely due to strain splitting in the absence of an applied magnetic field. The detection of CWODMR spectra is important as a test case to demonstrate that measurements can be done *in situ* using CMOS detection, and that the outputs are comparable to those already published using EMCCD, where the measured dip depth is 12% centred on 2.875 GHz and with similar splitting. [89]

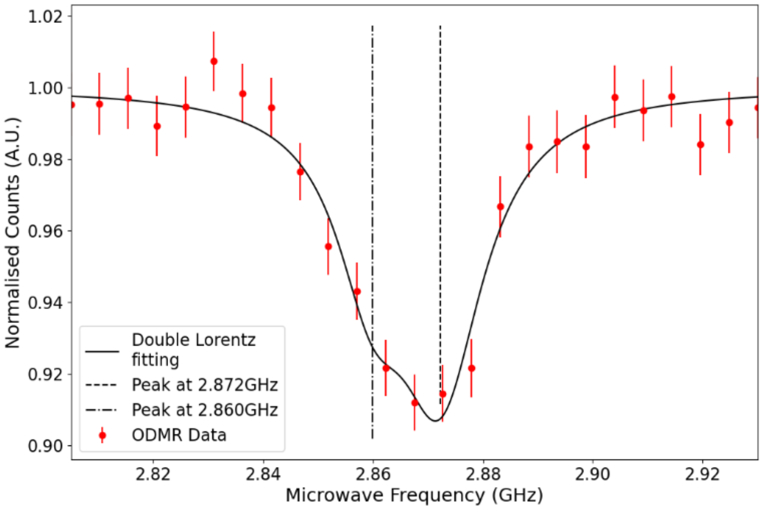

Figure 6.2: CWODMR of 90 nm FND *in situ* in *Caenorhabitis elegans* shown in Fig. 6.1.

6.3 *Tetrahymena pyriformis*

Tetrahymena pyriformis are highly motile organisms; selecting them required investigation into methods to reduce motility, given the constraints of the microscope, so that imaging could be performed with live samples. The ability to stain with propidium iodide, which becomes detectable when the organism is deceased, enabled easy differentiation between viable and non-viable cells. This section set out to demonstrate the benefits of CWODMR in widefield imaging for spatial correlation with the organism and to combine Allan Deviation methods for characterising the noise in FND and in a combination of FND and organism measurements.

6.3.1 Methodology

Initial viability of the organism after culture with FND is 100% over 6 hours and is evaluated by propidium iodide staining using time-lapse widefield fluorescence microscopy. Dibucaine Hydrochloride has been previously reported to reduce motility in the organism. Cilia are stripped from the surface on exposure to dibucaine HCl. The organism is removed from the dibucaine solution, and after approximately 30 minutes, the cilia will grow back. [105] During this study, various concentrations of dibucaine HCl are explored - 0.01, 0.1, 0.25, 0.5, 0.75, 1, 2.5, 5 and 10 mM - concentrations up to 0.75 mM does not reduce motility, and higher concentrations led to complete cell death within 20 minutes of exposure.

Methylcellulose is tested as a high-viscosity alternative to agar and agarose, previously used for the immobilisation of Zebrafish. [106] 3% solution is made by continuous heating to 80 ^{o}C and stirring until the powder had dissolved into solution. The solution is left to cool with continuous stirring until room temperature is reached, at which point stirring ceased to allow the solution to harden. In 3% methylcellulose, when mounting, *Tetrahymena pyriformis* still maintained complete motility. Attempts are made to increase the concentration, but any concentration above 3% exceeded the saturation limit and became optically opaque, making it unsuitable for imaging.

Finally, 0.5% low melting point imaging quality agarose is explored. To increase cell viability, the organism is grown in NEFF media. This combination successfully halted the organism and maintained 100% viability over 6 hours.

Tetrahymena pyriformis are prepared with an overnight feeding of 100 nm FND. For initial feeding, 1 mL of *Tetrahymena pyriformis* is collected from the stock and centrifuged for 6 mins at 2,000 rpm; the supernatant is removed, leaving the pellet. Organisms are resuspended in 200 μL of fresh NEFF media, 100 μL of 100 nm FND and 100 μL of 10 mM Propidium iodide for viability staining before being left on gentle agitation overnight. The sample is retrieved and centrifuged again at 2,000 rpm for 6 mins, and the supernatant is removed.

A stock of 0.5% low-melting-point imaging-quality agarose is prepared with NEFF media as the solvent, 7 μL is placed on a coverslip, and the mixture is allowed to partially cool. The remaining pellet (4 μL) is placed in the centre of the mounting media. A copper wire is inserted through the pellet, which is sealed with a coverslip and nail varnish.

Imaging is performed with scan parameters of 2.800-2.930 GHz, 2 MHz steps, and generator power limited to -5 dBm to reduce excess heating. Frame integration time is set to 150 ms, and camera gain is 10 dB. Laser power is 45 mA in epifluorescence configuration.

6.3.2 Results - Endocytosis of Fluorescent Nanaodiamond

A sample of *Tetrahymena pyriformis* in 100 nm FND slurry is prepared on a 0.5% low melting point agarose with a NEFF solvent base and imaged on a Zeiss Differential Interference Contrast Microscope with a 10x objective to allow visualisation of endocytosis of FND.

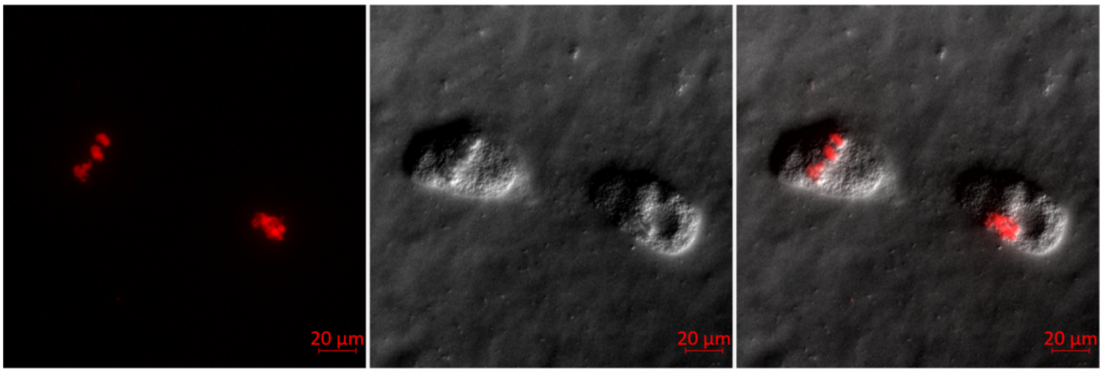

Figure 6.3: Left: FND (100 nm) fluorescence image. Middle: Differential Interference Contrast image of *T. pyriformis*. Right: Fluorescence image overlaid on DIC image.

Fig. 6.3 shows the uptake of FND after 3 hours. FND are localised in clusters in food vacuoles. This confirms that the FND are ingressing into the main body of the organism and being retained within vacuoles, indicating that CWODMR is a possible line of inquiry for this organism.

6.3.3 Results - Continuous Wave Optically Detected Magnetic Resonance with Propidium iodide Emission

Tetrahymena pyriformis are prepared using propidium iodide as a viability stain. If non-specific fluorescence is observed, it is assumed the organism had died, as this fluorescence could not be attributed to FND but rather to propidium iodide and is therefore no longer suitable for live-cell imaging. Propidium iodide is excited at a wavelength of 520 nm and fluoresces above 650 nm, thus detected in the normal detection scheme for NV- sensing. Deceased organisms could still be used to test whether CWODMR is possible within the ciliate, and there are effects to the CWODMR produced as expected in the signal-to-noise ratio/dip depth discussion in Section 1.5.2.

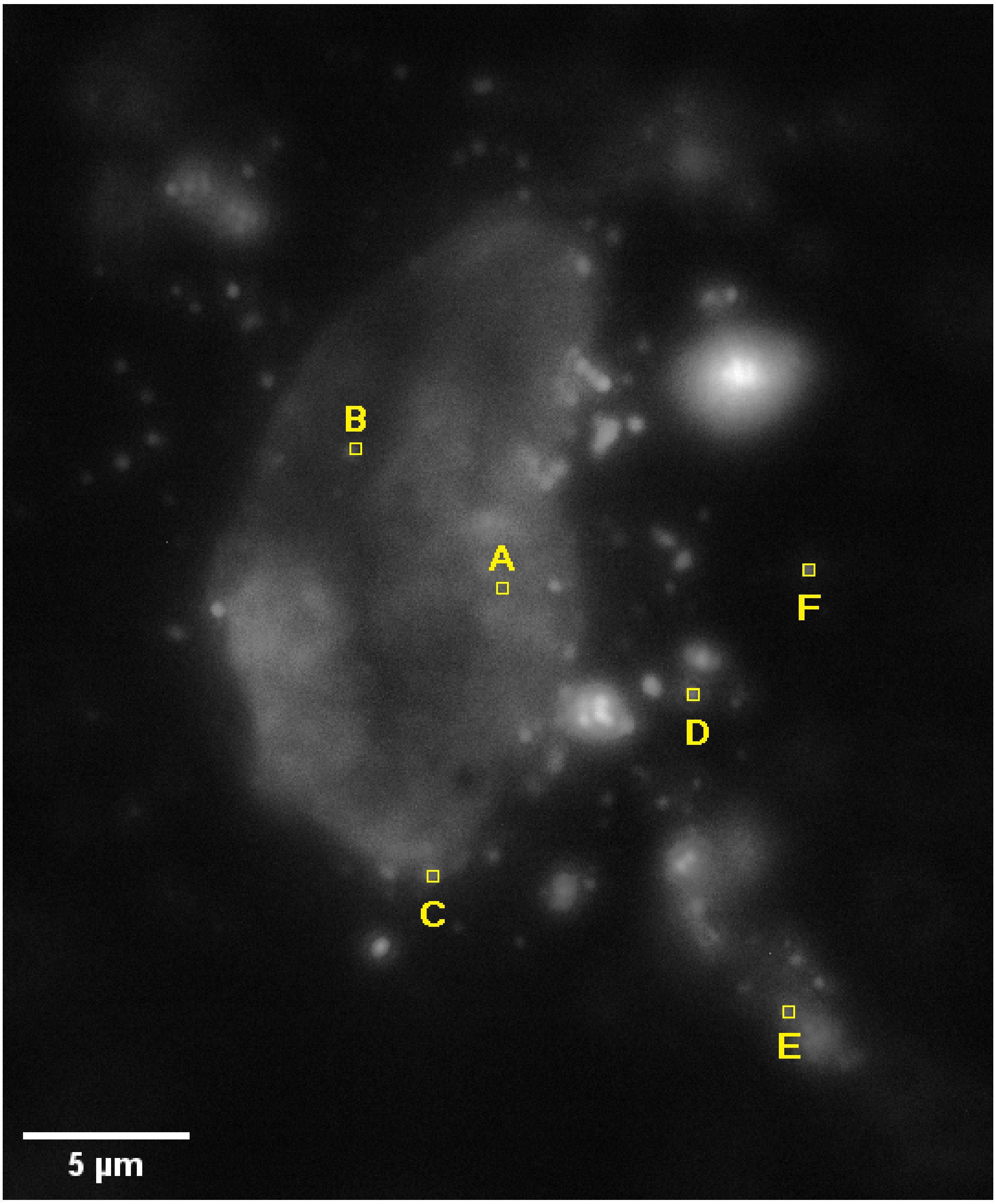

Figure 6.4: Fluorescence image of *Tetrahymena pyriformis* expressing propidium iodide and 100 nm FND. Fluorescence appears diffuse compared to previous samples since the FND are highly concentrated and emitting through the tissue. Yellow boxes indicate regions of interest from which CWODMR are extracted, as shown in Fig. 6.5. Regions of interest are selected where there is an expectation of PI expression only, FND *in situ*, or FND *in vitro*.

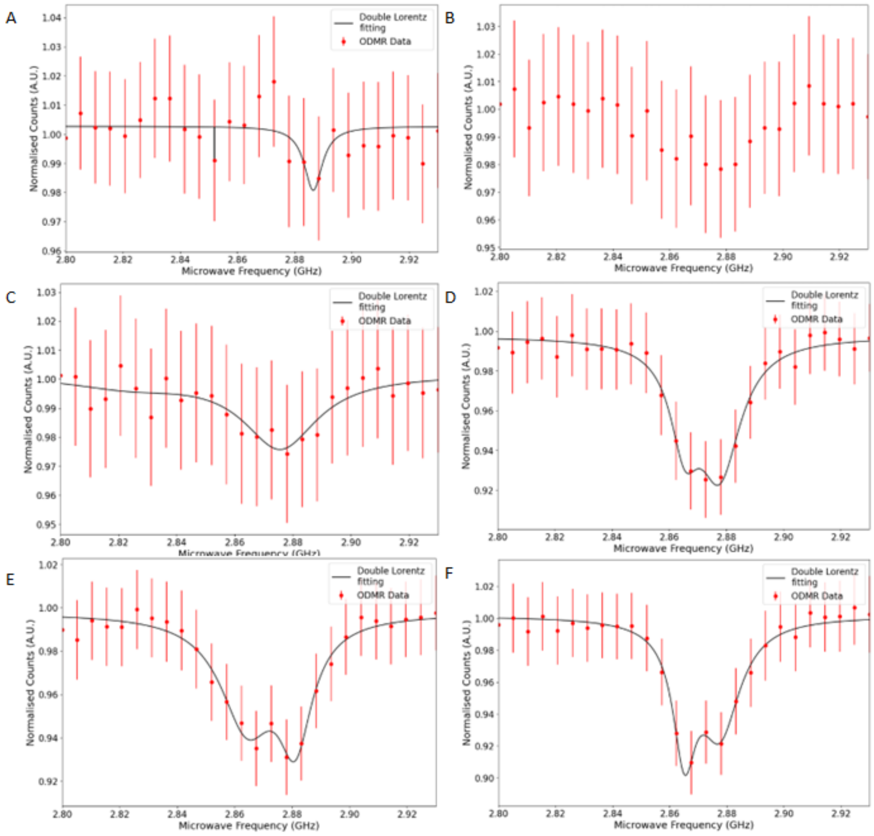

Figure 6.5: CWODMR extracted from the regions of interest indicated in Fig.6.4.

Fig. 6.4 is an example of a ciliate where FND is present with emission from PI staining. Selecting regions of interest internal to the structure and external allows comparison of various dynamic states (e.g., high vs low background signal). Internal CWODMR spectra are shown in regions A, B and C; external CWODMR spectra are shown in D, E and F. The region of interest (A) is chosen as the region with only propidium iodide fluorescence, and it detects background noise throughout the scan, which approximates to 3% of the normalised CWODMR frequency points. No fit is possible because no NVs are present in the region of interest, so spectra would not be produced in region of interest (A). Fit for region of interest (B) is impossible because the noise is much greater than the detected dip depth (3% vs 1%), despite the apparent dip being evident. This improves in latter measurements, (C) - (F) produce a CWODMR fit to the data with lower noise present (reducing to 2%) indicating that the PI emission is overwhelming the fluorescent output of the NV- centre making it more difficult to extract CWODMR data with sufficient dip depth for analysis which is discussed in Section 1.5.2. The further the FND is from the sample, the greater the dip depth, further indicating that the CWODMR dip depth is being lost due to the increase in the background signal, which is a non-responding component.

6.3.4 Results - Continuous Wave Optically Detected Magnetic Resonance in Live Cells without Propidium iodide Emission

Live cells should not emit fluorescence when stained with propidium iodide. In the same sample preparation in which propidium iodide expression is observed, some organisms are found to be live cells. Since fluorescence imaging of the organism is not possible, to provide perspective on the location of the FNDs in the specimen, the brightfield image is overlaid with the FND fluorescence image, resulting in Fig. 6.6. Regions of interest are selected to evaluate CWODMR spectra produced where fluorescence is present within and external to the organism to allow comparison of the CWODMR spectra obtained through the organism to those of FND external, which can be used as a form of control to determine to what extent the CWODMR is affected *in vivo*. Total imaging time is 3 minutes and 15 seconds.

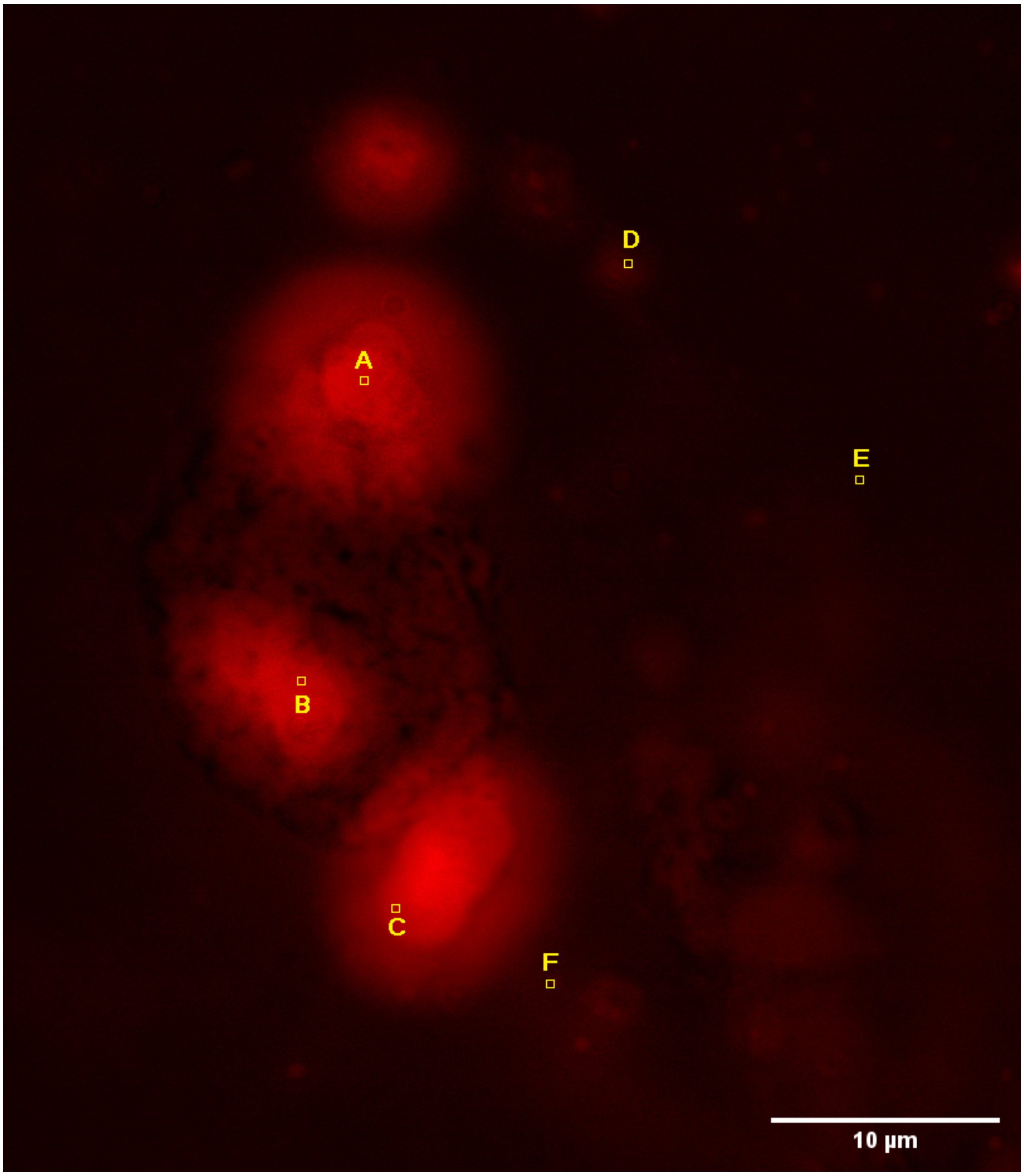

Figure 6.6: Fluorescence image of *Tetrahymena pyriformis* labelled with propidium iodide (no expression) and 100 nm FND. Yellow boxes are regions of interest where CWODMR are extracted from, shown in Fig. 6.7.

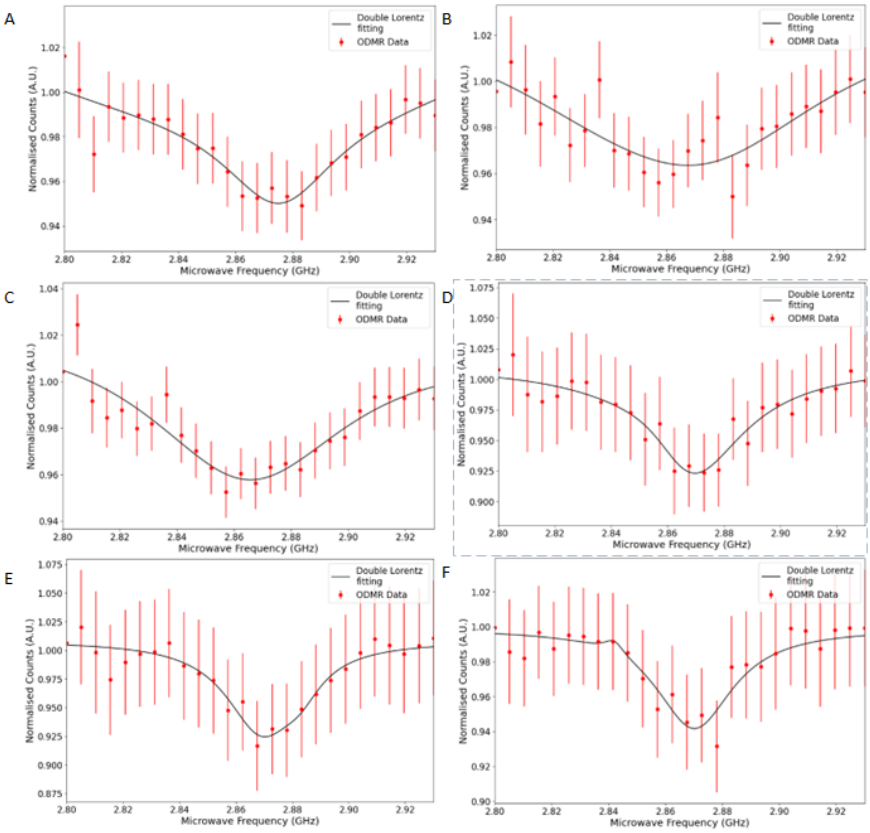

Figure 6.7: CWODMR extracted from the region of interest indicated in Fig.6.6.

Since there is no additional fluorescence as in the previous section, the CWODMR spectra in Fig. 6.7 show lower noise within the organism, approximately 2%. regions of interest (A) - (C) from within the organism produce dip depths larger than the noise at 5%, 3% and 4%, respectively.

6.3.5 Result - Allan Variance in *Tetrahymena pyriformis*

To determine the efficacy of Allan Deviation in biological systems as a method of characterising the acquisition criteria to raise the signal-to-noise ratio, the measurements performed in Chapter 4 are repeated using a region of interest selecting FND consumed by live *Tetrahymena pyriformis*. These measurements are conducted with a frame integration time of 150 ms, 10 dB camera gain and microwave power outputs set to -5 dBm (35 dBm at the sample). Initial imaging is of fluorescence output with no microwaves applied; the latter is normalised to microwave output at 2.8007 GHz (the point where the minima are most often found in a CWODMR with no temperature or magnetic field bias) and 2.500 GHz. Total imaging time is 25 minutes.

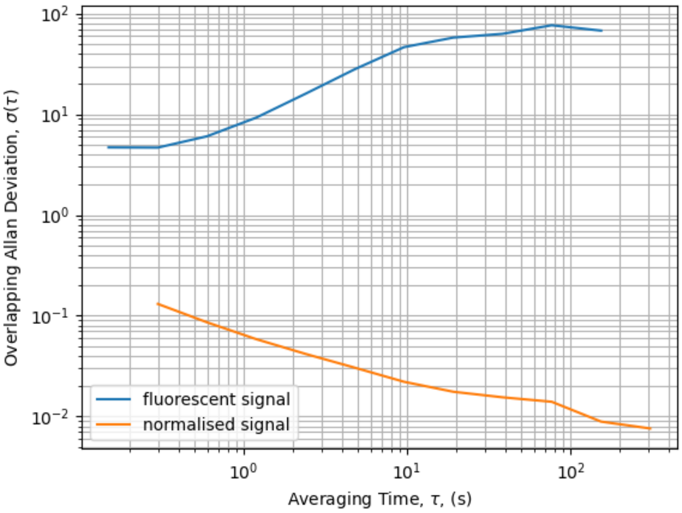

Figure 6.8: Allan Deviation produced using Stable32 software and plotted in Python. Allan deviation produced using fluorescent signal from FND within *Tetrahymena pyriformis* and using the fluorescent signal of normalised FND within the organism exposed to off- and on-resonant microwave excitation. Both plots are representative of a 150 ms camera integration time, a 10 dB camera gain, and 520 nm epifluorescence excitation.

Fig. 6.8 shows both resulting Allan deviation plots using epifluorescence excitation. These can be compared with the initial epifluorescence plots for no biological organism, as presented in Chapter 5 (Fig. 5.7). The sigma values in both graphs are of the same order of magnitude as those previously reported, demonstrating that the Allan deviation is comparable to that observed outside the organism and indicating that it need not be repeated for an emitter with the same imaging criteria within a sample. In contrast, the increase in deviation shown in the fluorescence plot is expected from previous measurements due to the inhomogeneities and speckles present in the excitation laser. Normalisation is similar to the normalisation plots shown in Chapter 5; the improvement with increased sample size is expected (as discussed in Chapter 5) and demonstrates the efficacy of referencing, even in biological material sensitive to high microwave power. Overall, this demonstrates the reliability of Allan deviation for characterising an emitter, even when the local environment of the FND is altered, such as within a biological sample rather than deionised water, where the signal must pass through a structure with varying refractive index.

6.4 *Pond Weed*

6.4.1 Maintenance

Pond Weed is collected from the Molendinar Burn on the University of Strathclyde campus near Callandish Monument ("Steelhenge") by inspection and kept in an open container, using water also collected from the burn as growth media.

6.4.2 Methodology

Pond weed is collected with 2 mL of natural pond water collected at the site. 100 μL FND (100 nm) is added to the suspension and left overnight for FND to ingress or adhere to pond weed. The sample is mounted in de-ionised water for imaging purposes following the method for total internal reflection fluorescence NV- sensing. Images are acquired with a frame integration time of 90 ms and a camera gain 10 dB. Scan parameters are 2.800-2.930 GHz with 2 MHz steps. Both generators are set to 0 dBm power output and reference frequency 2.500 GHz. Scans are taken such that the initial scan is excited at 520 nm, then at 520 nm and 450 nm, and then at 520 nm using the RGB laser in WEFM. Exciting at 520 nm doesn't excite chlorophyll II, which is the chlorophyll type targeted. Exciting at 450 nm should trigger a day cycle, inducing photosynthesis, and removing should trigger a night cycle, where photosynthesis slows. To ensure excitation using 450 nm triggers photosynthesis from a dark state, samples are dark-adapted for 24 hours, allowing all photosynthetic reactions to cease. [103]

6.4.3 Results

To determine the viability of studies on the temperature shift associated with photosynthesis, pond weed is collected, and FND is adhered to the structures. CWODMR is performed to determine whether FND are close enough to detect temperature differences (as observed when CWODMR is affected by thermal shifts). After dark adjusting for 24 hours, samples are excited with 520 nm light to excite the NV- centres, then Chlorophyll II is excited using 450 nm light to induce photosynthesis. Fig. 6.9 shows the relative distance between FND and chloroplasts; the emission to the right of the FND is chloroplasts that are out of focus. Since the measurement is intracellular, it is not possible to use total internal reflection fluorescence excitation.

Spectra in Fig. 6.10 show the CWODMR with only 520 nm after dark, after adjusting the sample; this is centred at 2.8007 GHz with a dip depth of 12.5%. The ODMR noise in this spectrum is higher, around 2.5%, than that previously presented. When 450 nm excitation is present, the dip depth decreases to 8% due to increased background fluorescence relative to the sample, but it remains centred at 2.8007 GHz with lower ODMR noise at 2%. When a scan is done without 520 nm excitation, the background noise is detected at 2% and no fit is possible since the NV- centre is not excited with the 450 nm excitation, showing the viability of the dual channel excitation without exciting the NV- centres at 450 nm as shown in Fig. 6.10. Understanding the FND's capability to measure CWODMR spectra in proximity to chloroplasts and the effects of dual excitation on CWODMR spectra prompted further measurements with another pond weed sample.

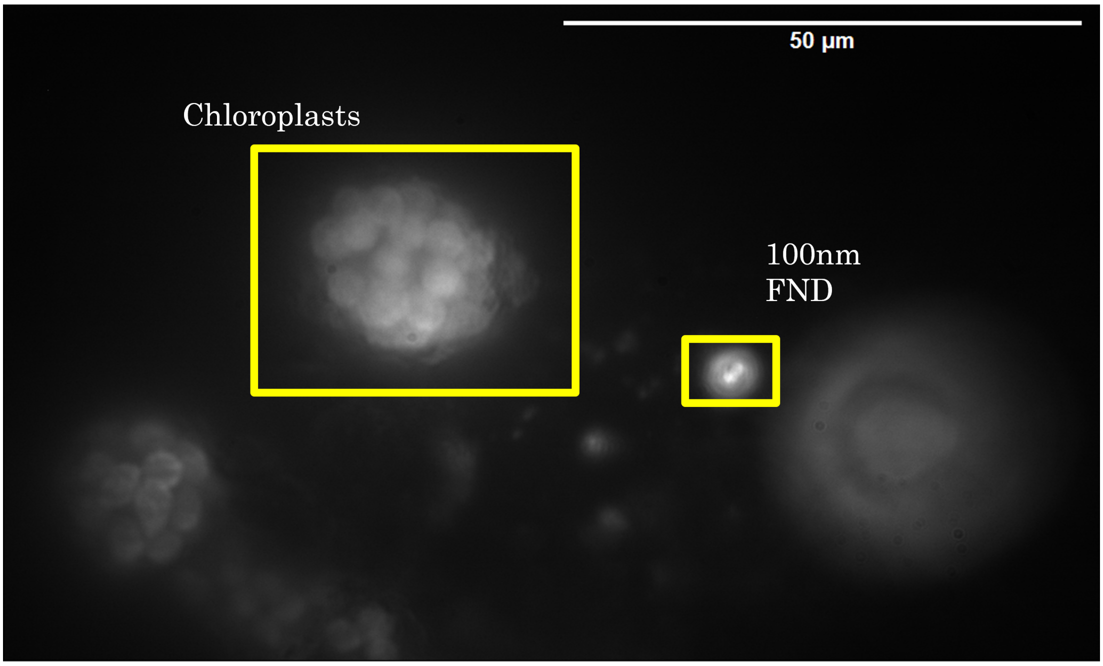

Figure 6.9: Widefield epifluorescence image showing chloroplasts and FND location in Pond Weed.

To ensure the FND is in proximity to the chloroplasts and not suspended in solution near them, a confocal scan is acquired, as shown in Fig. 6.11, which shows multiple FNDs adhered to the surface of the pond weed. CWODMR spectra are acquired again, and the decision to increase the microwave frequency step size to 5 MHz from 2 MHz is taken to reduce acquisition time, despite the loss of information, to capture any temperature shift more quickly, since four-point measurements used in subsequent sections do not require 2 MHz steps for characterisation. Initial characterisation with a full CWODMR scan is required for four-point measurement. All graphs show a shift from the initial 520 nm excitation scan to the 450 nm and 520 nm scans at their central points. With dual excitation the central point shifts from 2.80080 GHz to 2.875 GHz in both repeats. There is also broadening, with the two minima increasing in separation by around 5 MHz after the 450 nm excitation is incident. As these scans are performed in a different sample to those in Fig. 6.10, it is perhaps not surprising that the central dip is at 2.80080 GHz opposed to 2.80070 GHz. The data shown at the top of Fig. 6.12 shows a small differential with the 450 nm excitation indicating a temperature decrease in line

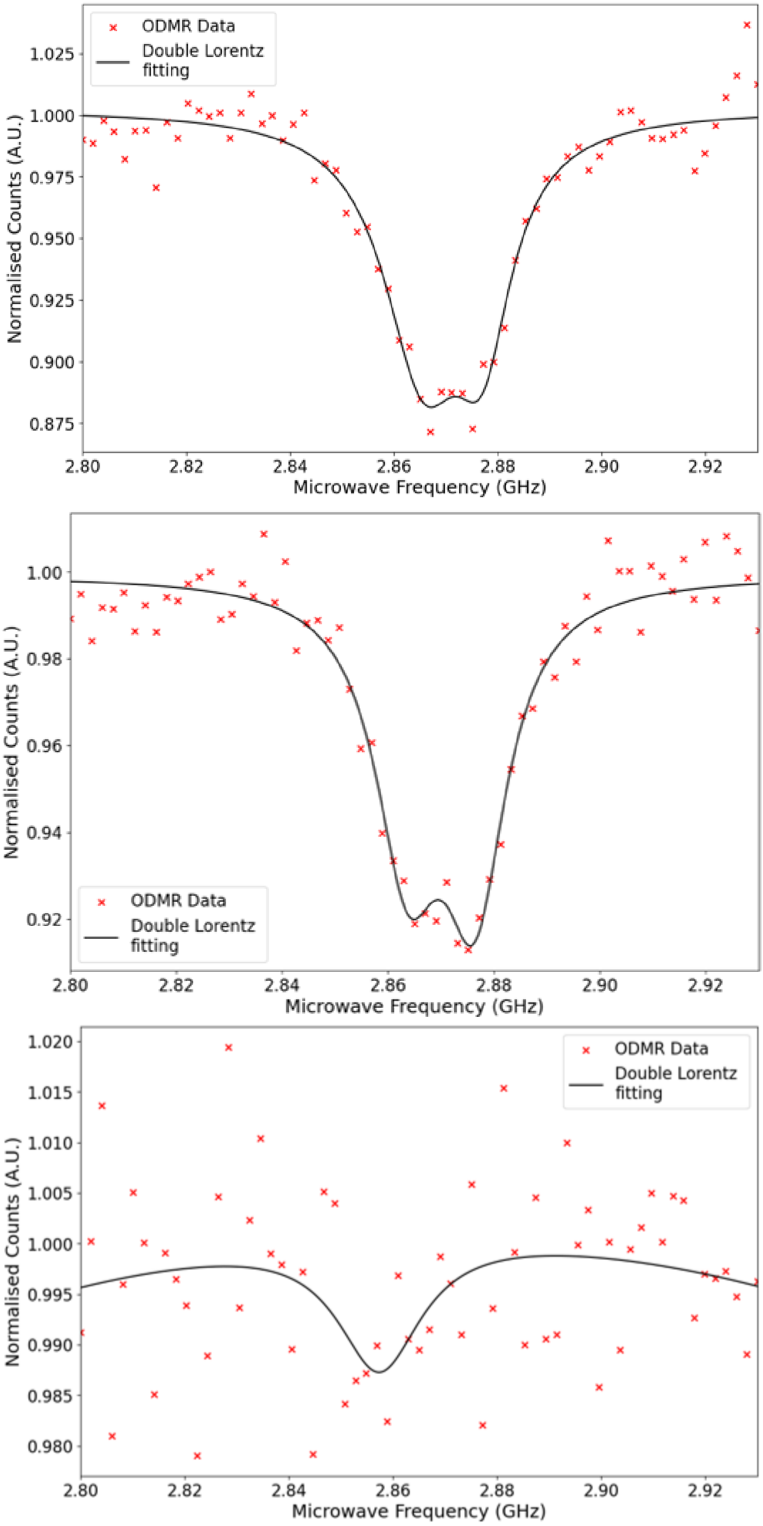

Figure 6.10: CWODMR spectra produced from Fig. 6.9 where the top is spectra produced with only 520 nm excitation, the middle is 520 nm and 450 nm excitation to excite Chlorophyll, and the bottom is 450 nm excitation only.

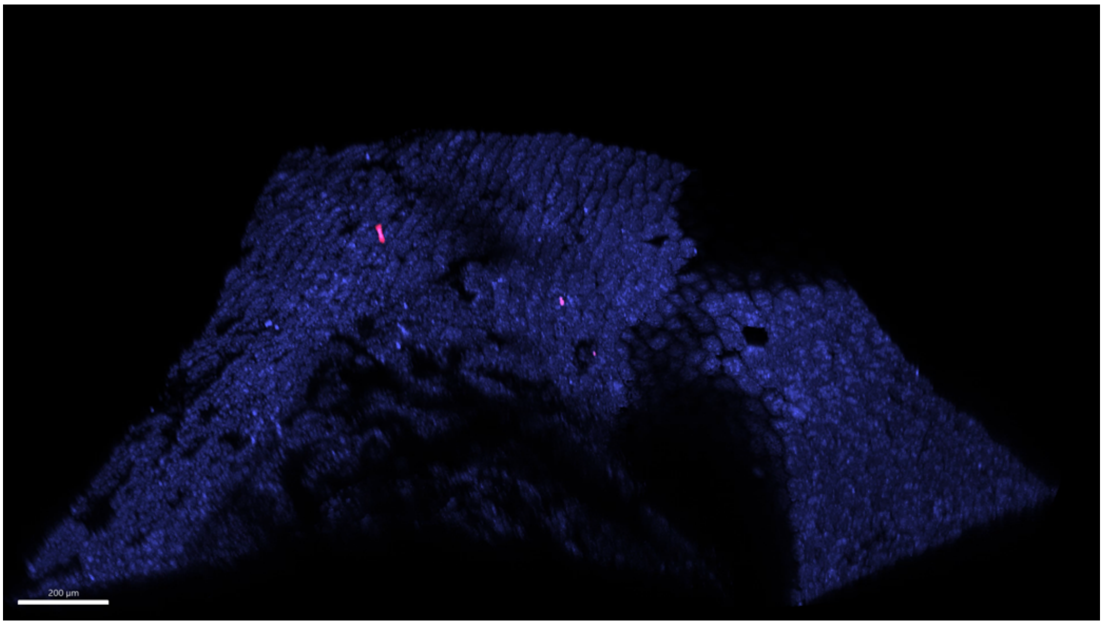

Figure 6.11: Confocal image with magenta showing NV- centres and purple indicating Chlorophyll II emission from Chloroplasts.

with the biological understanding of the chemical processes behind photosynthesis. The timescale for dark adjustment varies from sample to sample; further study could be done to determine the optimal time between measurements. However, the second sample shown at the bottom indicates heating, with a spectral centre shift to the left and poorer resolution. This cannot be confirmed due to temperature-sensing characterisation issues presented in Chapter 4.

This warranted further investigation using a scientifically significant, controlled sample from a known strain with expected structure and behaviour. *Spirogyra varians* is used as this sample could be purchased and is not limited by a thick surrounding of chromatin, allowing total internal reflection fluorescence excitation in conjunction with epifluorescence excitation.

6.5 *Spirogyra varians*

After experimentation with pond weed, *Spirogyra varians* is selected due to its repeating, predictable structure, thin cell membrane and its ease of culture.

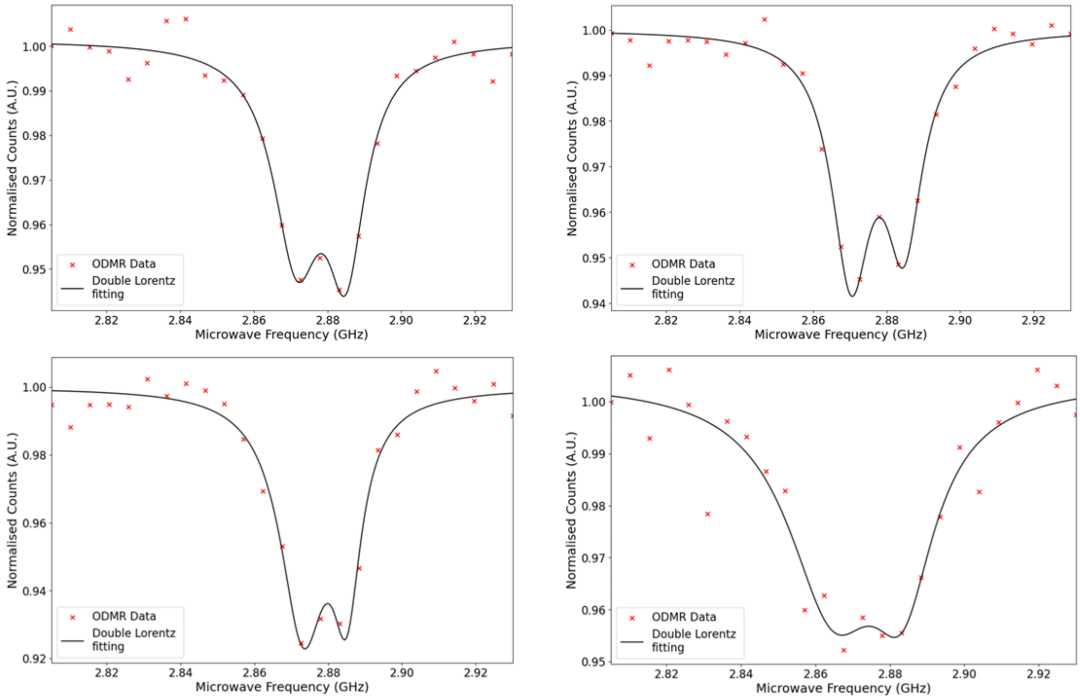

Figure 6.12: Repeated measurement of two samples (grouped top and bottom) with 520 nm excitation on the left and dual excitation 450 nm and 520 nm on the right.

6.5.1 Maintenance

Spirogyra varians are cultured in 3N-BBM+V medium, which is bought in stock. Once in solution in conical flasks, a bung is inserted, and the cultures are left at room temperature in direct sunlight to propagate. Once the mass has grown, culture can be aseptically subcultured for imaging.

6.5.2 Methodology

Spirogyra varians are sub-cultured for imaging purposes, shaken for 2 hours with 50 μL 70 nm FND solution in culture media. A monolayer of 70 nm FND is dry adhered to an 18 mm round coverslip, *S. varians* are deposited on top of the bed of diamond in proximity to the 50 μm copper wire. The sample is mounted in 3N-BBM+V media and sealed with a 16 mm coverslip and commercial nail polish. This sample is mounted on a total internal reflection prism. The sample is then starved from light for 48 hours before experimentation began. Since the sample is mounted in the media, it is assumed it is not lacking nutrients; however, the lack of available oxygen may be a source of additional starvation.

Initial imaging is performed using epifluorescence with 520 nm excitation for FND emission. A CWODMR is obtained between 2.800 and 2.930 GHz with a step size of 5 MHz. The frame integration time is set to 200 ms, the camera gain is 15 dB, the microwave power is set to -5 dBm, and there are 10 repeats per frequency.

Four-point measurements are then acquired with 520 nm excitation with 10 repeats per frequency and 40 line repeats. Another scan is acquired with 520 nm (115 mA) and 450 nm (35 mA) excitation to excite chlorophyll II and induce photosynthesis with 10 repeats per frequency and 150 line repeats. Finally, a relaxation scan (where photosynthesis should slow with no 450 nm excitation) is taken under the same parameters, using exclusively 520 nm excitation to track the temperature-sensing moving back into the dark state. Due to the issues presented in Chapter 4, this is the recommended protocol, and ODMR results will be discussed. However, no conclusive discussion can be had about the thermal results, as characterisation of the response to thermal shifts could not be completed on the FND used in this experiment to verify the -75 MHz/K value; however, trends seen in the data can be presented.

6.5.3 Results - Continuous Wave Optically Detected Magnetic Resonance in *Spirogyra varians*

After culture experimentation is done to ensure FND would adhere to the cell, the proximity of FND to chloroplasts is shown in Fig. 6.13 where magenta is a wide-field transmission image of the *Spirogyra varians* cell and cyan shows the location of 70 nm FND and chloroplasts, differentiated by Airy rings present on FND and region of interest where CWODMR is possible. Dark banding is present in the algal cell wall.

To demonstrate the capabilities of the multi-modal microscope for NV- sensing *in situ*, CWODMR spectra are acquired for epifluorescence and total internal reflection fluorescence excitation, and the results are shown in Fig. 6.14. These are acquired from different samples, but the same acquisition scheme is used (200 ms, 15 dB camera gain) with the same scan criteria (2.800-2.930 GHz, 5 MHz step size).

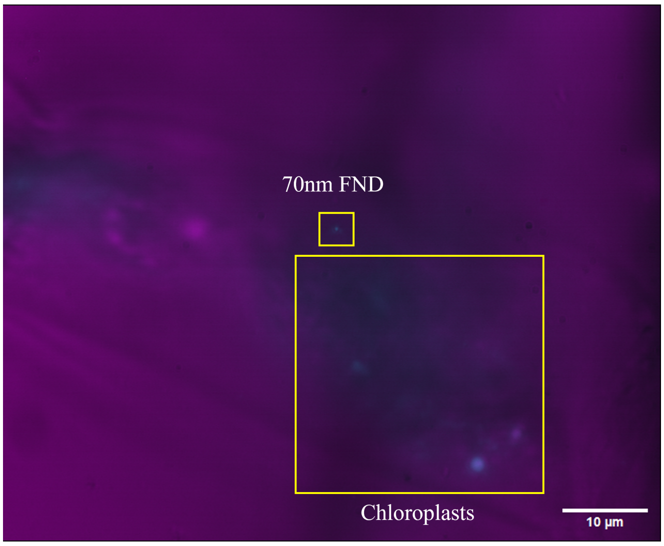

Figure 6.13: Widefield epifluorescence image showing chloroplasts and FND location in *Spirogyra varians*. Magenta is a brightfield image overlaid with cyan fluorescence channels.

Both spectra are similar despite being from separate samples; the only key difference is the dip depth on each spin state, which is greater at the lower-frequency minima on the top than at the higher-frequency minima on the bottom. This is likely due to a slight difference in the FND orientation. Otherwise, these spectra have a similar dip depth (8%) and ODMR noise (1%), which are similar to what has been presented in other organisms in this chapter and even in diamond-only samples in Chapter 3.

The spectral similarity indicates that both modalities are adequate for CWODMR measurements and that 4-point thermometry could be performed with either modality.

6.6 Conclusions

This work set out to determine the viability of the system as a means to undertake biological measurement within an organism using NV- centres. The increase in spatial information afforded by widefield CWODMR scans compared to single photon detectors allows the determination of key results, as the user can immediately recognise the local environment of the measurement. Widefield imaging also enabled continuous observation of the sample, which, if thermometry protocols had been characterised, would have provided real-time information on mechanical processes within the cell.

The use of a common biological model, *Caenorhabditis elegans*, facilitated a clear understanding and confirmation of CWODMR measurement capability, as this organism is well established for this measurement. Determining that the measurement could be taken from inside the organism is an important step in this research. This study confirmed that it is possible and that CWODMR outputs are comparable to those from FND measurement alone. It also allowed understanding the effects of background fluorescence from other emitters in the field of view on the resulting CWODMR spectra for calibration, since the sample continuously emitted mCherry. *Caenorhabditis elegans* is used as a model to determine methods of biological sample preparation, since it is known that the organism would uptake the FND. They are used to determine methods for sample preparation and mounting to inform a study into unknown biological samples.

Tetrahymena pyriformis had a similar mechanism of establishing ingress of FND to the organism (both would consume without interference) as with *Caenorhabditis elegans*, which is less complex than other biological models could have been. The biggest limiting factor for the *Tetrahymena pyriformis* measurement is the difficulty in immobilisation. After several iterations, a suitable method is found using low-melting-point agarose. The achievement of CWODMR *in situ* demonstrates the capabilities of this system for wide-field, spatially correlated measurements of cellular structures in live cells and for comparing CWODMR internally with structures external to an organism within the field of view. Using Allan deviation, a comparison can be made with the Allan deviation produced in Chapter 5 for similar imaging criteria. Outside the organism, the standard deviation is typically smaller for any given number of repeats, and there is less variability between them. Further investigations could have been conducted in biological studies; for example, there is interest in examining the oxygenated free radical production by photosensitizers and its effects on CWODMR spectra, but time limitations prevented this. [97]

Pond weed offered a segue into plant biology and looking at the role of thermal production in photosynthesis. Whilst not easily reproduced, observing a difference in the CWODMR between light-starved and 450 nm-excited chlorophyll is a vital piece of research that led to these measurements. Primarily, spectra showing a difference between 520 nm excitation and dual 520 nm and 450 nm excitation, where the central point red-shifted, demonstrated that the FND could ingress towards the chloroplasts to observe the effects of photosynthesis. As the effects of dual excitation had already been studied and showed no effect on FND CWODMR spectra in Chapter 2, it can be concluded that any effects demonstrated on the CWODMR between single excitation and dual excitation are due to the biochemical (photosynthesis) event causing a thermal shift. Since it is known Chlorophyll II can undergo CWODMR measurements, the 450 nm exclusive CWODMR spectra proved that the excitation microwave frequencies are in the wrong range to excite the spin state transitions in Chlorophyll II further confirming that there is a response in the CWODMR to the excitation of the chloroplasts. However, this isn't fully characterised due to the mechanical and thermal limitations on measurement within the system.

Moving into work with *S. varians*, similar outputs are observed with CWODMR as with the pond weed. These experiments allowed the repeat of those done with the pond weed using a known strain, removing the possibility of natural variability between the model biological organism and the found. The disparity between epifluorescence measurement and total internal reflection fluorescence measurement is difficult to explain apart from the total internal reflection fluorescence volume of excitation being too small for thermodynamic coupling of the FND to the system of interest. Ideally, full temperature sensing characterisation would have occurred, which would have made this result meaningful; however, as discussed, the variation in temperature on the temperature control stage is too great to obtain a measurement.

Overall, this demonstrates the widefield system's ability to perform meaningful CWODMR measurements in biological specimens, and the dual excitation indicates that important biological measurements are compatible with this system in the future.

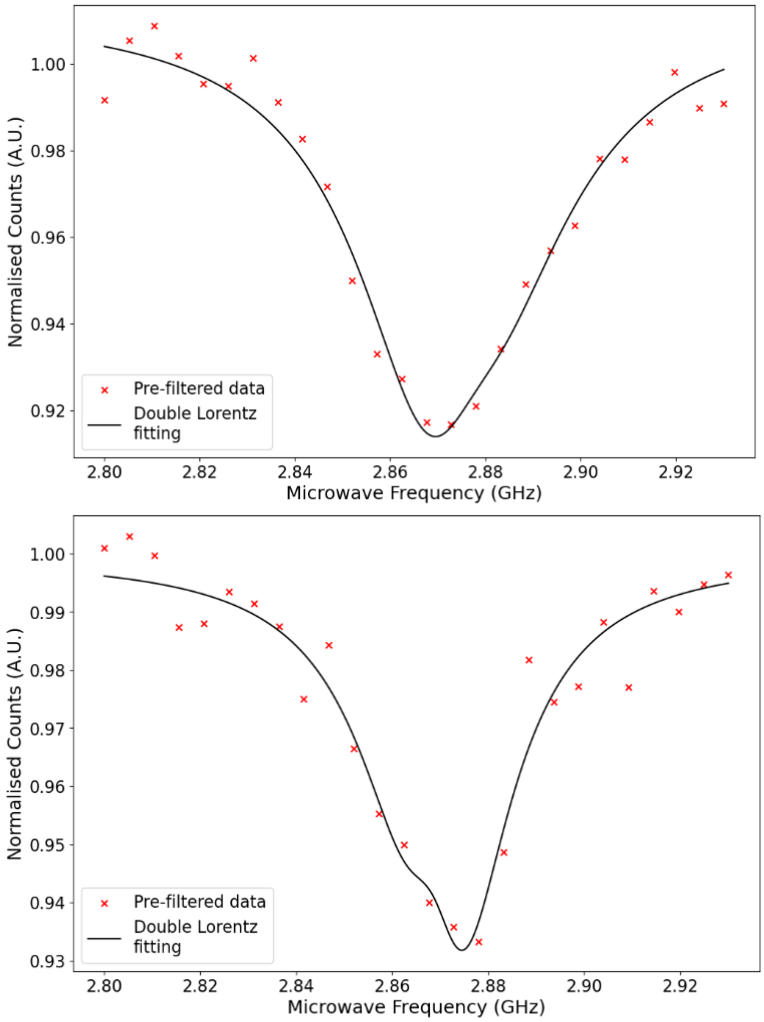

Figure 6.14: CWODMR spectra of 70 nm FND in *Spirogyra varians* with top using epifluorescence excitation and bottom using total internal reflection fluorescence excitation.

Chapter 7

Conclusion

In pursuit of an optical system capable of biological imaging and nitrogen vacancy sensing, with viability for implementation in multidisciplinary research, this project set clear criteria for success. The viability of future experimentation depended on whether a widefield system using CMOS detection would be capable of continuous wave optically detected magnetic resonance comparable to previously published research.

Key criteria for success included:

1. An epifluorescence system capable of producing continuous wave optically detected magnetic resonance spectra.
2. A total internal reflection fluorescence microscope capable of producing continuous wave optically detected magnetic resonance spectra.
3. Combining the above techniques for widefield excitation without disrupting the continuous wave optically detected magnetic resonance spectra.
4. Characterisation of each technique employed and how they compare to already published outcomes.
5. Comparative imaging in biological specimens already imaged in nitrogen vacancy sensing schemes.
6. Expanding the scope of biological imaging for nitrogen vacancy sensing with real-time widefield spatial information.

The work presented shows the development of this microscope from its initial principles, culminating in a multi-modal microscope that serves as a viable platform for biological imaging. Characterisation demonstrated the distribution of noise across different modes. It showed differences in excitation homogeneity across excitation lasers, which is a limiting factor for dual excitation, as inhomogeneous illumination is largely due to the multi-mode fibre in epifluorescence excitation. To determine the effectiveness of the total internal reflection fluorescence modality, selective excitation is demonstrated, enabling the exclusion of out-of-focus emission and the resolution of focal adhesions in HeLa cells, compared with full-volume excitation in epifluorescence.

Building on the microscopy system, the implementation of the measurement scheme for nitrogen vacancy sensing further highlighted the need for calibration. Sample preparation played a role in the delivery of microwaves, as it deviated from previous work using waveguides, which required insight into how efficiently microwaves would be delivered in this new format, in which the waveguide had been split into two. After confirming that the microwave excitation would pass into the sample, region of interest selection is investigated. After sample preparation, the quality of continuous wave optically detected magnetic resonance is limited by the ability to select an ROI as close to a single fluorescent nanodiamond as possible, since larger congregates distort the fluorescence spectra through inhomogeneous broadening as a culmination of spin effects. To determine the location of these single fluorescent nanodiamonds, CLAHE and SRRF are attempted. SRRF can provide information on the location of optically active fluorescent nanodiamond sites, but requires a lengthy imaging process that is unrealistic for photosensitive biological samples; by comparison, CLAHE is a faster process that produces qualitatively similar results and can be performed without acquiring large amounts of data.

The effects of different imaging modalities on the production of continuous wave optically detected magnetic resonance spectra and the interactions between fluorescent nanodiamond and other excitation wavelengths during dual excitation had to be examined, as these are novel techniques. This found an improvement in fluorescent nanodiamond detection using total internal reflection fluorescence excitation, due to reduced background noise and out-of-focus emission from other emitters. It is also noted that significant mode-hopping occurred in the epifluorescence configuration, leading to a poor fit to a double Lorentzian. Moreover, there is no notable effect from dual excitation at other wavelengths, and 450 nm did not excite the nitrogen vacancy centre into spectroscopy schemes. Ideally, an investigation could have been done to determine whether there is a marked improvement in epifluorescence stability by using the excitation source from the total internal reflection fluorescence excitation to solidly conclude that the inhomogeneities in measurement are due to the RGB laser mode-hopping rather than the epifluorescence modality itself, as hypothesised in this work. Finally, to ensure a quantum response from the fluorescent nanodiamond measurable in widefield CMOS detection, magnetometry is introduced. Using neodymium magnets, it is possible to split the spin states via Zeeman splitting and, importantly, to measure the splitting using continuous wave optically detected magnetic resonance, which is unaffected by the presence of magnetic nanoparticles used in biological investigations. Having determined the system is capable of quantum measurement, it is possible to conduct further experimentation.

To assess the performance of this system relative to others previously published in the field, thermometry is attempted. The first step in the thermometry measurement process is to calibrate the fluorescent nanodiamond's response to temperature changes, since each type responds differently, as measured by the strain it imposes on the crystal lattice. Unfortunately, it is impossible to calibrate. Using the PID, it is noted that microwaves interfered with the probe, causing erroneous measurements that, when integrated into the PID loop, led to large temperature fluctuations at the sample plane, resulting in defocusing and refocusing of the sample. The bath improved thermal stability over longer periods, until microwaves are introduced, at which point the same erroneous measurements occurred. In further work, it would be prudent to reattempt these measurements and consider ways to mitigate the heating effect, such as using an electronic cold junction to improve the PID loop's temperature reading accuracy.

Allan variance as a tool for evaluating fluorescence stability of emitters is a novel concept, and using the measurements in this body of work to comment on various imaging parameters allows a deeper understanding of how these imaging parameters can be sampled to reduce deviation. Determining that exposure time, camera gain, and laser power (which directly affects image contrast) affect the stability of the detected fluorescence signal over time is key to investigating the imaging parameters used in scans that require many image repeats. More data points could have been explored, as well as more exposure times, gains, and laser powers across various systems, to determine whether this remains true across different imaging modalities and systems. However, the scale of those measurements is outside the project's scope and would require significant time to acquire, so they are not explored further. Definitive proof that the use of a microwave generator improves the stability of long-term imaging by reducing the optical heating differential caused by turning microwaves on and off is produced using Allan deviation, and this is the first time this has been presented quantitatively. To determine whether Allan deviation is useful for estimating the sampling required for continuous wave optically detected magnetic resonance, the number of repeats is compared between the two modalities. The deviation from the continuous wave optically detected magnetic resonance fit improved in both imaging modalities, as predicted by the Allan deviation. Ideally, this should have been repeated with multiple samples to confirm; however, the time required to obtain these measurements is limited, so further investigation is advised.

Finally, the measurement scheme is applied to biological specimens. Each sample contributed to the system's credibility for widefield continuous wave optically detected magnetic resonance measurements. *C. elegans* have previously been imaged in widefield in a similar system using EMCCD detection, and successfully making this measurement to the same quality is a key point in the understanding of the viability of a system with CMOS detection. *T. pyriformis* proved the scope of measurement and detection in live organisms, providing real-time spatial information alongside continuous wave optically detected magnetic resonance detection outside of what has already studied. It is hoped that the investigation could examine the effects of oxygenated free radical production when the organism is under the influence of a photosensitizer; however, dibucaine HCl repeatedly killed the sample, and the use of cancer-involved photosensitizers is prohibited, so this line of inquiry had to be dropped. This would make an interesting follow-up in a suitable environment since it is known that the production of oxygenated free radicals affects the nitrogen vacancy centre, and the selective excitation provided by total internal reflection fluorescence would have allowed measurement with and without photoexcitation. Demonstrating the similarities in Allan deviation in fixed biological samples also shows the benefit of characterising the fluorescent nanodiamond emitter *in situ*, as the outcome is roughly the same as in a free sample. Finally, the inclusion of photosynthesis measurements in the form of pond weed and *S. varians* demonstrated that, despite the fluorescent nanodiamond not being fully characterised to provide a quantitative measurement, it is possible to induce and detect a thermometry event.

This work has demonstrated the construction and calibration of a multimodal CMOS widefield microscope for optically detected magnetic resonance measurements using the nitrogen-vacancy defect in nanodiamond. It has demonstrated widefield spectroscopy as an alternative to other systems in the literature, matching their resolution and contrast, two key parameters in the measurements. This system is a better choice for biological measurements because it adds spatial information, unlike photodetector-based systems and at a reduced cost compared to other systems.

Have no fear of perfection -
you’ll never reach it.

MARIE CURIE

Appendix A

Materials

In this paper a full list of equipment and suppliers is included, making it easier to find equipment to repeat parts of the experimentation.

Table A.1: Microwave Parts

Item	Part No.	Company	Location
Microwave Generator 1	TGR6000	Aim-TTi	Germany
Microwave Generator 2	USG-LF44	GW_INSTEK	United Kingdom
Microwave Switch	ZASWA-2-50DR+	mini-circuits	United States
Microwave Circulator	PE38CR1004	Pasternack	United States
Microwave Amplifier	AM64-2.7-3.1-40-40	microwave amps	United Kingdom

Table A.2: Biology Parts

Item	Part No.	Company	Location
C. elegans	VPR108	Caenorhabditis genetics centre	Minnesota, USA
T. pyriformis	CCAP 1630/21	SAMS	United Kingdom
S. varians	CCAP 678/3	SAMS	United Kingdom

Table A.3: Optics Parts

Item	Part No.	Company	Location
Laser 1	MSL-FN-532nm-300mW-19061472	Changchun New Industries Opto-electronics Tech. Co.	China
Condensor Lens	ACL25416U	ThorLabs	Germany
Dichroic Mirror	Di02-R532-25x36	Laser 2000	United Kingdom
Objective Lens	421090-9902-000	Zeiss	United Kingdom
Laser 2	Compact-RGB laser with FC Connector	Alrad Instruments	United Kingdom
Mirror	PF10-03-P01	ThorLabs	Germany
1/2 Waveplate	WPQ10E-532	ThorLabs	Germany
5x Beam Expander	GBE05-A	ThorLabs	Germany
Polarising Beam Splitter	CCM1-PBS25-532/M	ThorLabs	Germany
Focusing Lens (L3)	LJ1629RM-A	ThorLabs	Germany
Emission Filter (650LP)	FELH0650	ThorLabs	Germany
Emission Filter (600LP)	FELH0600	ThorLabs	Germany
Tube Lens	SM05	ThorLabs	Germany
Camera	CU235MP	ThorLabs	Germany
Prism	PS991	ThorLabs	Germany

Table A.4: Chemical Parts

Item	Part No.	Company	Location
Immersion Oil	Z-81226A	Olympus	United Kingdom
Fluorescent MicroSpheres	F8812	ThermoFisher	United Kingdom
Sodium Chloride	S7653-1KG	Sigma-Aldrich	United States
LB Broth with agar (Miller)	L3147-1KG	Sigma-Aldrich	United States
LB Broth (Miller)	L3522-1KG	Sigma-Aldrich	United States
Agar	05039-50G	Sigma-Aldrich	United States
Peptone	83059-500G-F	Sigma-Aldrich	United States
Cholesterol	C8503-25G	Sigma-Aldrich	United States
Calcium Chloride	C5670-100G	Sigma-Aldrich	United States
MgSO_4	M2643-500G	Sigma-Aldrich	United States
KH_2PO_4	P5379-1KG	Sigma-Aldrich	United States
Na_2HPO_4	P3786-1KG	Sigma-Aldrich	United States
Dibucaine Hydrochloride	D0638-5G	Sigma-Aldrich	United States
3N-BBM+V	FA3N-C	SAMS	United Kingdom

Table A.5: Miscellaneous Parts

Item	Part No.	Company	Location
DAQ	BNC-2110	National Instruments	United States
Thermister	TH10K	ThorLabs	Germany
Thermocouple	210-4372	RS Components	United Kingdom
Heating Element	TECF1S	ThorLabs	Germany
Motherboard	MTDEVAL1	ThorLabs	Germany
Daughterboard (thermistor)	MTD1020T	ThorLabs	Germany
Daughterboard (thermocouple)	MTD415TE	ThorLabs	Germany

Appendix B

Media and Preparation

This is a full account of the methods used to maintain cultures and make samples suitable for imaging.

Nanodiamond

Nanodiamond was prepared from stocks for 70 nm, 90 nm and 100 nm samples. These were diluted 1:100 with deionised water. Suspension was then agitated for 2 mins using sonocation to increase sample dispersion before being placed in the chamber of a nebuliser to create a mist of nanodiamond which coverslips were held in for 2 mins.

Growth Plates - *C. elegans*

Escherichia coli OP50 is the bacteria that sustain *C. elegans*, LB Agar plates were prepared for *E. coli* growth. Stocks of *E. coli* were collected from -80^{o}C freezer using sterile loop and streaked on LB Agar plates, growth occurs at 37^{o}C overnight in incubator. LB Broth was made in universals with 10 mL per universal, single colonies were selected after incubation from LB plates and transferred to LB universals, incubated overnight again at 37^{o}C until cloudy appearance.

Growth medium for *C. elegans* is Nemotode Growth Medium (NGM) and is made by suspending 1.25 g peptone, 1.5 g Sodium Chloride, 8.5 g agar and 462.5 mL deionised water then autoclaved. Flask is left to cool for 30 mins then buffers added. Buffers are

0.5 mL 5 mg/mL cholestrol in ethanol, 0.5 mL of 1 M Magnesium Sulphate, 0.5 mL 1 M Calcium Chloride and 12.5 mL 1 M Potassium Phosphate.

Medium plates were selected from growth and filled approximately 2/3 then left to harden overnight to determine if there was contamination. *E. coli* was cultured on these plates overnight by seeding 50 μL of *E. coli* suspension onto fresh NGM plates and growing overnight at 37^{o}C.

Plates with colonies of *C. elegans* were chunked (removing a chunk of NGM with worms present) and transfered face down to the fresh cultured plates. Plates could either be stored at room temperature to encourage growth of *C. elegans* colonies or placed in 14^{o}C fridge to slow growth and limit requirement for replating to every 3 months.

Growth Media - *T. pyriformis*

Modified Neff Media was used for *T. pyriformis* (CCAP 1630/1W, Culture Collection of algae & protozoa, Scotland) culturing. Modified Neff media consists of 0.25% proptease peptone, 0.25% yeast extract, 0.5% glucose and 33.3 μM Iron(III)Chloride. This media was separated into 5 100 mL cultures and autoclaved in bottle. To start a new culture 4 mL was removed asseptically from previous culture and placed in fresh culture media. This was then kept at room temperature exposed to normal lighting, subculture was undertaken every 2 months.

Growth Media - *S. varians*

For *S. varians* (CCAP 378/3, Culture Collection of algae & protozoa, Scotland) culture, Modified Bold Basal Medium with 3-fold Nitrogen and Vitamins was used as culture media. Concentrated stocks (CCAP FA3N-C, Culture Collection of algae & protozoa, Scotland) were bought from supplier so 5 mL of sodium nitrate, 0.5 mL of calcium chloride dihydrate, 0.5 mL magnesium sulfate heptahydrate, 0.5 mL Dipotassium hydrogen phosphate trihydrate, 0.5 mL Monopotassium phosphate, 0.5 mL sodium chloride, 3 mL trace elements, 0.5 mL Vitamin B_1 and 0.5 mL Vitamin B_{12} were suspended in

500 mL of deionised water. Media is autoclaved then small collection of *S. varians* is collected from previous culture and transfered to new culture. Culture is kept in direct sunlight to allow circadian pathway and at room temperature in Erlynmeyer flask.

Mounting Media - *C. elegans*

C. elegans needed to be immobilised for imaging using Agarose, a solution of 0.1% was made using TopVision Low Melting Point Agarose (R0801, ThermoFisher Scientific, United Kingdom). Agarose was then infused after cooling but before gel state with collected *C. elegans* and mounted for TIRFM imaging.

Bibliography

[1] Ryan Corbyn. “Optimising Temperature and Electromagnetic sensing using Nanodiamonds and Fluorescence Microscopy”. PhD thesis. University of Strathclyde, 2023.

[2] Richard H. Steckel. “Biological Measures of the Standard of Living.” In: *Journal of Economic Perspectives* 22.1 (2008), pp. 129–152. DOI: `10.1257/jep.22.1.129`.

[3] Kenneth A. Dawson and Yan Yan. “Current understanding of biological identity at the nanoscale and future prospects”. In: *Nature Nanotechnology* 16 (2021), pp. 229–242. DOI: `10.1038/s41565-021-00860-0`.

[4] Jung Woo Han et al. “Plasma Membrane Localized GCaMP-MS4A12 by Orai1 Co-Expression Shows Thapsigargin- and Ca2+-Dependent Fluorescence Increases”. In: *Molecules and Cells* 44.4 (2021), pp. 223–232. ISSN: 1016-8478. DOI: `10.14348/molcells.2021.2031`.

[5] Dal Hyung Kim et al. “Three-dimensional control of Tetrahymena pyriformis using artificial magnetotaxis”. In: *Applied Physics Letters* 100.5 (Feb. 2012), p. 053702. ISSN: 0003-6951. DOI: `10.1063/1.3678340`. eprint: `https://pubs.aip.org/aip/apl/article-pdf/doi/10.1063/1.3678340/14255181/053702_1_online.pdf`. URL: `https://doi.org/10.1063/1.3678340`.

[6] Masazumi Fujiwara et al. “Real-time nanodiamond thermometry probing in vivo thermogenic responses”. In: *Science Advances* 6.37 (2020), eaba9636.

[7] S. R. Hemelaar et al. “Nanodiamonds as multi-purpose labels for microscopy”. In: *Scientific Reports* 7 (2017). ISSN: 2045-2322. DOI: `10.1038/s41598-017-00797-2`.

[8] Santiago Hernández-Gómez and Nicole Fabbri. “Quantum Control for Nanoscale Spectroscopy With Diamond Nitrogen-Vacancy Centers: A Short Review”. In: *Frontiers in Physics* 8 (2021). ISSN: 2296-424X. DOI: `10.3389/fphy.2020.610868`. URL: `https://www.frontiersin.org/journals/physics/articles/10.3389/fphy.2020.610868`.

[9] Nabeel Aslam et al. “Quantum sensors for biomedical applications”. In: *Nature Reviews Physics* 5 (2023), pp. 157–169. DOI: `10.1038/s42254-023-00558-3`.

[10] Mark Hosey. *Allan Deviation Made Simple*. May 2023.

[11] S. Culley et al. “SRRF: Universal live-cell super-resolution microscopy.” In: *The international journal of biochemistry & cell biology* (2018). DOI: `10.1016/j.biocel.2018.05.014`.

[12] R A Serway J W Jewett. *Physics for Scientist and Engineers*. 9th ed. Cambridge MA: Cengage Learning, 2013.

[13] David M. Jameson. *Introduction to Fluorescence*. Boca Raton, FL: Taylor & Francis Group, 2014.

[14] Malte Renz. “Fluorescence microscopy - A historical and technical perspective”. In: *Cytometry Part A* 83 (9 2013). DOI: `10.1002/cyto.a.22295`.

[15] Edinburgh Instruments. *What is a Jablonski Diagram (Perrin-Jablonski Diagram)?* 2024. URL: `https://www.edinst.com/blog/jablonski-diagram-2/`.

[16] David Briers et al. “Laser speckle contrast imaging: theoretical and practical limitations”. In: *Journal of Biomedical Optics* 18.066018 (6 2013).

[17] Taylor L. Bobrow et al. “DeepLSR: a deep learning approach for laser speckle reduction”. In: *Biomedical Optics Express* 10.6 (2019), pp. 2869–2882. DOI: `10.1364/BOE.10.002869`.

[18] W. Ha et al. “Speckle reduction in multimode fiber with a piezoelectric transducer in radial vibration for fiber laser marking and display applications”. In: *Fiber Lasers V: Technology, Systems, and Applications*. Ed. by Jes Broeng and Clifford Headley. Vol. 6873. International Society for Optics and Photonics. SPIE, 2008, p. 68731V. DOI: `10.1117/12.774889`.

[19] M. Nadeem Akram et al. “Laser speckle reduction due to spatial and angular diversity introduced by fast scanning micromirror”. In: *Applied Optics* 49.17 (June 2010), pp. 3297–3304. DOI: `10.1364/AO.49.003297`.

[20] Zhaoning Zhang et al. “Characterizing and correcting camera noise in back-illuminated sCMOS cameras”. In: *Optical Express* 29.5 (Mar. 2021), pp. 6668–6690. DOI: `10.1364/OE.418684`.

[21] Biagio Mandracchia et al. “Fast and accurate sCMOS noise correction for fluorescence microscopy”. In: *Nature Communications* 11.94 (2020). DOI: `10.1038/s41467-019-13841-8`.

[22] Jyrki Selinummi et al. “Bright Field Microscopy as an Alternative to Whole Cell Fluorescence in Automated Analysis of Macrophage Images”. In: *PLoS One* 4.10 (2022). DOI: `10.1371/journal.pone.0007497`.

[23] Jack II Clifton and Jerrold B. Leikin. “Methylene Blue”. In: *American Journal of Therapuetics* (2003). URL: `https://journals.lww.com/americantherapeutics/fulltext/2003/07000/methylene_blue.9.aspx`.

[24] Elliot AD. “Confocal Microscopy: Principles and Modern Practices”. In: *Curr Protoc Cytom* 92.1 (2020). DOI: `10.1002/cpcy.68`.

[25] Max S. Fairlamb et al. “Construction of a Three-Color Prism-Based TIRF Microscope to Study the Interactions and Dynamics of Macromolecules”. In: *Biology* 10.7 (2021). ISSN: 2079-7737. DOI: `10.3390/biology10070571`. URL: `https://www.mdpi.com/2079-7737/10/7/571`.

[26] S. van de Linde et al. “Photoswitching microscopy with standard fluorophores.” In: *Applied Physics B Lasers and Optics* 93 (2008). DOI: `10.1007/s00340-008-3250-9`.

[27] Stephen M. Pizer et al. “Adaptive histogram equalization and its variations”. In: *Computer Vision, Graphics, and Image Processing* 39.3 (1987), pp. 355–368. DOI: `10.1016/S0734-189X(87)80186-X`.

[28] Johannes Schindelin et al. “Fiji: an open-source platform for biological-image analysis”. In: *Nature Methods* 9 (2012). ISSN: 1548-7105. DOI: `10.1038/nmeth.2019`.

[29] R. Giri et al. “Selective measurement of charge dynamics in an ensemble of nitrogen-vacancy centers in nanodiamond and bulk diamond”. In: *Physical Review B* 99 (15 2019), p. 155426. DOI: `10.1103/PhysRevB.99.155426`.

[30] Masazumi Fujiwara et al. “Real-time estimation of the optically detected magnetic resonance shift in diamond quantum thermometry toward biological applications”. In: *Phys. Rev. Res.* 2 (4 Dec. 2020), p. 043415. DOI: `10.1103/PhysRevResearch.2.043415`. URL: `https://link.aps.org/doi/10.1103/PhysRevResearch.2.043415`.

[31] A. Mzyk, A. Sigaeva, and R. Schirhagl. “Relaxometry with Nitrogen Vacancy (NV) Centers in Diamond.” In: *Accounts of chemical research* 55.24 (2022). DOI: `10.1021/acs.accounts.2c00520`.

[32] N. Aslam et al. “Photo-induced ionization dynamics of the nitrogen vacancy defect in diamond investigated by single-shot charge state detection”. In: *New Journal of Physics* 15 (2013). DOI: `10.1088/1367-2630/15/1/013064`.

[33] Akihiro Kuwahata et al. “Magnetometer with nitrogen-vacancy center in a bulk diamond for detecting magnetic nanoparticles in biomedical applications”. In: *Scientific Reports* 10 (2483 2020). DOI: `/10.1038/s41598-020-59064-6`.

[34] Gang-Qin Liu et al. “Coherent quantum control of nitrogen-vacancy center spins near 1000 kelvin”. In: *Nature communications* 10.1 (2019), p. 1344. ISSN: 2041-1723. DOI: `10.1038/s41467-019-09327-2`.

[35] Saravanan Sengottuvel et al. “Wide-field magnetometry using nitrogen-vacancy color centers with randomly oriented micro-diamonds”. In: *Scientific Reports* 12.17997 (2022).

[36] Agnieszka Szczsna et al. “Inertial Motion Capture Costume Design Study”. In: *Sensors* 17.3 (2017). ISSN: 1424-8220. DOI: `10.3390/s17030612`.

[37] E. Rubiola and Francois Vernotte. *The Companion of the Enrico’s Chart for Phase Noise and Two-Sample Variances.* Jan. 2022.

[38] Andrii V. Rudyk et al. “Strapdown Inertial Navigation Systems for Positioning Mobile RobotsMEMS Gyroscopes Random Errors Analysis Using Allan Variance Method”. In: *Sensors* 20.17 (2020). ISSN: 1424-8220. DOI: `10.3390/s20174841`.

[39] Martina C. Wiedner. *Noise Charaterisation and Allan Variances of Water Vapour Monitors.* Tech. rep. memo 148. SMA, 2002.

[40] Keisuke Oshimi et al. “Bright Quantum-Grade Fluorescent Nanodiamonds”. In: *ACS Nano* 18 (52 2024). DOI: `10.1021/acsnano.4c03424`.

[41] Ruheng Shi et al. “Multi-plane, wide-field fluorescent microscopy for biodynamic imaging in vivo”. In: *Biomedical Optics Express* 10.12 (2019), pp. 6625–6635. DOI: `10.1364/BOE.10.006625`.

[42] Martin Oheim et al. “Calibrating Evanescent-Wave Penetration Depths for Biological TIRF Microscopy”. In: *Biophysical Journal* 117 (2019), pp. 795–809.

[43] Amicia D Elliott. “Confocal microscopy: principles and modern practices”. In: *Current protocols in cytometry* 92.1 (2020).

[44] Tobias Müller, Christian Schumann, and Annette Kraegeloh. “STED Microscopy and its Applications: New Insights into Cellular Processes on the Nanoscale”. In: *ChemPhysChem* 13 (8 2012). DOI: `10.1002/cphc.201100986`.

[45] Michael J Rust, Mark Bates, and Xiaowei Zhuang. “Sub-diffraction-limit imaging by stochastic optical reconstruction microscopy (STORM)”. In: *Nature Methods* 3 (793–796 2006). DOI: `10.1038/nmeth929`.

[46] Bhanu Neupane, Frances S. Ligler, and Gufeng Wang. “Review of recent developments in stimulated emission depletion microscopy: applications on cell imaging.” In: *Journal of Biomedical Optics* 19.8 (2014), p. 080901. DOI: `10.1117/1.JBO.19.8.080901`.

[47] Gail McConnell et al. “A novel optical microscope for imaging large embryos and tissue volumes with sub-cellular resolution throughout”. In: *eLife* 5 (2016), e18659. DOI: `10.7554/eLife.18659`.

[48] F.B. LEGESSE et al. “Seamless stitching of tile scan microscope images”. In: *Journal of Microscopy* 258 (3 2015), pp. 223–232. DOI: `10.1111/jmi.12236`.

[49] Michael J. Sanderson et al. “Fluorescence Microscopy”. In: *Cold Spring Harb Protocols* 10 (2014). DOI: `10.1101/pdb.top071795`.

[50] Yinan Wan, Katie McDole, and Philipp J. Keller. “Light-Sheet Microscopy and Its Potential for Understanding Developmental Processes”. In: *Annual Review of Cell and Developmental Biology* 35 (2019). DOI: `10.1146/annurev-cellbio-100818-125311`.

[51] Chen-Hao P. Lin et al. “Multi-mode fiber-based speckle contrast optical spectroscopy: analysis of speckle statistics”. In: *Optical Letters* 48.6 (2023), pp. 1427–1430. DOI: `10.1364/OL.478956`.

[52] Paula J Cranfill et al. “Quantitative assessment of fluorescent proteins”. In: *Nature Methods* 13 (7 2016). DOI: `10.1038/nmeth.3891`.

[53] M. Omini and A. Sparavigna. “Heat transport in dielectric solids with diamond structure”. In: *Il Nuovo Cimeto* 19.10 (1997), pp. 1537–1563.

[54] Lilian Childress and Ronald Hanson. “Diamond NV centers for quantum computing and quantum networks”. In: *MRS Bulletin* 38.2 (2013), pp. 134–138. DOI: `10.1557/mrs.2013.20`.

[55] M. Panizza and G. Cerisola. “Application of diamond electrodes to electrochemical processes”. In: *Electrochimica Acta* 51.2 (2005), pp. 191–199. DOI: `10.1016/j.electacta.2005.04.023`.

[56] Orlando Auciello et al. “Materials science and fabrication processes for a new MEMS technology based on ultrananocrystalline diamond thin films”. In: *Journal of Physics: Condensed Matter* 16.16 (Apr. 2004), R539. DOI: `10.1088/0953-8984/16/16/R02`.

[57] Joanne Duberley et al. “Diamonds are a girls best friend? Examining gender and careers in the jewellery industry”. In: *Organization* 24.3 (2017), pp. 355–376. DOI: `10.1177/1350508416687767`.

[58] Rian Mulcahy. “Facets of value: an investigation into the formation of worth in the diamond market”. PhD thesis. London School of Economics and Political Science, 2017.

[59] Hadjer Boukhatem et al. “Evaluation of Slowfade Diamond as a buffer for STORM microscopy”. In: *Biomedical optics express* 14.2 (2023), pp. 550–558.

[60] Silvia Arroyo-Camejo et al. “Stimulated emission depletion microscopy resolves individual nitrogen vacancy centers in diamond nanocrystals”. In: *ACS nano* 7.12 (2013), pp. 10912–10919.

[61] Hannes Bernien et al. “Two-photon quantum interference from separate nitrogen vacancy centers in diamond”. In: *Physical Review Letters* 108.4 (2012), p. 043604.

[62] Fedor Jelezko et al. “Observation of coherent oscillations in a single electron spin”. In: *Physical review letters* 92.7 (2004), p. 076401.

[63] Aldona Mzyk, Alina Sigaeva, and Romana Schirhagl. “Relaxometry with nitrogen vacancy (NV) centers in diamond”. In: *Accounts of Chemical Research* 55.24 (2022), pp. 3572–3580.

[64] Yiwen Chu and Mikhail D Lukin. “Quantum optics with nitrogen-vacancy centers in diamond”. In: *Quantum Optics and Nanophotonics* (2015), pp. 229–270.

[65] Patrick Maletinsky et al. “A robust scanning diamond sensor for nanoscale imaging with single nitrogen-vacancy centres”. In: *Nature nanotechnology* 7.5 (2012), pp. 320–324.

[66] Dhruvil Hiteshkumar Jariwala, Dhrumi Patel, and Sarika Wairkar. “Surface functionalization of nanodiamonds for biomedical applications”. In: *Materials Science and Engineering: C* 113 (2020), p. 110996.

[67] Christian Laube et al. “Controlling the fluorescence properties of nitrogen vacancy centers in nanodiamonds”. In: *Nanoscale* 11.4 (2019), pp. 1770–1783.

[68] Suvechhya Lamichhane et al. “Magnetic Relaxometry of Hemoglobin by Widefield Nitrogen-Vacancy Microscopy”. In: *arXiv preprint arXiv:2405.08227* (2024).

[69] Suvechhya Lamichhane et al. “Nitrogen-Vacancy Magnetic Relaxometry of Nanoclustered Cytochrome C Proteins”. In: *Nano Letters* 24.3 (2024), pp. 873–880.

[70] Hui Ting Li et al. “Measuring free radicals with relaxometry: Pioneering steps for measurements in human semen”. In: *Diamond and Related Materials* 140 (2023), p. 110388.

[71] A. Dréau et al. “Avoiding power broadening in optically detected magnetic resonance of single NV defects for enhanced dc magnetic field sensitivity”. In: *Physical Review B* 84 (19 2011), p. 195204. DOI: `10.1103/PhysRevB.84.195204`.

[72] Takuya F. Segawa and Ryuji Igarashi. “Nanoscale quantum sensing with Nitrogen-Vacancy centers in nanodiamonds A magnetic resonance perspective”. In: *Progress in Nuclear Magnetic Resonance Spectroscopy* 134–135 (2023), pp. 20–38.

[73] Stefan Fischer. *Apply CLAHE filter on a stack in Fiji*. URL: `http://stefischer.de/2019/06/12/apply-clahe-filter-on-a-stack-in-fiji/`.

[74] Peng Ji et al. “Multiple-photon excitation of nitrogen vacancy centers in diamond”. In: *Phys. Rev. B* 97 (13 Apr. 2018), p. 134112. DOI: `10.1103/PhysRevB.97.134112`.

[75] Yushi Nishimura et al. “Wide-field fluorescent nanodiamond spin measurements toward real-time large-area intracellular thermometry”. In: *Scientific Reports* 11 (2021).

[76] Claudia Stella et al. “Characterization of nanodiamond samples for intracellular temperature sensing”. In: *Measurement: Sensors* (2025), p. 101650. ISSN: 2665-9174. DOI: `10.1016/j.measen.2024.101650`.

[77] Kanda Wongwailikhit and Saranporn Horwongsakul. “The preparation of iron (III) oxide nanoparticles using W/O microemulsion”. In: *Materials Letters* 65.17 (2011), pp. 2820–2822. DOI: `10.1016/j.matlet.2011.05.063`.

[78] A. M. Wojciechowski et al. “Optical Magnetometry Based on Nanodiamonds with Nitrogen-Vacancy Color Centers.” In: *Materials (Basel)* 12 (18 2019). DOI: `10.3390/ma12182951`.

[79] Akihiro Kuwahata et al. “Magnetometer with nitrogen-vacancy center in a bulk diamond for detecting magnetic nanoparticles in biomedical applications”. In: *Scientific Reports* 10 (2020). DOI: `10.1038/s41598-020-59064-6`.

[80] Masazumi Fujiwara et al. “Observation of the linewidth broadening of single spins in diamond nanoparticles in aqueous fluid and its relation to the rotational Brownian motion”. In: *Scientific Reports* 8.1 (2018). DOI: `10.1038/s41598-018-33041-6`.

[81] K. Lu et al. “Intracellular Heat Transfer and Thermal Property Revealed by Kilohertz Temperature Imaging with a Genetically Encoded Nanothermometer.” In: *Nano letters* 22.14 (2022). DOI: `10.1021/acs.nanolett.2c00608`.

[82] Kohki Okabe and Seiichi Uchiyama. “Intracellular thermometry uncovers spontaneous thermogenesis and associated thermal signaling”. In: *Communications Biology* 4.1 (2021). DOI: `110.1038/s42003-021-02908-2`.

[83] Changling Wang et al. “Determining intracellular temperature at single-cell level by a novel thermocouple method”. In: *Cell Research* 21 (2011), pp. 1517–1519.

[84] Fangxu Wang et al. “Multichannel cell thermometry system based on transparent platinum resistance for real-time visual monitoring energy metabolism in vascular endothelial cells”. In: *Nano Today* 54 (2024), p. 102125. ISSN: 1748-0132.

[85] Masaaki K. Sato et al. “Temperature Changes in Brown Adipocytes Detected with a Bimaterial Microcantilever”. In: *Biophysical Journal* 106.11 (2014), pp. 2458–2464. ISSN: 0006-3495.

[86] Masahiro Nakano and Takeharu Nagai. “Thermometers for monitoring cellular temperature”. In: *Journal of Photochemistry and Photobiology C: Photochemistry Reviews* 30 (2017). Special issue on Bioimaging, pp. 2–9. ISSN: 1389-5567.

[87] Rupsa Datta et al. “Fluorescence lifetime imaging microscopy: fundamentals and advances in instrumentation, analysis, and applications”. In: *Journal of Biomedical Optics* 25 (2020), pp. 1–43.

[88] G. Kucsko et al. “Nanometre-scale thermometry in a living cell”. In: *Nature* 50 (2013), pp. 54–58.

[89] Hiroshi Yukawa et al. “A quantum thermometric sensing and analysis system using fluorescent nanodiamonds for the evaluation of living stem cell functions according to intracellular temperature”. In: *Nanoscale Advances* 2 (5 2020), pp. 1859–1868.

[90] Zhonghao Li et al. “Microwave power self-coherent reference measurement based on ensembles of nitrogen-vacancy centers in diamond.” In: *Opt. Express* 32.13 (2024), pp. 23193–23203. DOI: `10.1364/OE.526072`.

[91] Istiaq Jamil Siddique and Arshad Adam Salema. “Unraveling the metallic thermocouple effects during microwave heating of biomass”. In: *Energy* 267 (2023), p. 126529. ISSN: 0360-5442. DOI: `https://doi.org/10.1016/j.energy.2022.126529`.

[92] Morteza Erfani et al. “Multiple microwave resonance interaction in silicon single-electron transistors”. In: *Journal of Physics: Conference Series* 193.1 (2009), p. 012048. DOI: `10.1088/1742-6596/193/1/012048`.

[93] Nicolas de Mateo Smith. “A technique for continuous measurement of the quality factor of mechanical oscillators.” In: *The Review of scientific instruments* 86 (2015), p. 053907.

[94] Sergey Dushenko, Kapildeb Ambal, and Robert D. McMichael. “Sequential Bayesian Experiment Design for Optically Detected Magnetic Resonance of Nitrogen-Vacancy Centers”. In: *Physical Review Applied* 14 (5 2020), p. 054036. DOI: `10.1103/PhysRevApplied.14.054036`.

[95] Michael Caouette-Mansour et al. “Robust Spin Relaxometry with Fast Adaptive Bayesian Estimation”. In: *Physical Review Applied* 17 (June 2022). DOI: `10.1103/PhysRevApplied.17.064031`.

[96] Michael J. M. Harrap et al. “Reporting of thermography parameters in biology: a systematic review of thermal imaging literature”. In: *Royal Society Open Science* 5.12 (2018), p. 181281. DOI: `10.1098/rsos.181281`.

[97] S Fan et al. “Quantum Sensing of Free Radical Generation in Mitochondria of Single Heart Muscle Cells during Hypoxia and Reoxygenation”. In: *ACS Nano* 18 (4 2024), pp. 2982–2991. DOI: `10.1021/acsnano.3c07959`.

[98] Guillermo Senisterra, Irene Chau, and Masoud Vedadi. “Thermal Denaturation Assays in Chemical Biology”. In: *ASSAY and Drug Development Technologies* 10.2 (2012), pp. 128–136. DOI: `10.1089/adt.2011.0390`.

[99] Wnt signaling Eisenmann D. M. *The C. elegans Research Community, WormBoo.* 2005. DOI: `10.1895/wormbook.1.7.1`. URL: `http://www.wormbook.org` (visited on 09/24/2021).

[100] Marisa D Ruehle, Eduardo Orias, and Chad G Pearson. “Tetrahymena as a Unicellular Model Eukaryote: Genetic and Genomic Tools”. In: *Genetics* 203.2 (2016), pp. 649–665. ISSN: 1943-2631. DOI: `10.1534/genetics.114.169748`.

[101] Xie Chang-Li et al. “Microcalorimetric studies on Tetrahymena pyriformis: Part 1. Growth metabolic power and thermal equations”. In: *Thermochimica Acta* 183 (1991), pp. 117–123. ISSN: 0040-6031. DOI: `https://doi.org/10.1016/0040-6031(91)80451-N`. URL: `https://www.sciencedirect.com/science/article/pii/004060319180451N`.

[102] P Darcy et al. “The effect of lofepramine and other related agents on the motility of Tetrahymena pyriformis”. In: *Toxicology Letters* 128.1 (2002), pp. 207–214. ISSN: 0378-4274. DOI: `https://doi.org/10.1016/S0378-4274(01)00542-2`. URL: `https://www.sciencedirect.com/science/article/pii/S0378427401005422`.

[103] Johnson MP. “Photosynthesis”. In: *Essays Biochemistry* 61.4 (2017). DOI: `10.1042/EBC20160016_COR`.

[104] C.J.R. Sheppard. “MICROSCOPY | Overview”. In: *Encyclopedia of Modern Optics*. Ed. by Robert D. Guenther. Oxford: Elsevier, 2005, pp. 61–69. ISBN: 978-0-12-369395-2. DOI: `10.1016/B0-12-369395-0/00823-X`.

[105] Guy A. Thompson, Lonnie C. Baugh, and Laurie F. Walker. “Nonlethal deciliation of tetrahymena by a local anesthetic and its utility as a tool for studying cilia regeneration”. In: *The Journal of Cell Biology* 61 (1974), pp. 253–257.

[106] Jordan L. Cocchiaro and John F. Rawls. “Microgavage of Zebrafish Larvae”. In: *J Vis Exp* 72 (2013). DOI: `10.3791/4434`.